

Collective Short Wavelength Dynamics in Composite Phospholipid Model Membranes

with
Inelastic Neutron Scattering

Dissertation
zur Erlangung des Doktorgrades
der Mathematisch-Naturwissenschaftlichen Fakultäten
der Georg-August-Universität zu Göttingen

vorgelegt von
Beate-Annette Brüning
aus Bielefeld

Göttingen 2009

D7

Referent: Prof. Dr. Tim Salditt

Korreferent(in): Prof. Dr. Helmut Schober

Tag der mündlichen Prüfung: 02.12.2008

Contents

1	Introduction	5
2	Membranes and Membrane Dynamics	8
2.1	Biological Membranes	8
2.2	Model Membranes	9
2.2.1	Membrane Structure and Lamellar Phases	10
2.2.2	Phase Transitions	11
2.2.3	Lipid Melting: Cooperativity and In-plane Correlation	13
2.2.4	Membrane Interaction Potentials	16
2.3	Single Lipid and Composite Model Membranes Studied	18
2.3.1	DSPC: Chain-length and Main Phase Transition	18
2.3.2	Phospholipid/Cholesterol:	20
2.3.3	Phospholipid/Ethanol:	23
2.4	Collective In-plane Dynamics: Biological Membranes	27
2.4.1	Transmembrane Transport of Molecules	27
2.4.2	Nerve Pulse Propagation	27
3	Collective Dynamics in Model Membranes	28
3.1	Inelastic Neutron Scattering	28
3.1.1	The Scattering Cross Section	28
3.1.2	Coherent <i>vs.</i> Incoherent Scattering	30
3.2	Dynamical Processes: the Neutron Window	31
3.2.1	Local Modes	32
3.2.2	Collective Excitations	33
3.2.3	Collective Dynamics in Liquids: Effective Eigenmode Model	36
3.3	Neutron Spectroscopy	38
3.3.1	Three-axis Spectrometry	38
3.3.2	Instrumental Setup	41
3.3.3	Influence of Instrumental Resolution	41
3.3.4	Data Treatment of Inelastic Energy-Scans	46

4	Single Component Model Membrane: DSPC-d70	49
4.1	X-ray Diffraction: Structural Phase Characterization	49
4.1.1	Experimental	50
4.1.2	Effect of Lipid Chain Length: Bilayer and In-plane Ordering	51
4.2	Neutron Scattering: Structure and Collective Dynamics	57
4.2.1	Sample Preparation and Experiment	57
4.2.2	Diffraction: Bilayer Repeat Spacing and Chain Correlation	58
4.2.3	Extracting Points of a Liquid Dispersion Curve	62
4.2.4	Summary and Conclusion	66
5	Cholesterol in Model Membranes	69
5.1	X-ray Diffraction: DMPC/Cholesterol Phase Diagram	69
5.1.1	Experimental	70
5.1.2	Temperature Dependence	71
5.1.3	Concentration Dependence	84
5.1.4	Summary and Conclusion	88
5.2	Neutron Scattering	91
5.2.1	Sample Preparation and Experiment	91
5.2.2	Neutron Diffraction: Specific Points in Phase Diagram	91
	Reflectivity: Bilayer Repeat Spacing	92
	Acyl Chain Correlation: In-plane Ordering	93
5.2.3	Collective In-plane Dynamics in a Composite Membrane	96
5.2.4	Discussion	104
5.3	Summary and Conclusion	106
6	Ethanol in Model Membranes	108
6.1	X-ray Reflectivity on Model Membranes	108
6.1.1	Sample Preparation and Environment	110
6.1.2	Effect of Ethanol concentration	111
6.1.3	Unbinding of DMPC-bilayers	113
6.1.4	Influence of Osmotic Pressure	115
6.2	Neutron Scattering	117
6.2.1	Sample Preparation and Experiment	117
6.2.2	Neutron Diffraction: In-plane and Bilayer Ordering	118
6.2.3	Influence of Ethanol on Collective In-plane Chain Dynamics	121
6.3	Summary and Outlook	122
7	Summary	123

A X-ray Experiments	127
A.1 WENDI-macros (SPEC)	127
A.1.1 SAXS- and WAXS-scans combined	127
A.1.2 temperature ramp	128
A.2 Data Treatment: Matlab	130
A.2.1 3d-plots	130
A.2.2 Evaluation of Temperature Ramps	131
A.2.3 Cuts through 3d-plots Shown	132
A.2.4 DMPC/Cholesterol Phase diagram	134
A.3 Osmotic Pressures induced by PEG 20000	138
B Neutron Experiments	140
B.1 Instrument Parameters (V2-Flex)	140
B.2 Macro Example (MAD)	142
B.3 Data Treatment: Matlab	143
B.3.1 Fit of Neutron Reflectivities	143
B.3.2 DMPC/Ethanol Bilayer Decay	144
B.4 Treatment of Inelastic Data	149
B.4.1 Energy-Scans: Detailed Balance Correction	149
B.4.2 Energy-Scans: Absorption Correction	149
B.5 Resolution Calculation with 'Rescal'	150
Bibliography	161

Abbreviations

Chemicals

DMPC: 1,2-dimyristoyl-sn-3-phosphatidylcholine

DPPC: 1,2-dipalmitoyl-sn-3-phosphatidylcholine

DSPC: 1,2-distearoyl-sn-3-phosphatidylcholine

DMPE: 1,2-dimyristoyl-sn-3-phosphatidylethanolamine

DMPC-d54: chain deuterated DMPC

DSPC-d70: chain deuterated DSPC

TFE: 2-2-2-Trifluoroethanol

PEG (20000): poly-ethylen-glycol (molecular weight in Dalton)

CPE: chemical permeation enhancer

Techniques

SAXS: small-angle x-ray scattering

WAXS: wide-angle x-ray scattering

TAS: (neutron) three-axis spectrometry

QENS: quasielastic neutron scattering

NMR: nuclear magnetic resonance

MD-simulation: molecular dynamics simulation

DSC: differential scanning calorimetry

Facilities

HMI: Hahn-Meitner Institut, Berlin (Germany)

ILL: Institut Laue Langevin, Grenoble (France)

ESRF: European Synchrotron Radiation Facility, Grenoble (France)

IRP: Institut für Röntgenphysik, Georg-August Universität, Göttingen (Germany)

Instruments

V2(-Flex): cold three-axis spectrometer, HMI

IN12: cold three-axis spectrometer, ILL

IN8: thermal three-axis spectrometer, ILL

ID2: combined SAXS and WAXS beamline, ESRF

WENDI: inhouse diffractometer (SAXS, WAXS)

Samples

MLV: multilamellar vesicle

Chapter 1

Introduction

Phospholipid membranes often serve as simple model systems to understand basic properties of their far more complex biological counterparts.

One of the most significant aims in membrane biophysics is to relate changes in composition of a model system as well as of the external parameters, to the specific functionality of the membrane. The most relevant external parameters are temperature, humidity, pressure or pH. Functional properties of a membrane depend equally on structural and dynamical properties. For example, the collective in-plane density fluctuations of the phospholipid chains, which are in the focus of the present work, have been shown to influence membrane permeability [1, 2]. Knowledge about the relationships between collective dynamics on one hand, and the resulting transport properties on the other hand, can then be useful for biomedical applications, such as drug delivery.

While molecular vibrations, conformational dynamics and diffusional processes are studied by a number of spectroscopic techniques over a broad range of time scales, such as e. g. nuclear magnetic resonance (NMR) [3, 4], incoherent inelastic neutron scattering (QENS) [5, 6] or dielectric spectroscopy, only very few experimental techniques can access the short range collective motions mentioned above. Chen et al. were the first to present an inelastic x-ray scattering study with a dispersion relation $\hbar\omega(Q_r)$ which quantifies the collective motion of the lipid acyl chains as a function of the lateral momentum transfer Q_r [7]. In the following years, Rheinstädter et al. have used inelastic neutron scattering for similar investigations of the collective in-plane chain dynamics [8], and pointed out several distinct differences between the two probes. These are related to the energy-momentum relations of neutrons and photons, which affect the respective energy-resolution, the accessible (Q, ω) -range, and the signal-to-noise ratio. Most importantly, the fact that the energy of the incident neutron beam with several meV lies in the range of the excitations, results

in an energy-resolution of up to $\approx 300 \mu\text{eV}$, compared to 1.5 meV for an inelastic x-ray experiment. The latter is a decisive advantage for a quantitative comparison of dispersion curves for lipid membranes, where high resolution is needed. On the other hand, the range at low Q and high ω , is not accessible by inelastic neutron scattering due to the dispersion of the neutron itself ($\sim Q^2$).

A detailed comparison between points of the dispersion relations of two single component lipid membranes is the starting point of this thesis: Chapter 4 presents the collective short wavelength dynamics in two single lipid model membranes, which exhibit distinctly different phase behavior. These differences become apparent in the temperature-dependence in the bilayer repeat spacing, as well the packing of lipid molecules in the plane of the membrane. So far, the different phase behavior has not been linked to the corresponding dynamical properties.

The insertion of the membrane-active molecule Cholesterol, which is known to regulate membrane fluidity, membrane permeability and the lateral mobility of proteins, is then a next step towards the understanding of collective dynamics in physiologically more relevant membrane systems (chapter 5). In order to first achieve a more complete description of the membrane on a molecular level, the temperature- and concentration-dependent structural changes in the phospholipid/Cholesterol-system have been studied by small- and wide-angle x-ray scattering. Secondly, the influence of Cholesterol on the collective short wavelength fluctuations of the phospholipid acyl chains was studied by inelastic neutron scattering. Sharp inelastic excitations have been observed in the composite membrane, which exhibit a surprisingly long life-time.

Next, composite model membranes containing Ethanol have been studied, in order to gain insight in the molecular mechanism underlying its function as a drug enhancer and anesthetic. Note, that the alcohol has a somewhat reverse effect on the in-plane ordering of lipid molecules than Cholesterol, due to its tendency to maximize the interfacial area between the bilayer and water. A structural characterization was performed by x-ray reflectivity measurements on highly oriented membrane samples in a liquid environment. An approach for a technically challenging inelastic neutron scattering experiment is introduced and first results are discussed.

The thesis is organized as follows: In the next chapter a general introduction into basic membrane properties and membrane dynamics is given, the specific model systems that were investigated, are introduced. In chapter 3 an overview over the neutron window for the observation of various dynamical processes in model membranes is given, before focussing on the picosecond time scale, and length scales of nearest neighbor distances. Technical aspects of the neutron three-axis technique and

its application to lipid membranes are presented. Chapters 4-6 are each dedicated to a specific model system and are subdivided into a structural characterization performed with x-rays and the simultaneous characterization of structure and dynamics by inelastic neutron scattering. Finally, chapter 7 presents a brief summary and conclusions of this work.

Chapter 2

Membranes and Membrane Dynamics

2.1 Biological Membranes

Various models of biological membranes have been introduced in the past. In 1877 Pfeffer was the first to propose the existence of a plasma membrane which covers the outer surface of cells, but also separates all aqueous environments of different composition from each other [9]. The well-known lipid bilayer structure as a model for a cell membrane was first introduced by Gorter and Grendel in 1925 [10].

A very successful model was introduced in 1972 by Singer and Nicolson who suggested that proteins are not only bound to the membrane surface, but can also span through it (Fig. 2.1). Since it was known from x-ray crystallography in the 1960's that many proteins exhibit an α -helical structure, they hypothesized that the hydrophobic amino acids in the helices might play a special role. In their famous *Fluid-Mosaic Model* they underline that some proteins could interact with the surrounding lipids and that, in turn, protein function could depend on the presence of specific lipids [11]. However, they proposed that lipids in the physiologically relevant fluid state form a matrix through which proteins can freely diffuse, including the formation of domains, but excluding long-range order or interactions of proteins.

As this picture does not fully match experimental observations, Mouritsen and Bloom suggested a slightly refined version of the model taking into consideration that lipids and proteins may distribute inhomogeneously and that not only domains, but also clusters form within the plane of the membrane. In their *mattress model* they take into account the influence of a mismatch in the hydrophobic length of different membrane constituents, for example for lipids and proteins or lipids of varying length in lipid mixtures [12]. In order to avoid energetically unfavorable hy-

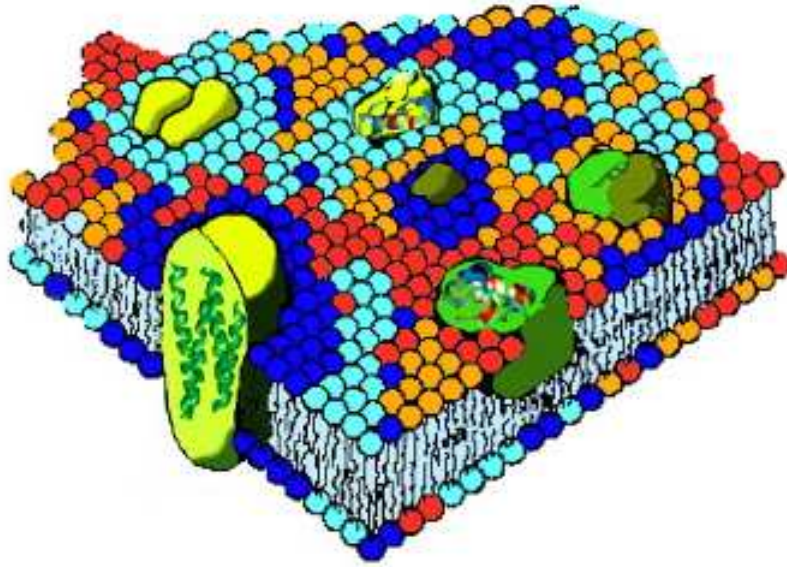


Figure 2.1: *Fluid-Mosaic Model* for membrane introduced by **Singer** and **Nicolson** [11].

drophobic interactions, deformations in the membrane can occur in order to shield hydrophobic molecular parts. This so-called 'hydrophobic matching' causes interfacial tensions between membrane constituents which can lead to the accumulation of certain lipid species or the mutual attraction of proteins. These in turn cause aggregation and clustering phenomena, as well as the formation of domains. This phase behavior determines the cooperativity of transitions in biological membranes, which is considered to be of extreme interest for regulation and signal transduction processes (cf. 2.4). The investigation of collective dynamical processes in simple model membranes is the main objective of the present work.

2.2 Model Membranes

In biological membranes complex compositions with hundreds of different lipids (and proteins) are found which vary significantly between different cells or even organelles of the same cell. Therefore it is commonly believed that the specific composition of a membrane is crucial to its unique function. The study of the structure and dynamics of simple model membranes consisting of one or two components is a key approach to investigate the link between a particular composition and a specific functionality. A change in the composition therefore naturally induces a variation in the structural organization in the membrane plane as well as in its bilayer ordering. This change reflects itself in the lipids' melting behavior as well as in the corresponding phase

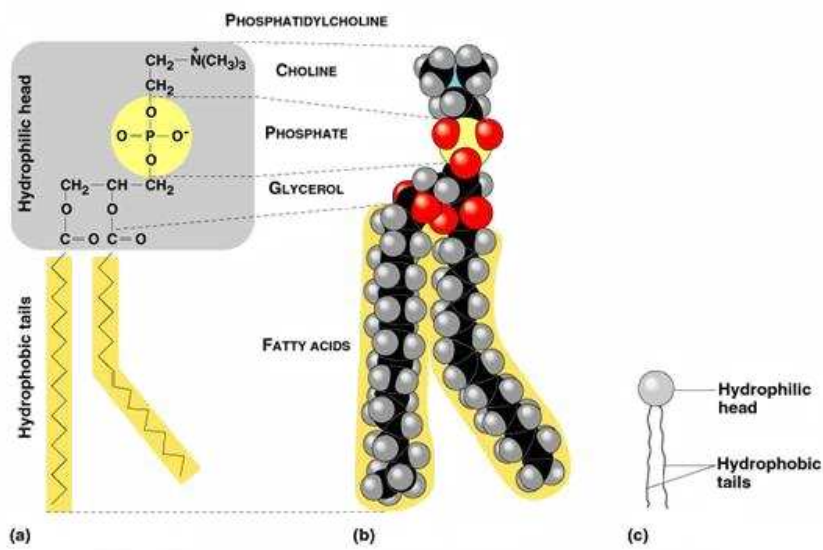


Figure 2.2: Phospholipid in different representations: (a) structure formula, (b) space-filling model, (c) phospholipid symbol.

transitions. The following sections will therefore give an overview over the lamellar structures that occur in single lipid membranes, as well as a brief general review over phase transitions that is needed later on for the discussion of the melting processes (cf. 2.2.3) observed in single lipid membranes (cf. 4).

2.2.1 Membrane Structure and Lamellar Phases

Phospholipids consist of a polar headgroup and unpolar acyl chains (see Fig. 2.2). In a polar medium, commonly water, they therefore tend to form aggregates which expose the headgroups and shield the unpolar hydrocarbon chains from the medium. Due to this hydrophobic effect the formation of specific aggregates is highly concentration dependent [13]. At high lipid concentrations the assembly into larger aggregates becomes more favorable.

Among the wealth of phases that occur we will in the following concentrate on the 'lamellar phases' in lipid membranes. Depending on sample preparation these occur in oriented extended two-dimensional bilayer sheets or in so-called vesicles which consist of one (unilamellar) or multiple (multilamellar) bilayers (Fig. 2.3). The phases exist in different states shown in Fig. 2.4 corresponding to their occurrence at increasing temperatures:

- L_c -phase: In this crystalline phase the lipid chains are arranged in the highly ordered *all-trans* configuration. The bilayers formed are not separated by a water layer as is the case in the L'_β -phase.

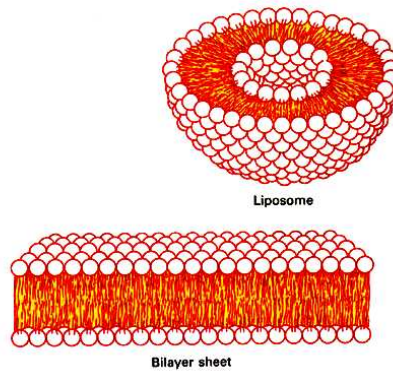


Figure 2.3: (*top*) cut through unilamellar vesicle (liposome); (*bottom*) oriented bilayer sheet.

- L'_β -phase: In the 'gel' phase the lipid chains are also arranged in the *all-trans* configuration (see 2.2.2). The prime index indicates a tilt of the headgroups with respect to the bilayer normal (Fig. 2.4, 2.12). This tilt is commonly found in phospholipids that have large headgroups with respect to their chain lengths, such as DMPC and DSPC. The high degree of chain order evokes a quasi crystalline hexagonal in-plane order of the lipid molecules. Therefore this phase is also referred to as the 'solid (ordered)' phase.
- P'_β -phase: The 'ripple' phase is an intermediate phase that occurs with increased temperature for some phospholipids. It shows characteristic one-dimensional ripples on the membrane surface (Fig. 2.4). These ripples are probably evoked by a partially molten lipid L_α -phase (see below) with a lower average degree of chain ordering than in the L'_β -phase. The crystalline in-plane order of the lipid molecules is therefore partially lost. The ripples are likely to be formed of periodic assemblies of linear gel (L'_β) and fluid (L_α) lipid domains [14, 15].
- L_α -phase: in the 'fluid' phase the lipid acyl chains are mostly disordered and all in-plane lattice order is of short range order (fluid like). Therefore this phase is sometimes also referred to as liquid-disordered L_d -phase.

2.2.2 Phase Transitions

In order to describe phase transitions theoretically, an order parameter ϕ representing a suitable thermodynamic macroscopic quantity is introduced [16]. The order of a phase transition is generally defined as the order of the lowest derivative of ϕ that

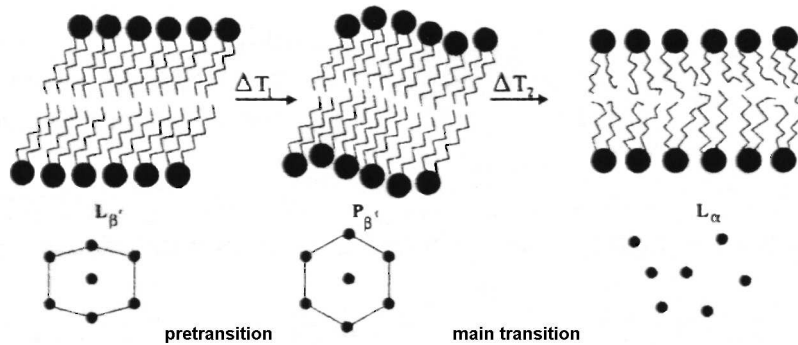


Figure 2.4: The lamellar phases in phospholipid model membranes display a decreasing order of the chains with increasing temperature (see text).

shows a discontinuity when passing through a coexistence regime. As differences between coexisting phases diminish with rising order of the transition, the first and second order phase transitions are of most practical interest.

First Order Phase Transition: A **first order** phase transition possesses the following characteristic features:

- A *latent heat* dQ is characteristic for the transition.
- Phases coexist during the transition.
- Entropy $S(T, p)$ and volume $V(T, p)$ exhibit a discontinuity at the transition temperature $T_c(p)$, which means entropy and volume have distinct quantities for each of the respective phases.

The latter means that the derivatives of $S(T, p)$ and $V(T, p)$, that are the isobaric heat capacity c_p and the isothermal compressibility κ_T as well as the isobaric compressibility κ_p are not defined at the transition T_c .

Second Order Phase Transition: A **second order** phase transition is characterized as follows:

- No latent heat is observed.
- No coexistence of phases occurs.
- $S(T, p)$ and $V(T, p)$ are continuous around the transition $T_c(p)$.
- The isobaric heat capacity c_p , the isothermal compressibility κ_T and the isobaric compressibility κ_p exhibit a discontinuity at $T_c(p)$.

A second order phase transition is typically accompanied by diverging fluctuations in the form of deviations around a mean value which occur during the transition. The isobaric heat capacity and the isothermal compressibility are linked to the occurring fluctuations according to the *Fluctuation-Dissipation Theorem*:

$$\begin{aligned} c_p &= \left(\frac{d\bar{H}}{dT} \right)_p = \frac{\overline{H^2} - \bar{H}^2}{RT^2} \\ \kappa_T &= -\frac{1}{V} \left(\frac{d\bar{V}}{dp} \right)_T = \frac{\overline{V^2} - \bar{V}^2}{V \cdot RT} \end{aligned} \quad (2.1)$$

This means, the isobaric heat capacity and the isothermal compressibility change according to the fluctuations in enthalpy H and volume V , respectively. Note, that in the case of membranes instead of volume fluctuations often lateral in-plane area fluctuations are regarded.

A system which undergoes a second order transition obeys the following laws:

- Near the transition temperature T_c the so-called *correlation length* $\xi(T)$, which is a measure for the length scale of specific interactions, diverges. For a number of systems the corresponding correlation function can then be described as:

$$g(\mathbf{r}, r') = c_0 \frac{\exp(-\frac{|r-r'|}{\xi(T)})}{|r-r'|} \quad (2.2)$$

This is called *Ornstein-Zernike behavior* [16]. The absence of a defined length scale when ξ diverges near the transition temperature T_c is referred to as *scale invariance*.

- As a consequence of the scaling invariance all thermodynamic quantities follow power laws near the critical temperature T_c according to:

$$f \sim \left| \frac{T - T_c}{T_c} \right|^\gamma \quad (2.3)$$

Here, γ denotes a so-called *critical exponent*.

- The divergence of the correlation length is accompanied by a so-called *critical slowing down*. This means characteristic time scales of dynamic processes increase near the phase transition.

2.2.3 Lipid Melting: Cooperativity and In-plane Correlation

For a specific single component phospholipid model membrane, the 'main phase transition' is induced at a defined temperature T_m at which equal amounts of lipids

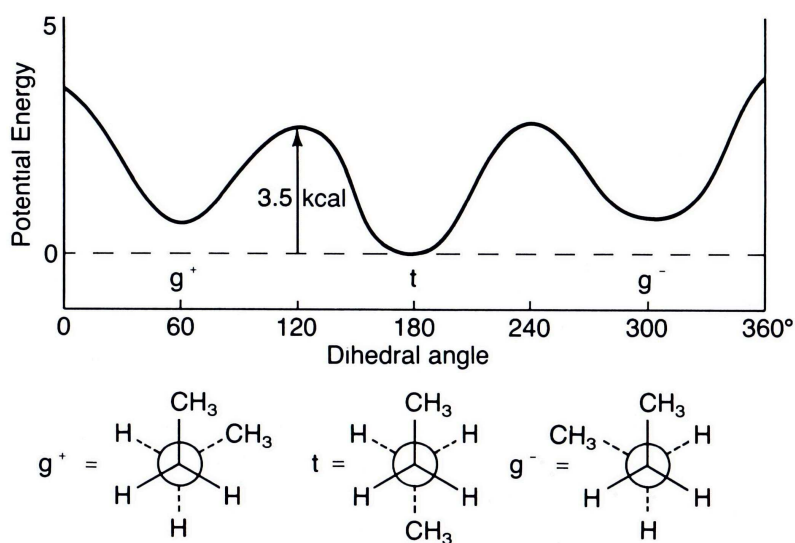


Figure 2.5: (*top*) Potential energy for rotation around a C-C bond in the phospholipid acyl chain; (*bottom*) Newman projection diagram of minimum energy conformations *gauche* (g^+ , g^-) and *trans* (t) of butane [17].

exist in the gel and in the fluid phase respectively. Well below this temperature in the $L_{\beta'}$ -phase the lipids are arranged on a lattice within the membrane plane (Fig. 2.4). This tight packing in the lipid 'gel phase' is due to the *all-trans* configuration of the acyl chains. Above the main phase transition temperature T_m this high degree of chain order is lost to a more random organization due to increased isomerizations in their carbon-carbon (C-C) bonds (Fig. 2.5).

The (low enthalpy) *all-trans* configuration is favorable for steric reasons. However, rotations around C-C bonds with $\pm 120^\circ$ evoke the second favorable so-called *gauche* conformations g^+ and g^- which lead to a characteristic change in enthalpy ΔH_{rot} . The angular changes between different neighbouring chain segments as well as the corresponding dependence of the potential energy of the hydrocarbon chain is shown in Fig. 2.5. Since the enthalpy cost of a single C-C rotation has a defined value, it is plausible that the characteristic melting enthalpy ΔH around the main phase transition shows a linear dependence on the lipid chain length (Fig. 2.7, (*left*): 1 kcal corresponds to 4.19 kJ).

The characteristic enthalpy ΔH accompanying the main phase transition can be obtained experimentally through differential scanning calorimetry (DSC) via integration of the recorded excess heat capacity curve: $\Delta H = \int_{T_0}^{T_1} \Delta c_p dT$. Examples of such heat capacity profiles obtained from samples consisting of unilamellar vesicles (cf. Fig. 2.3, (*top*)) of single lipids of increasing chain length (chapter 4) are shown

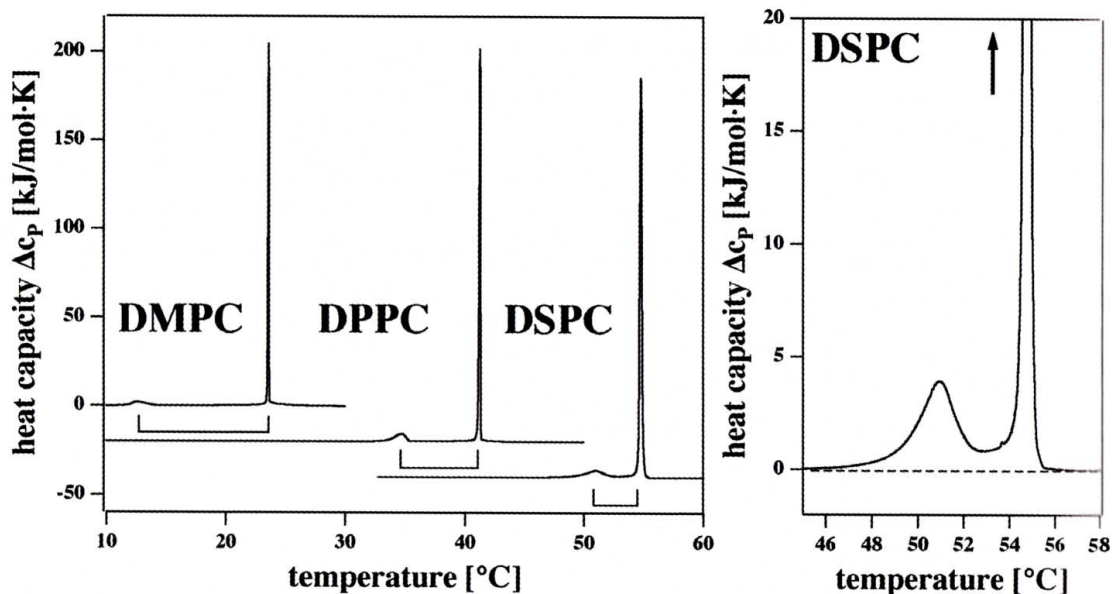


Figure 2.6: (*left*) Heat capacity profiles of three different phospholipids of increasing chain length: DMPC, DPPC and DSPC. The total area of the melting peak increases with increasing chain length, whereas the temperature interval between the pretransition and main transition decreases; (*right*) Magnification of the Δc_p -profile of DSPC [15].

in Fig. 2.6. In the case of DMPC, e. g., these vesicles have a diameter of 80 nm at room temperature. Obtained melting temperatures T_m and enthalpies ΔH are given in Table 2.1.

The small broad peak at the lower temperature corresponds to the lipid's pretransition between gel- ($L_{\beta'}$) and ripple-phase ($P_{\beta'}$), the sharp peak with the large amplitude to its main transition from the ripple to the fluid phase (L_{α}). A magnification of the Δc_p -profile is shown on the right. That the excess heat capacity does not return to the baseline between the two phase transitions is taken as an indication for the coupling of the two phenomena by Heimburg et al. [14, 15].

For all three lipids shown in Fig. 2.6 the melting transition occurs over a tem-

Lipid	Chainlength	T_m (°C)	ΔH (kJ/mol)
DMPC	14	23.6	23.9
DPPC	16	41.3	38.1
DSPC	18	54.7	50.7

Table 2.1: Melting enthalpies ΔH obtained from the integration of the heat capacity profiles around the main transition shown in Fig. 2.6 (excluding the pretransition peak), melting temperatures T_m obtained from the heat capacity maxima. Adapted from [15].

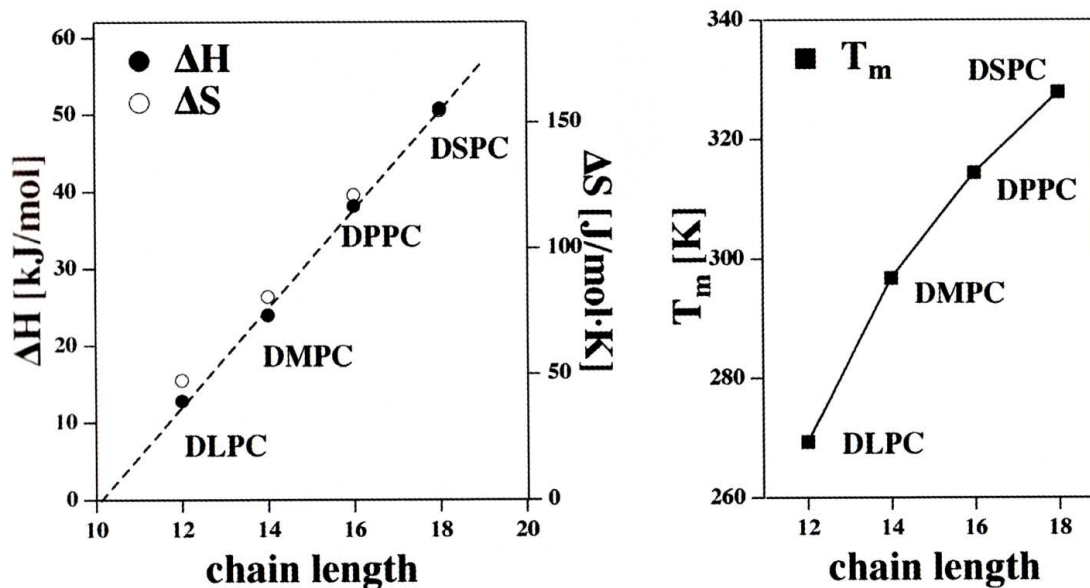


Figure 2.7: (*left*) Melting enthalpy ΔH and melting entropy ΔS show a linear dependence of the lipid chain length; (*right*) Melting temperature T_m as a function of the chain length exhibits nonlinear behavior [15].

perature range of less than 1°C . The characteristic width of theoretically calculated heat capacity profiles only match the corresponding experimental data if cooperative unit sizes in the order of 1000 lipid molecules are assumed [15]. Since the melting enthalpy ΔH shows a linear dependence on the chain length (Fig. 2.7, (*left*)), the nonlinear behavior of T_m vs chainlength (Fig. 2.7, (*right*)) can be explained by the cooperativity of the main phase transition. Therefore heat capacity profiles yield valuable information on the size of a distinct lipid's gel and fluid phase domains near the main phase transition, and thus the in-plane correlation of molecules. We will refer to this point in chapter 4, when discussing the effect of variable domain sizes on the corresponding collective in-plane dynamics.

2.2.4 Membrane Interaction Potentials

The (lamellar) repeat spacing D_z of oriented model membranes is determined by a balance of repulsive and attractive forces. For uncharged membranes the two predominant contributions to the overall potential are based on the attractive Van der Waals and the repulsive hydration force. The corresponding Van der Waals potential consists of a static and a dispersive contribution [18]. The static contribution (eq. 2.4) is for small membrane distances ($d_h \rightarrow 0$, cf. Fig. 2.8) often approximated

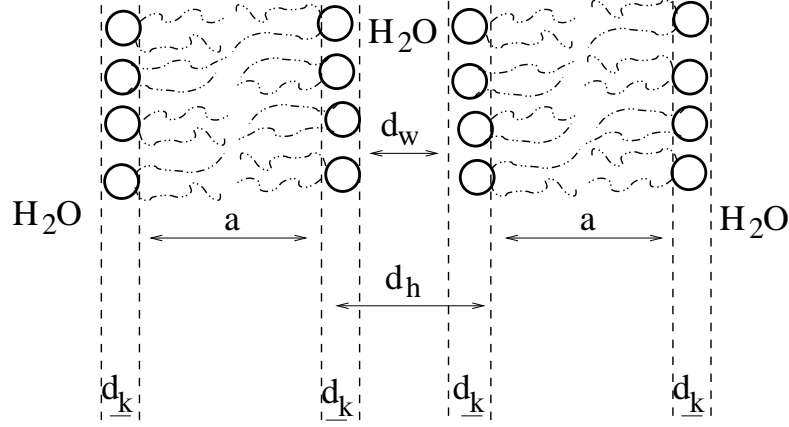


Figure 2.8: Definition of membrane and water layer spacings that can be obtained from analysis of electron density profiles derived from the reflectivity curves. The overall lamellar repeat spacing can be expressed as: $D_z = 2d_k + a + d_w = a + d_h$.

by two half-layers which are separated by a thin water film.

$$V_0(d_h, T) = \frac{H_{stat}(l_D)k_B T}{12\pi} \frac{1}{d_h^2} \quad (2.4)$$

Here, $H_{stat}(l_D)$ denotes the static Hamaker constant, l_D the Debye-Hückel length and d_h the distance between layers (Fig. 2.8). The dispersive contribution can be described according to (eq. 2.5) with a dispersive Hamaker constant $H_{dis} = 2 \sum_{n=0}^{\infty} \Delta_n^2$.

$$V_{dis}(d_h) = \frac{H_{dis}k_B T}{16\pi d_h^2} \left[1 - \frac{2}{1 + a/d_h} + \frac{1}{1 + 2a/d_h} \right] \quad (2.5)$$

In this equation, a stands for the length of a double chain (Fig. 2.8), Δ_n denotes the relative difference of the frequency-dependent dielectrical constants of the two media according to $\Delta_n = (\epsilon_{H_2O}(\omega_n) - \epsilon_{CH_2}(\omega_n)) / (\epsilon_{H_2O}(\omega_n) + \epsilon_{CH_2}(\omega_n))$ with a temperature-dependent angular frequency of $\omega_n = 2\pi k_B T n / (h/2\pi)$ [18].

The repulsive hydration force can be described by the empirical expression $V_{hyd}(d_w) = H_0 e^{-d_w/\lambda_h}$ where d_w denotes the water layer in between the membranes, H_0 typically lies in the order of a few $k_B T \text{ \AA}^{-2}$ and $\lambda_h \approx 2 \text{ \AA}$ [19, 20].

The overall potential between two DMPC bilayers as a sum of the Van der Waals Potential and the hydration potential is shown in Fig. 2.9.

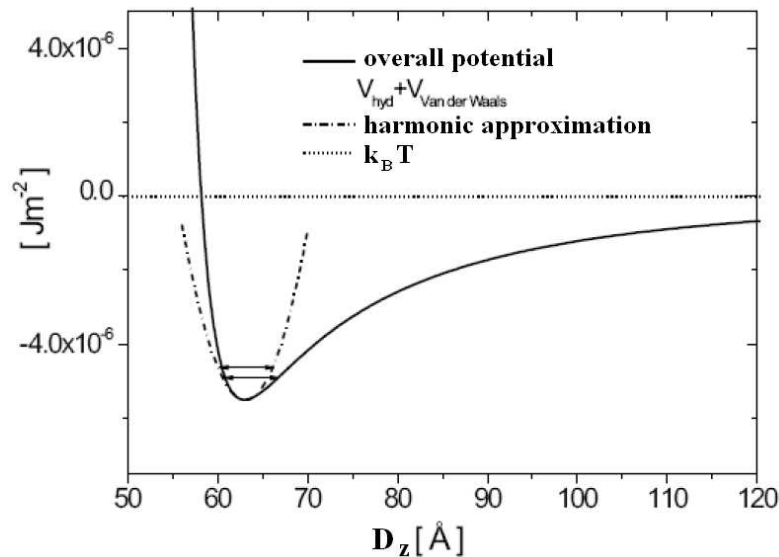


Figure 2.9: Potential between two DMPC bilayers as a sum of the Van der Waals Potential and the hydration potential, adapted from [19].

2.3 Single Lipid and Composite Model Membranes Studied

2.3.1 DSPC: Chain-length and Main Phase Transition

The main phase transition in phospholipid bilayers which occurs with the increase of temperature from the gel (P'_β) to the fluid (L_α)-phase is still not fully understood. The melting of the lipid acyl chains in DMPC has been investigated thoroughly. It shows a so-called 'pseudocritical' swelling (cf. Fig. 2.10 for explanation), in contrast to a continuous change of the lamellar D_z -spacing in the temperature regime of the main phase transition as well as of the interchain correlation peak above the main phase transition at T_m . Assuming a softening of the bilayer bending modulus K_B at T_m , it is possible to explain both the increasing fluctuations and the pseudocritical behavior of D_z close to T_m [21]. In fact, in a previous neutron backscattering study on the DMPC model membrane, a link between the critical swelling and the collective motions of the lipid's acyl chains has been suggested [22].

The inelastic neutron scattering experiment on a single lipid membrane (chapter 4) was carried out in order to investigate the validity of two likely scenarios regarding the nature of the main phase transition. This was achieved by measuring significant points in the short wavelength dispersion relation of DSPC in order to compare the results to the ones previously obtained for DMPC.

In the 'critical point scenario' (model I) a closely lying critical point is assumed near the main phase transition (cf. 2.2.1, 2.2.2), but the critical temperature is not

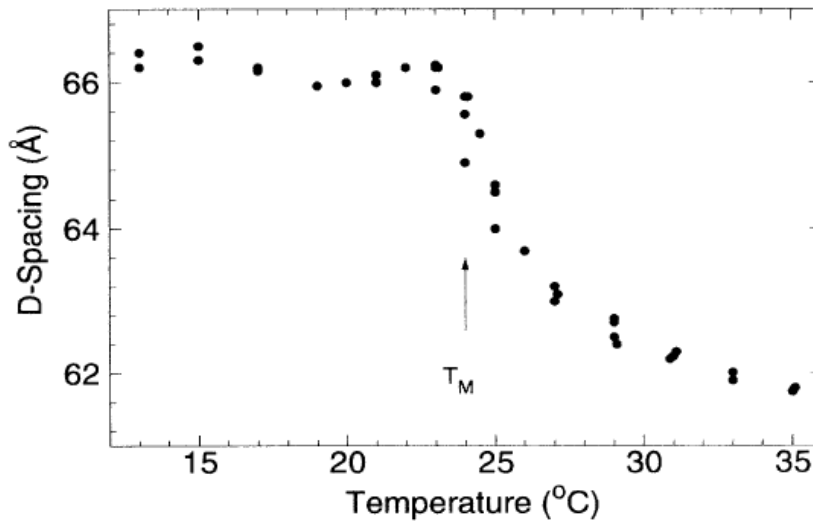


Figure 2.10: Temperature dependence of the D_z -spacing of fully hydrated unoriented bilayer suspensions of DMPC. The transition from the high temperature chain melted phase to the lower temperature ripple phase occurs at $T_m = 24^\circ\text{C}$ [23]. The deviation from linear behavior in the decrease of the lamellar repeat spacing with rising temperature is called 'anomalous' or 'pseudocritical' swelling.

reached experimentally before being cut off by a first order transition at $T_m > T_c$.

It has been discussed in the past, whether the appearance of the 'pseudocritical swelling' is connected to the formation of 'ripple' phase observed for certain phospholipids [21, 23, 24, 25]. For DMPC, e. g., a ripple phase is known to accompany the pseudocritical swelling, whereas for DSPC a ripple phase exists, but no critical swelling occurs. DMPE, on the other hand, shows critical swelling, but no ripple phase [25, 26]. Therefore, a direct coupling between the two phenomena can be excluded and it is possible to compare the single lipid membranes DSPC and DMPC, which both exhibit the 'ripple' phase. However, only the latter shows an anomalous swelling.

In the 'weak crystallization scenario' (model II) it is assumed that the phase transition is of a weak first order. This means it exhibits mostly properties of a first order transition, such as phase coexistence around the transition temperature. In analogy to solid state crystals, a soft mode at the position of the nearest neighbor peak in the short wavelength dispersion relation (Fig. 3.4) is believed to be a precursor of such a phase transition [8].

The finding of a soft mode in the single lipid membrane DSPC would therefore contradict a link between the pseudocritical swelling and the short wavelength density fluctuations and favor the 'weak crystallization scenario'.

2.3.2 Phospholipid/Cholesterol:

Cholesterol is a major constituent of eukaryotic cell membranes and is located mainly in the plasma membrane, naturally occurring in ratios of up to 50 mol% with respect to the lipids [27]. Its biological functions include the maintenance of proper fluidity [28, 29], formation of glyco-sphingolipid-Cholesterol enriched raft domains [30], reduction of passive permeability [31, 32, 33], and increasing the mechanical strength [34, 35, 36].

In order to be able to model the structure and dynamics of the composite system on a molecular level, it is crucial to understand how the sterol partitions into the membrane in defined temperature- and concentration regimes. Therefore, a brief introduction into the corresponding phase behavior is given in the following.

The DMPC/Cholesterol system can exist in one of two possible liquid phases: a liquid-disordered phase (L_d) at low Cholesterol concentrations, and a liquid-ordered phase (L_o) at high concentrations, with an intermediate region of the phase diagram where the two can coexist (cf. Fig. 2.11) at the same temperature and pressure [37, 38, 39, 40]. It is occasionally assumed that in the L_o -phase Cholesterol molecules span the hydrocarbon core of both leaflets of the bilayer in specific temperature regimes [6, 41], whereas in the L_d -phase they are packed like phospholipid molecules in each leaflet [39, 40, 42].

It has also been suggested, that the fluid phase immiscibility may create domains in biological membranes [43, 44]. The separation of domains of stable stoichiometric complexes could be an essential characteristic for some biochemical functions. Fluid-fluid immiscibilities are expected to occur in binary mixtures with large structural differences or when one component exhibits a characteristic headgroup tilt [41]. This is the case when the polar phosphatidylcholine headgroup (PC) is bulky with respect to the length of the lipid acyl chains (14 segments for DMPC, 16 for DPPC). When aggregating into a bilayer structure optimum in-plane packing is therefore ensured through a tilt of the lipid's headgroup against the bilayer normal (Fig. 2.12, (*left*)).

The Cholesterol molecule is largely unpolar (Fig. 2.12, (*right*)), since the hydroxyl group at the head represents less than five percent of the molecule's total mass and approximately a quarter of the surface exposed towards the water in between membrane layers. An exposure to the water layer is therefore even more unfavorable for the sterol molecules than an agglomeration of peer sterol molecules.

The 'umbrella' model introduced by Huang et al. is intended to give an explanation for the microscopic interactions that lead to a maximum solubility of Cholesterol in lipid bilayers [45]. It is based on the assumption that a minimization

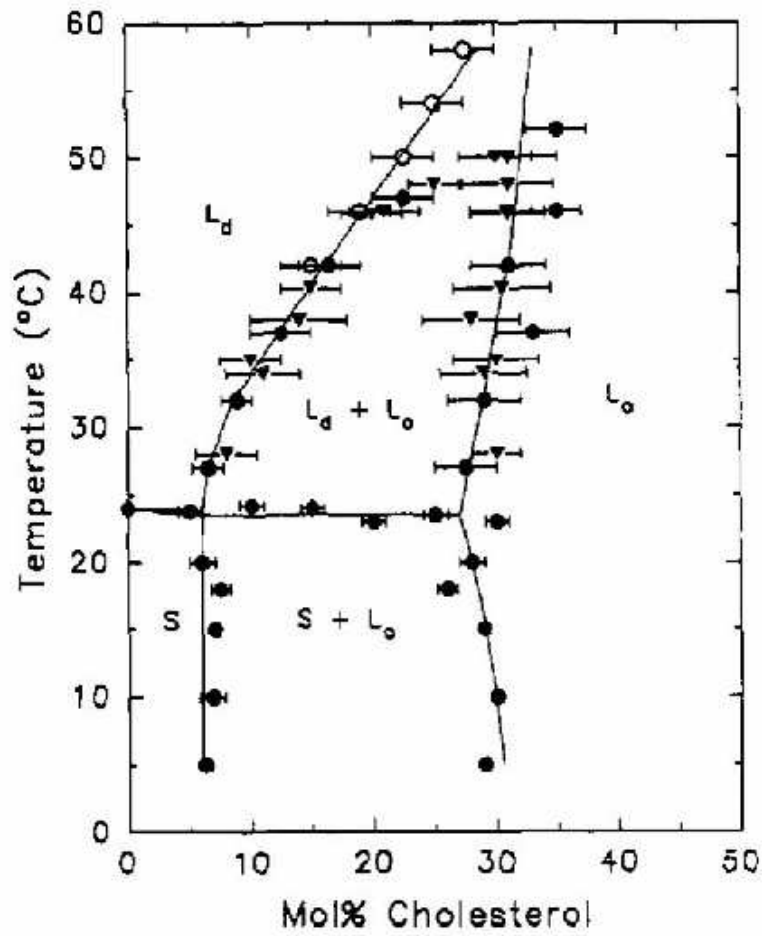


Figure 2.11: Phase diagram for DMPC/Cholesterol: points were obtained from the study of changes in the lateral diffusion of a phospholipid probe in a binary mixture by the fluorescence recovery after photobleaching technique [42].

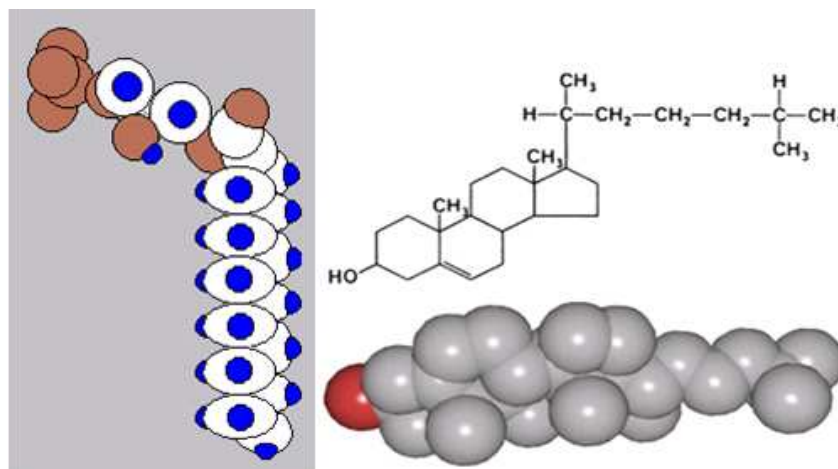


Figure 2.12: (*left*) A phospholipid molecule which consists of a comparably bulky head group with respect to the acyl chain length achieves optimum packing within a membrane bilayer structure through tilting its headgroup vs. the bilayer normal; (*right*) Cholesterol molecule.

of the free energy is reached, if the sterol is incorporated so that it shares the space under the phospholipid headgroup with the acyl chains. Therefore, the nonpolar part of Cholesterol is shielded from exposure to water by the lipid, much like by an 'umbrella'.

At low concentrations (<5mol%, L_d -phase) Cholesterol is loosely bound to the phospholipid's tilted headgroup by hydrogen bridge (Fig. 2.13, (*left*)). Therefore the lipid chains are found in a kink-conformation, much like in the pure lipids' fluid phase. As the sterol concentration increases, however, the liquid-ordered L_o -phase is at first only partially induced (cf. Fig. 2.11): in order to allow a tight packing and an equal arrangement of Cholesterol molecules along both lipid acyl chains, as well as further shielding from the surrounding water, the headgroup tilt ceases to exist and the chains resume to a configuration closely resembling the *all-trans* configuration (Fig. 2.13, (*right*)). If the Cholesterol concentration is increased beyond a limit where the shielding from water through the phospholipid 'umbrella' is possible, sterol molecules approach their second favorite binding partners and another phase consisting of Cholesterol monohydrate crystals [45].

A partial phase diagram of a DPPC/Cholesterol model membrane was investigated by Karmakar et al. using small-angle and wide-angle x-ray diffraction on oriented samples. They observe a sterol-induced modulated phase P_β at intermediate concentrations below the main phase transition temperature, that can be distinguished from the well-known ripple phase (P_β'), but is not found in membranes

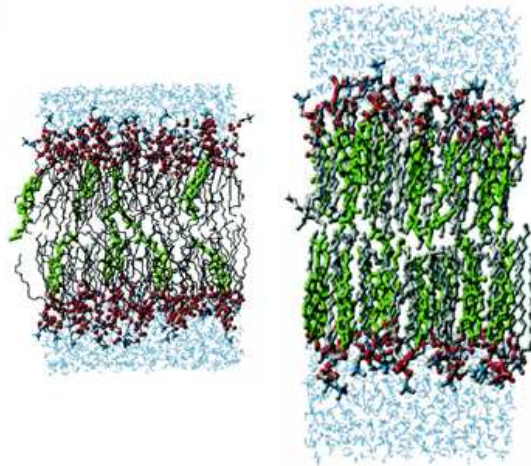


Figure 2.13: Snapshots of MD-simulations: DPPC with 11mol% Cholesterol (*left*) and 50mol% Cholesterol (*right*) at a temperature of $T = 50^{\circ}\text{C}$ and a pressure of $P=0$ atm with a duration of 2 ns for each run. Cholesterol molecules are represented by green sticks. [46].

which do not exhibit the $P_{\beta'}$ -phase without Cholesterol influence [47, 48, 49]. Similarities between the P_{β} -phase and the previously discussed coexistence of the lipids' solid S - and liquid-ordered L_o -phase are pointed out. Mortensen et al. also observe a phase dependent formation of ripples of varying wavelength λ in a neutron small angle scattering study on a DMPC/Cholesterol model membrane [50]. The imperfect miscibility of the two amphiphiles has also been studied with time-resolved small-angle x-ray diffraction by Richter et al. [41]. The authors propose a model in which lateral and vertical alignment of Cholesterol molecules are linked to an increase in the sterol concentration and temperature, respectively. Corresponding temperature- and concentration- dependent lateral and vertical diffusion processes of the sterol molecule have been observed with quasielastic neutron scattering [6, 51].

2.3.3 Phospholipid/Ethanol:

Ethanol exhibits two major functions in a model membrane: On the one hand, it enhances transdermal drug delivery by decreasing the barrier resistance of the initial layers of the stratum corneum (skin). Since the lipids are arranged in bilayer stacks due to the surrounding polar medium (water), the permeation of most drugs is seriously hindered. So-called chemical permeation enhancers (CPE's) promote drug delivery through the stratum corneum by decreasing the barrier resistance [52, 53, 54]. This means the physico-chemical nature of the skin membrane is reversibly altered for diffusion processes. Ethanol is a typical example of such a CPE. On

the other hand, Ethanol is also known to show properties similar to an anesthetic. The effect of an anesthetic is to induce a lateral pressure within the fluid membrane which can cause changes in the conformation of inserted membrane proteins and therefore alter their function [15, 55, 56]. Therefore the effect of osmotic pressure on the layer repeat spacing of membranes containing Ethanol is studied in section 6.1 prior to the corresponding collective in-plane dynamics in section 6.2.

As for the previously introduced composite system, the following overview over the occurring phases will be referred to in the discussion of a molecular model for the observed structure and dynamics when Ethanol is inserted into the membrane.

The influence of Ethanol on properties of different phospholipid model membranes has been investigated in several studies. For saturated phosphatidylcholines, Ethanol induces interdigitation of the lamellar gel phase at threshold concentrations that decrease with the lipid chain length [57]. A biphasic effect on the gel-liquid crystalline phase transition of the lipid multilayers is associated to this interdigitation. The temperature of this transition first decreases slightly, then increases when the Ethanol concentration exceeds the threshold concentration. For DMPC and DPPC the interdigitation threshold concentrations for vesicle solutions are 10.7 and 6.3vol% respectively. The results presented in this work were taken on **DMPC** with Ethanol.

With a variety of techniques Vierl et al. investigate a DPPC/Ethanol phase diagram by x-ray diffraction Fig. 2.14 [58]:

L_c -phase: Occurs below the so-called subtransition temperature (between 16 and 18°C) with a lamellar repeat distance of $63.0 \pm 0.5 \text{ \AA}$ in pure water and $62.4 \pm 0.5 \text{ \AA}$ in 2.0 M aqueous Ethanol.

$L_{\beta'}$ -phase: Below the pretransition temperature 1st, 2nd and 3rd order Bragg reflections occur with a lamellar spacing of $62.7 \pm 0.6 \text{ \AA}$.

$P_{\beta'}$ -phase: Between the pretransition and the main phase transition only two low angle x-ray reflections occur with a repeat distance of $61.7 \pm 1.5 \text{ \AA}$ (the 'ripple phase' corresponds to an undulation of the bilayers).

$L_{\beta_i'}$ -phase: At an Ethanol concentration lower than 0.7 M no qualitative effect is observed on the x-ray diffraction patterns apart from a shift of the lamellar spacing from 63 to 61 \AA with rising amounts of alcohol.

The pretransition temperature decreases with higher alcohol concentrations from 34°C in pure water to 28°C at 0.9 M Ethanol. At Ethanol concentrations larger than 0.7 M the chain melting main phase transition temperature is lowered by 1°C. In this case additional reflexes typical of a phase coexistence were observed.

Above 1.2 M Ethanol only reflexes appear, which correspond to an interdigitation

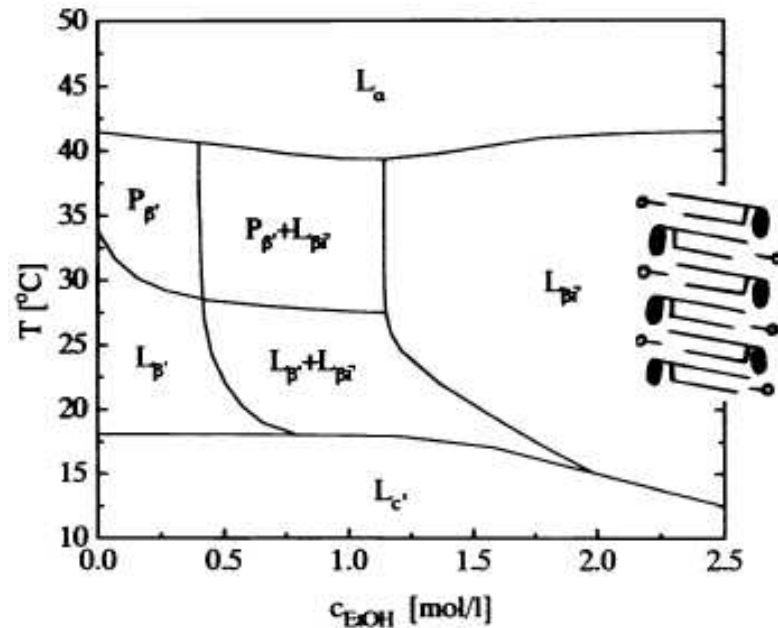


Figure 2.14: Phase diagram of DPPC in water/Ethanol-mixtures of varying concentrations as obtained from a combination of calorimetric, fluorescence, dynamic light scattering and x-ray diffraction measurements on vesicle solutions, adapted from [58].

of the lipid lamellae (Fig. 2.14). The D_z -spacing characteristic for this particular phase is $48.8 \pm 0.5 \text{ \AA}$.

L_α -phase: For temperatures above the main phase transition temperature two very sharp and intense reflections occur with a repeat distance of $67.5 \pm 1.1 \text{ \AA}$.

For the position of the Ethanol molecules at 12.5mol% and 30°C, Chanda et al. find a preferred location at the bilayer interface (cf. Fig. 2.15) [59]. Fig. 2.16 shows snapshots at the beginning and at the end of the simulation. Even Ethanol molecules originally placed within the layer's interior at the C6 atoms of the lipid chains migrate towards the glycerol backbone, the carbonyl groups and the first Methylene group (C2) of the lipid acyl chains.

Ethanol generally exhibits a strong affinity for the layer interface [60, 61, 62, 63]. This affinity can be related to the small difference between the molecule's hydrophobic and hydrophilic lengths in the membrane, which can be related to a distinct solubility towards hydrophobic (phospholipid chains) and hydrophilic (phospholipid heads, water) components (Meyer-Overton rule). In this respect, Ethanol and Cholesterol in a membrane have reverse influence on the molecular ordering of lipids with rising concentrations: while Cholesterol moves inside the bilayer leaflets to avoid contact with membrane water and therefore minimizes the layer interface (L_σ -

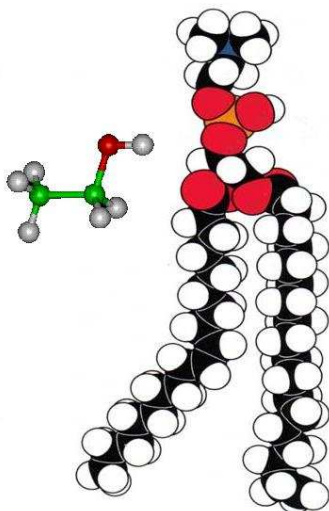


Figure 2.15: (*left*) Ethanol consists of a polar OH-group and an unpolar rest. The preferred position with respect to a neighboring phospholipid (*right*) is therefore at the molecular interlink between the lipids polar headgroup and its unpolar chains.

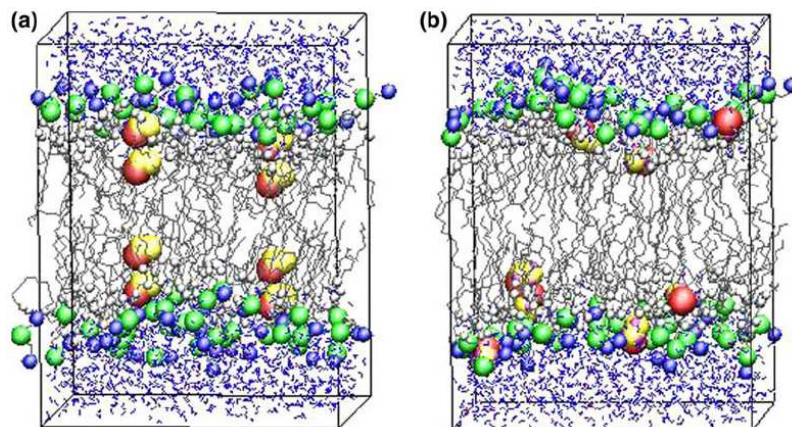


Figure 2.16: MD-simulation for DMPC with 12.5mol% Ethanol at 30°C (full hydration, constant pressure). Ethanol molecules and the lipid head group phosphorus (P) and nitrogen (N) atoms are drawn as large spheres. The atom coloring corresponds to blue for N, green for P, red for O (Ethanol), gray for O (lipid), yellow for C (Ethanol), silver for C (lipid) and water molecules in blue. After a total equilibration time of 870 ps, the actual simulation was performed for 4 ns. Snapshots show the beginning (a) and the near end (b) of the MD simulation [59].

phase), Ethanol seeks both, hydrophilic and hydrophobic, contact and therefore maximizes the layer interface ($L_{\beta'}$ -phase).

2.4 Collective In-plane Dynamics: Biological Membranes

2.4.1 Transmembrane Transport of Molecules

Correlated molecular motions play an important role for different biological functions of a membrane. Specifically the collective movement of the lipid acyl chains due to thermal fluctuations has been linked to the transport of small molecules through the bilayer [1, 64]. Nagle et al. investigate the passive sodium permeability of pure lipid vesicles, which has a large peak at the bilayer phase transition temperature [2]. They link the phenomenon to density fluctuations in the plane of the membrane, that open cavities in the headgroup region through which small ions can enter. In a thermodynamic approach, the *Fluctuation-Dissipation Theorem* is used to express the lateral area compressibility κ_T as a function of the in-plane pair correlation function $g(r) \propto e^{-\frac{r}{\xi_r}}$ and thereby link it to specific area fluctuations. These fluctuations, far from the main transition, determine the membrane's passive permeability to small molecules, such as sodium.

2.4.2 Nerve Pulse Propagation

In an electrochemical approach the well-known Hodgkin-Huxley model relates nerve pulse propagation to ion currents through specific resistors, so-called ion channels [65]. Heimburg et al., on the other hand, explain mechanical forces and dislocations as well as temperature responses of nerve membranes in-phase with the action potential on the basis of an adiabatically propagating reversible density wave triggered by a 'piezoelectric' impulse [15, 66]. They have previously shown that heat capacity changes in simple phospholipid model systems can be related to changes in the lateral compressibility of the membranes. This is the case not only for model systems, but also for biological membranes, such as for example *Escheria coli* or lung surfactant [67, 68, 69].

Neural tissue membranes are known to contain large quantities of Cholesterol and saturated phospholipids such as DMPC, as well as a significantly smaller number of (poly-) unsaturated phospholipids [70]. Studying the collective in-plane density fluctuations of the most simple composite membrane resembling such tissue membranes, can therefore directly yield distinct information on the functionality of a model system that could also apply to a significant number of natural membranes.

Chapter 3

Collective Dynamics in Model Membranes

The neutron is an ideal probe to study soft condensed matter due to its deep penetration of a sample without causing radiation damage upon the long counting times necessary for inelastic measurements. The neutron was first discovered by Chadwick in 1932 and exploited for Bragg diffraction on solids by using low-flux Ra-Be sources [71]. The latest generation of high-flux reactors such as the one at the Institut Laue-Langevin (ILL in Grenoble, France) came into existence in the early 1970's and made inelastic neutron scattering studies more practical.

In the present chapter various aspects of applying inelastic neutron scattering to investigate (collective) membrane dynamics are introduced. After a short general review of the corresponding scattering theory, an overview over collective and local modes accessible with neutron spectroscopy is given. The focus is then shifted to the modeling of the collective short wavelength dynamics within hydrodynamic theory, as well as to the neutron three-axis spectrometry as an experimental technique used.

3.1 Inelastic Neutron Scattering

3.1.1 The Scattering Cross Section

When neutrons are scattered by matter, the process is generally characterized by a momentum \mathbf{Q} and energy $\hbar\omega$ transfer between sample and probe. The corresponding conservation laws can be expressed as a function of the wave vectors of the incoming and scattered neutrons \mathbf{k}_i and \mathbf{k}_f :

$$\begin{aligned} \mathbf{Q} &= \mathbf{k}_i - \mathbf{k}_f && \text{momentum} \\ \hbar\omega = E_i - E_f &= \frac{\hbar^2}{2m}(k_i^2 - k_f^2) && \text{energy} \end{aligned} \quad (3.1)$$

If the energy transfer $E_i - E_f$ is zero, elastic scattering occurs, otherwise the process is inelastic.

In an (inelastic) neutron scattering experiment at a known incident Energy E_i and wave vector k_i the quantity of interest is the rate of neutrons scattered into a given solid angle $d\Omega_f$ in the direction of the wave vector \mathbf{k}_f with a final energy between E_f and $E_f + dE_f$. This rate is typically expressed by the product of the flux incident on a sample $\phi(\mathbf{k}_i)$ and the double differential cross section. If V is the interaction operator for the neutron with the sample and the initial and final states of the sample are labeled by quantum numbers λ_i and λ_f , the differential cross section can be expressed as [72]:

$$\frac{d^2\sigma}{d\Omega_f dE_f} = \frac{k_f}{k_i} \left(\frac{m_n}{2\pi\hbar^2} \right)^2 |\langle \mathbf{k}_f \lambda_f | V | \mathbf{k}_i \lambda_i \rangle|^2 \delta(\hbar\omega + E_i - E_f) \quad (3.2)$$

Since on a length scale of neutron wavelengths, typically \AA , the effective interaction is weak due to the short range of the nuclear potential, typically in fm, scattering is isotropical and can be described by a scalar, the nuclear scattering length b . It is related to the total scattering cross section according to $\sigma = 4\pi b^2$.

The Fermi-Pseudopotential $V(\mathbf{r})$ describes isotropical scattering in the Born approximation (eq. 3.3):

$$V(\mathbf{r}) = \frac{2\pi\hbar^2}{m_n} \sum_l b_l \delta(\mathbf{r} - \mathbf{r}_l) \quad (3.3)$$

In this equation \mathbf{r}_l is the position of the l -th nucleus for which the short range interaction potential is approximated by a delta function.

In a scattering experiment one generally averages over initial states and sums over final states. If $P(\lambda_i)$ is the statistical weight factor for the initial state, the differential cross section becomes:

$$\frac{d^2\sigma}{d\Omega_f dE_f} = \frac{k_f}{k_i} \sum_{\lambda_i, \lambda_f} P(\lambda_i) \left| \left\langle \lambda_f \left| b \sum_l e^{i\mathbf{Q}\mathbf{r}_l} \right| \lambda_i \right\rangle \right|^2 \delta(\hbar\omega + E_i - E_f) \quad (3.4)$$

With the neutron scattering function $S(\mathbf{Q}, \omega)$ (eq. 3.5), the double differential cross

section in the Van Hove formalism can be expressed as (eq. 3.6) [73]:

$$S(\mathbf{Q}, \omega) = \frac{1}{2\pi\hbar N} \sum_{l'} \int_{-\infty}^{\infty} dt \langle e^{-i\mathbf{Q}\mathbf{r}_{l'}(0)} e^{i\mathbf{Q}\mathbf{r}_l(t)} \rangle e^{-i\omega t} \quad (3.5)$$

$$\frac{d^2\sigma}{d\Omega_f dE_f} = N k_f k_i b^2 S(\mathbf{Q}, \omega) \quad (3.6)$$

In (eq. 3.5), N is the number of nuclei, t is the time and the brackets denote the average over the initial states. The scattering function depends only on momentum and energy transferred from a neutron to the sample, not on absolute values of k_i and k_f itself. The aim of an inelastic neutron scattering experiment is to measure $S(\mathbf{Q}, \omega)$ which contains both information on the positions as well as the motions of atoms comprising the sample in order to determine the microscopic properties of the system under investigation.

3.1.2 Coherent vs. Incoherent Scattering

In general one always obtains an incoherent and a coherent scattering contribution in any neutron experiment. Therefore one usually measures two different scattering cross sections. The difference can be understood looking at a monoatomic sample consisting of different isotopes, which each have distinct scattering lengths. For isotopes with a nuclear spin the scattering length depends on whether it is parallel or antiparallel to the neutron spin. Let us assume, for instance, the r th distinct isotope or nuclear spin state has the scattering length b_r , occurs with frequency c_r and correlations between nuclear position and scattering length can be omitted. Then scattering, which depends on the relative positions of the atoms, is described solely by the average (or coherent) scattering length $\bar{b} = \sum_r c_r b_r$ and therefore the average coherent cross section per atom $\sigma_{coh} = 4\pi(\bar{b})^2$.

Random deviations from a scattering average, on the other hand, will not give a contribution to collective scattering, only to the incoherent scattering. In this case the total cross section is given by $\sigma_{scat} = 4\pi \sum_i c_i b_i^2 = 4\pi\bar{b}^2$. Therefore, with $\sigma_{inc} = \sigma_{scat} - \sigma_{coh}$ the incoherent scattering cross section and the effective incoherent scattering length can be obtained as:

$$\begin{aligned} \sigma_{inc} &= 4\pi (\bar{b}^2 - \bar{b}^2) = 4\pi \overline{(b - \bar{b})^2} \\ &\Rightarrow b_{inc} = \sqrt{\overline{b^2} - \bar{b}^2} \end{aligned} \quad (3.7)$$

Table 3.1 shows examples of the coherent and incoherent scattering lengths and cross sections for the elements most common in phospholipid model membranes.

	Scattering length (10^{-15} m)		Scattering Cross Section (barns)	
	coh	inc	coh	inc
^1H	-3.74	25.2	1.76	79.0
$^2\text{H}=\text{D}$	6.67	4.03	5.60	2.04
C	6.65	0	5.55	0
N	9.37	1.98	11.0	0.49
O	5.81	0	4.23	0
P	5.13	0.2	3.3	0.01

Table 3.1: Scattering length and cross sections for elements found in phospholipid samples [74].

As one can see, most elements have significant coherent cross sections, except for hydrogen, for which the incoherent scattering is large and dominant. An incoherent cross section equal to zero is found only for single isotopes with zero nuclear spin.

For the coherent scattering of a sample consisting of a single element one can express the neutron scattering function using the Van Hove definition of the atomic density operator [73]:

$$\rho_{\mathbf{Q}}(t) = \sum_l e^{i\mathbf{Q}\cdot\mathbf{r}_l(t)} \quad (3.8)$$

This expression can be inserted into (eq. 3.5), which leads to:

$$S(\mathbf{Q}, \omega) = \frac{1}{2\pi\hbar N} \int_{-\infty}^{\infty} dt e^{-i\omega t} \langle \rho_{\mathbf{Q}}(0) \rho_{-\mathbf{Q}}(t) \rangle \quad (3.9)$$

Therefore the coherent part of the scattering function, representing cooperative effects, is a Fourier-transform of the space- and time-dependent pair-correlation function [72]. It can be shown that the incoherent contribution, which stands for individual particle motion is a Fourier-transform of the space- and time-dependent autocorrelation function.

3.2 Dynamical Processes: the Neutron Window

The spectrum of fluctuations in biological membranes ranges from the long wavelength undulation and bending modes of the bilayer with typical relaxations times of nanoseconds and lateral length scales of several hundred lipid molecules to the short wavelength density fluctuations in the picosecond range on nearest neighbor distances of lipid molecules. Within this broad frame three-axis spectrometry probes

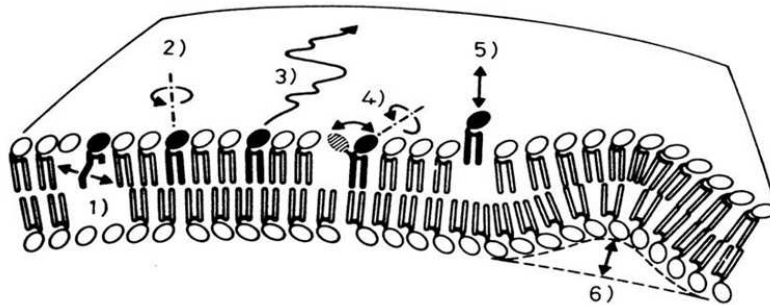


Figure 3.1: Motional processes in lipid bilayers consist of: 1) chain defect motions; 2) rotational diffusion of lipid molecules about their long molecular axis; 3) lateral diffusion of lipids in membrane plane; 4) rotational and flip-flop motion of lipid head groups; 5) vertical vibrational motion of the lipid molecules; 6) collective undulations of the bilayer [5].

distances of lipid molecules, lipid acyl chains and water molecules and propagating modes in the picosecond range [75, 76].

In general, membrane dynamics are characterized by a hierarchy of motional processes, of which the neutron window shall be described in the following.

3.2.1 Local Modes

Among the different dynamical processes of single lipid molecules are chain defect motions, rotational and lateral diffusion in the membrane plane, rotation and flip-flop motion of the lipid head groups as well as vertical vibrational motion out of the membrane plane (Fig. 3.1).

An early study of the incoherent quasielastic scattering investigated the local motions of lipids in fluid and gel-phase bilayers in terms of various diffusional processes observable.

Measuring in the in-plane geometry, the rotational motion of a whole lipid with a diffusion constant of $D_R = 5.6 \cdot 10^{10} \text{ s}^{-1}$ could be identified using the time-of-flight technique, the translational motion with a diffusion constant of $D_L = 1.8 \cdot 10^{-7} \text{ cm}^2 \text{ s}^{-1}$ in a backscattering experiment [5]. The study also states that a consistent interpretation of the findings of both types of scattering techniques at once was only possible assuming an additional collective motion at the time assessed to a bilayer undulation in the direction perpendicular to the bilayer plane (cf. 3.2.2).

Later high energy resolution studies not only analyze fast relaxations associated with diffusion processes of lipid and water molecules, but also find slower relaxations that can be related to collective dynamics [22, 77]. In a recent backscattering study

performed within the work of this thesis, selective contrast matching by alternating partial deuteration of lipid chains and intermembrane water, was used to distinguish between coherent and incoherent scattering contributions of both components. Here, on length scales of ns, slow collective motions of the lipid acyl chains were identified [78].

3.2.2 Collective Excitations

Bilayer Undulations: Collective undulations of the phospholipid bilayers can be probed using the neutron spin-echo method. It allows the analysis of thermally excited shape fluctuations in solid supported multilamellar lipid membranes. The underlying experimental dispersion relation $\tau^{-1}(q_{\parallel})$ is described as a function of the lateral momentum transfer q_{\parallel} . While three-axis spectrometry probes discrete molecular distances (the phospholipids' acyl chain correlation length), the bilayer displacement u_n corresponding to the dynamics observed with neutron spin-echo is described as a continuous variable [79].

An intermediate scattering function obtained from the density distribution in the sample is directly measured (eq. 3.10):

$$S(\mathbf{q}, t) = \int d^3\mathbf{R} e^{i\mathbf{q}\cdot\mathbf{R}} \int d^3r \langle \rho(\mathbf{r}, 0) \cdot \rho(\mathbf{r} + \mathbf{R}, t) \rangle \quad (3.10)$$

For a simple single lipid model membrane of DMPC this normalized intermediate scattering function was first obtained on the spectrometers IN11 and IN15 at the ILL and yielded two specific exponential decays within a q_{\parallel} -range of 0.002 \AA^{-1} and 0.08 \AA^{-1} , which correspond to relaxation processes on time scales of 10 ns and 100 ns respectively [79]. The faster process can be linked to collective undulations, the slower to a surface relaxation mode.

To describe the experimental results for the dispersion relation of the fluid L_{α} -phase (Fig. 3.2,b)), a theoretical expression that depends on the elastic coefficients B and K , which determine the compressional and bending modes of the smectic phase and are summarized to the smectic penetration length $\Lambda = \sqrt{K/B}$, the bilayer bending rigidity κ , the finite size of the lipid film D as well as the transport coefficient μ can be used (eq. 3.11):

$$\tau^{-1}(q_{\parallel}) = \frac{\kappa/d}{\eta_3} q_{\parallel}^2 \cdot \frac{q_{\parallel}^4 + [\pi/(\Lambda D)]^2}{q_{\parallel}^4 + \frac{1}{\mu\eta_3} (\pi/D)^2} \quad (3.11)$$

It is therefore possible to explicitly derive distinct quantities of the phospholipid model membrane by analyzing the undulation dynamics.

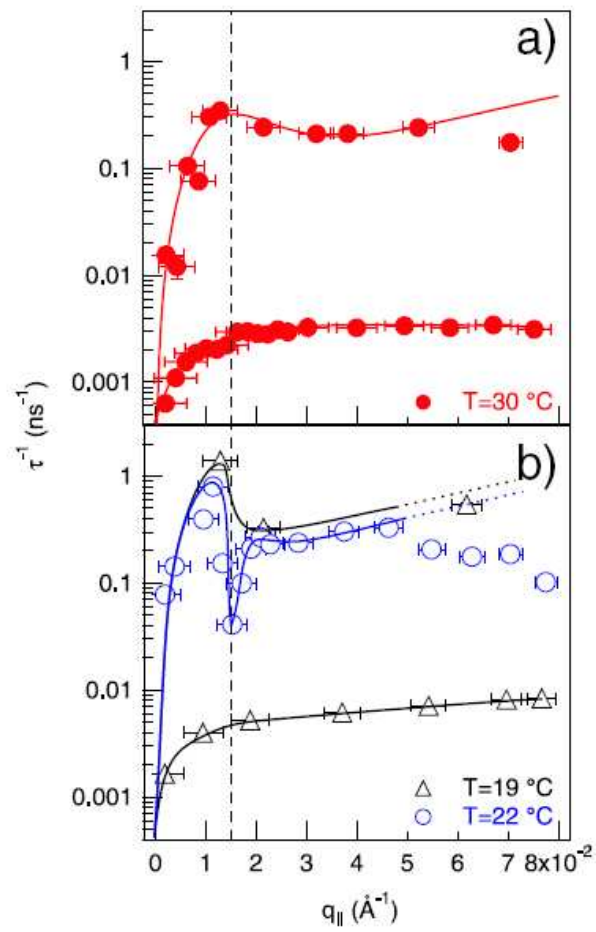


Figure 3.2: (a) Dispersion relations at $T=30^{\circ}\text{C}$, (b) Dispersion relations in the gel (19°C) and in the fluid phase (22°C) [79].

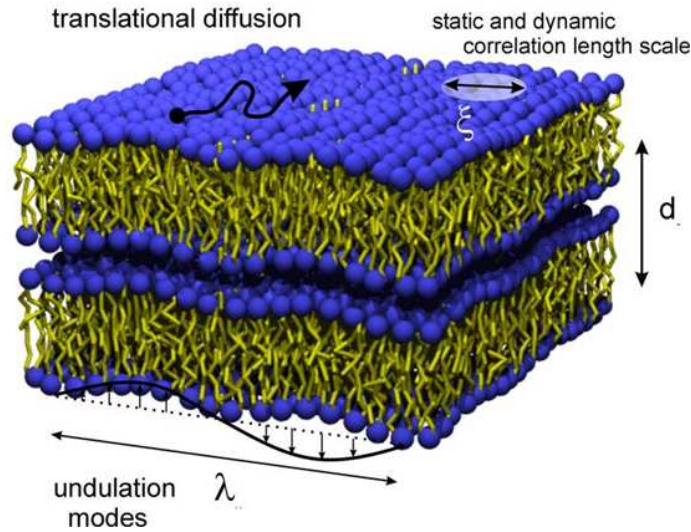


Figure 3.3: Collective dynamics as observed in model membranes: bilayer undulations and large scale in-plane density fluctuations.

Collective Short Wavelength Fluctuations The collective short wavelength in-plane density fluctuations of the lipid acyl chain segments can be described as sonic waves which are damped upon propagation through the membrane plane. The existence of a liquid dispersion curve with a minimum at the nearest neighbor distance has been previously predicted in MD-simulations [80] for DMPC and was first observed for several lipid membranes by inelastic x-ray scattering [7, 81]. Inelastic neutron scattering has, however, proven to be better suited to resolve distinct and characteristic dispersion curves due to a higher energy resolution around the position of the phospholipid nearest neighbor peak [8].

Fig. 3.4 shows the dispersion relations of the lipid bilayers in the gel (P_β) and in the fluid (L_α) phase at 18° and 30°C respectively. They were determined from inelastic energy scans at several constant Q -values between 0.9 and 3 \AA^{-1} . The shape of the dispersion function resembles that of an ideal liquid, such as liquid argon or helium [82, 83, 84] and can be understood qualitatively: At small Q -values the long-wave longitudinal sound wave is excited with $\omega \sim Q_r$. After going through a minimum at $Q_0 \approx 1.4 \text{\AA}^{-1}$ the dispersion saturates. Interestingly, the position of the minimum corresponds exactly to the peak position of the acyl chain correlation peak, similar to the de Gennes narrowing described for perfect gases [85]. This can be explained, if Q_0 is seen as a quasi-Brillouin zone in a two-dimensional liquid. Since collective modes with a wavelength ($2\pi/Q_0$) equal to the distance of the nearest neighbor are energetically favorable on this length-scale, they lead to a minimum

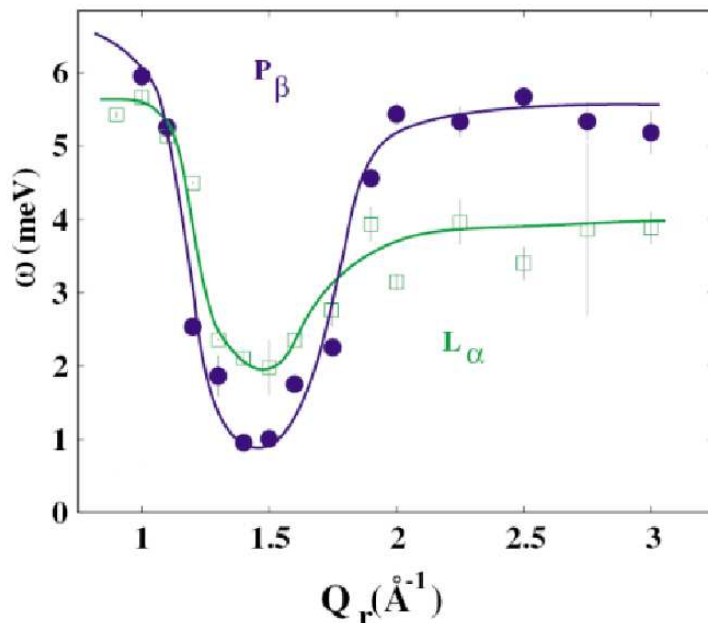


Figure 3.4: Dispersion relation as found for DMPC in the gel (P_β , 18°C) and in the fluid (L_α , 30°C) phase [8].

in the dispersion relation. At large Q -values one primarily observes single-particle behavior. The energy values of the maximum and the high- Q -region are higher in the gel than in the fluid phase (Fig. 3.4), due to a stiffer coupling of the lipid chains, whereas the minimum occurs at lower energy values. Analogous to a soft mode in crystalline systems, the existence of such a dispersion minimum is occasionally regarded as a precursor of a first order phase transition [8].

The main phase transition itself as well as the influence of the length of the lipid acyl chains on the collective short wavelength dynamics are investigated in the following chapter. Up to this point, the merit of neutron spectroscopy for studying properties of a single specific lipid model membrane (DMPC) was introduced using a broad range of inelastic neutron scattering techniques. The work presented in the following focusses on a smaller frame in (Q, ω) -space covered by the three-axis technique which is used to investigate the influence of variations in the composition of model membranes on the modulation of collective in-plane density fluctuations.

3.2.3 Collective Dynamics in Liquids: Effective Eigenmode Model

The three-effective eigenmode model describes dynamical processes on a molecular scale in atomic fluids, which can be observed with dynamic light scattering, inelastic x-ray and neutron scattering likewise [80, 81, 86, 87, 88]. The basic idea can be understood picturing the fluid as a giant molecule which receives or imparts thermal

excitations from the incident radiation. These excitations are visible in the scattered radiation and can be interpreted assuming the fluid exhibits the dynamic behavior that matches the existence of a few effective eigenmodes. The corresponding eigenvalues determine the decay of excitations when they are real, and their propagation when they are complex.

The experimentally obtained dynamic structure factor $S(Q_r, \omega)$ can be equivalently represented by its time Fourier transform, the intermediate scattering function $G(Q_r, t)$, which can be represented as a sum of three exponentials. The respective exponents are the eigenvalues, their respective intensities are determined by the eigenfunctions of the three effective eigenmodes of the fluid.

The model originates in the theory of Landau and Placzek for the light scattering of fluids, which explains the Rayleigh-Brillouin triplet lines observed in the spectrum of light. Here, it is assumed that the wavelength of the incident light is much larger than the size of the atoms, so that many atoms would be comprised in a wavelength. This assumption in general does not hold for whole lipids with sizes in the range of several Å's and neutron wavelengths in the order of Å's. The membrane plane can, however, be sliced into layers, which can be described as 2-dimensional liquid crystals. This way, single acyl chain segments can be considered similar to independent particles of a liquid described by de Gennes [89, 90]. This means, the time evolution of these chain segments can in good approximation be described by the equations of hydrodynamics, that is as if they move like particles in macroscopic flow, according to:

$$\frac{\partial}{\partial t} \mathbf{G}(Q, t) = -\mathbf{H}(Q) \mathbf{G}(Q, t) \quad (3.12)$$

which implies (eq. 3.13)

$$\mathbf{G}(Q, t) = \exp \{-t\mathbf{H}(Q)\} \quad (3.13)$$

With $G_{jl}(Q, 0) = \delta_{jl}$ for $(j, l = 1, 2, 3)$ and the hydrodynamic matrix for small Q , $\mathbf{H}(Q)$:

$$\mathbf{H}(Q) = \begin{pmatrix} 0 & if_{un}(Q) & 0 \\ if_{un}(Q) & z_u(Q) & if_{uT}(Q) \\ 0 & if_{uT}(Q) & z_T(Q) \end{pmatrix} \quad (3.14)$$

The matrix elements are the following:

$$\begin{aligned}
f_{un}(Q) &= Qc_s \cdot \sqrt{\gamma} \\
z_u(Q) &= \phi \cdot Q^2 \\
z_T(Q) &= \gamma \cdot D_T Q^2 \\
f_{uT}(Q) &= Qc_s \cdot \sqrt{(\gamma - 1)/\gamma}
\end{aligned} \tag{3.15}$$

Where: $c_s = v_0[\gamma/S(0)]^{1/2}$: adiabatic speed of sound; $\gamma = c_p/c_v$: ratio of specific heat per unit mass at constant pressure and volume; $\phi = [(4/3)\eta + \zeta]/nm$: kinematic longitudinal viscosity, η : shear viscosity, $\rho = nm$: mass density of the fluid with n : number density, ζ : bulk viscosity; $D_T = \lambda/nmc_p$: thermal diffusivity, λ : thermal conductivity.

The three hydrodynamic modes are now given as the three eigenvalues ($O(Q^2)$) of the hydrodynamic matrix:

$$\begin{aligned}
z_u(Q) &= D_T Q^2 && \text{heat mode} \\
z_+(Q) &= \pm ic_s Q + \Gamma_s Q^2 && \text{sound mode}
\end{aligned} \tag{3.16}$$

If the obtained correlation function $G(Q,t)$ is now inversely Fourier-transformed, the solution of (eq. 3.12) in the hydrodynamic form can be written as (eq. 3.17):

$$S(Q, \omega)/S(Q) = 1/\pi \cdot \left\{ A_0 \frac{z_h}{\omega^2 + z_h^2} + A_s \frac{\Gamma_s + b(\omega + \omega_s)}{(\omega + \omega_s)^2 + \Gamma_s^2} + A_s \frac{\Gamma_s - b(\omega - \omega_s)}{(\omega - \omega_s)^2 + \Gamma_s^2} \right\} \tag{3.17}$$

Looking at (eq. 3.17) two cases are of special interest: When $f_{uT} = 0$, the amplitude of the central peak $S(Q, \omega)$ diminishes. Therefore the last two terms representing the side peaks stay and the model remains a damped harmonic oscillation model (DHO). When $z_u(Q) = 0$, one obtains only a Lorentzian with the decay time $z_T(Q)$, the so-called 'viscoelastic model'.

3.3 Neutron Spectroscopy

3.3.1 Three-axis Spectrometry

Among the instrumental methods used for neutron spectroscopy the three-axis technique (developed in 1961 by Brockhouse) plays a significant role, since it allows controlled measurement of the scattering function $S(Q, \omega)$ at essentially any point

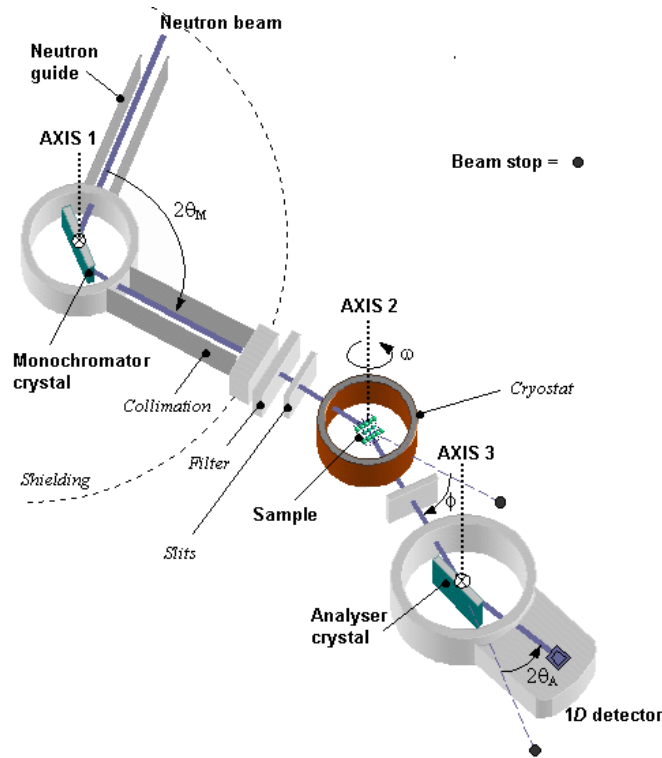


Figure 3.5: In a three-axis spectrometer, the three axes of rotation define the inelastic scattering triangle: The white neutron beam meets the monochromator crystal (axis 1), where a specific wavelength is selected by Bragg reflection. During measurements the sample can be rotated on an independent tray around the angle ω (axis 2). Its change in relative position with respect to the angle ϕ between the incoming beam k_i and the outgoing beam k_f determines the energy or momentum transfer in an inelastic scan. At the analyzer crystal (axis 3) a specific wavelength is again selected by Bragg reflection.

in momentum ($\hbar Q$) and energy ($\hbar\omega$) space. The first three-axis spectrometer was developed in 1961 by Brockhouse at Chalk River, Canada [71].

The instrument's three axes correspond to the axes of rotation of the monochromator, sample and analyzer (Fig. 3.5). While direction and magnitude of the momentum of the incident beam are defined by the monochromator, the analyzer determines direction and magnitude of the final beam. Depending on setup and desired resolution properties (cf. 3.3.3), one chooses a fixed scattering sense geometry for the three axes' (in the direction of the incoming beam, right hand scattering corresponds to a scattering sense of -1).

Apparently, for the measurement of a specific inelastic scan the corresponding scattering triangle must close, which is not always the case. It is not possible to lose more than the incident energy, the maximum momentum transfer is obtained in backscattering geometry for $\phi = 180^\circ$. If the final energy is significantly larger

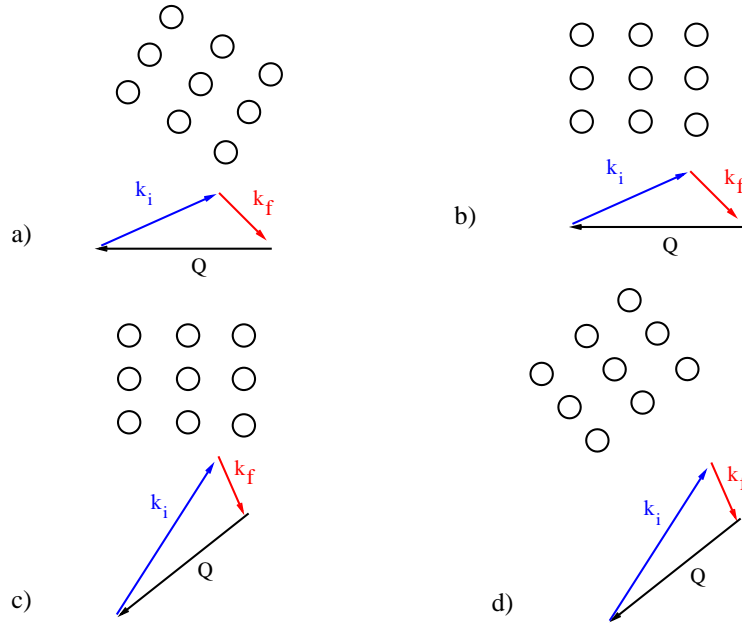


Figure 3.6: Simple energy scan consisting of two data points; point one: a) selection of specific energy and momentum transfer through k_i (monochromator) and k_f (analyzer), b) the sample is turned around the angle ω to adjust its position in \mathbf{Q} with respect to the instrument scattering triangle; point two: c) next energy transfer: k_i changes in direction and magnitude ($2\theta_m$), therefore the angle ϕ between k_i and k_f ($k_f = \text{const.}$) changes as do the directions of k_f and \mathbf{Q} in order to close the scattering triangle, d) sample reference system and instrument are again brought to overlap by turning the sample around the angle ω .

than the incident energy, $E_f \gg E_i$, (eq. 3.1) changes to (eq. 3.18).

$$\mathbf{Q} = -\mathbf{k}_f$$

$$\hbar\omega = -E_f = -\frac{\hbar^2}{2m}Q^2 \quad (3.18)$$

The course of a typical three-axis experiment as the ones reported was as follows: the sample was oriented on the first Bragg peak of the lamellar repeat layers with alternating rocking scans, before taking long reflectivity-scans to characterize the lamellar repeat order of the membrane bilayers. It is then turned to the orthogonal scattering geometry, so that the momentum transfer \mathbf{Q} occurs along the direction of the membrane plane. Two types of inelastic scans are common: constant-energy and constant- Q scans (also referred to as energy scans). The latter are performed by holding either k_i or k_f fixed in magnitude. Fig. 3.6 a)-d) shows how subsequent points of an energy-scan are taken in the constant- k_f mode.

3.3.2 Instrumental Setup

Commonly used monochromators and analyzers consist of pyrolytic graphite (002) crystals, the IN12 monochromator offers a variable vertical curvature for optimum focussing. In the experiments described in this work slits were placed before and after the sample, additional collimation of $30'$ was added before and after the slits, respectively, and $60'$ before the detector. No filter was used, the occurrence of unwanted harmonic wavelengths in k_i and k_f was avoided by limiting the magnitude of the energy transfer with respect to the incident neutron energy to $k_i/k_f < 3/2$.

The standard sample environment consisted of an aluminium chamber, in which the temperature was controlled through a water bath and humidity was held constant using saturated salt solutions. The flux on IN12 usually lies in the order of 10^7 n/cm² s, on IN8 it is a tenfold larger. On IN12, the angular range of $2\theta_m$ lies between 15° and 90° , the angular range of $2\theta_s$ lies between -120° and 120° . On IN8, the corresponding angular range of $2\theta_m$ lies between 10° and 90° , and for $2\theta_s$ between 0° and 130° . Although several multiplex detection systems (e.g. Flatcone, IMPS) were in the construction and testing stages at the ILL at the time of writing, conventional ³He line detectors recorded the scattered signal.

3.3.3 Influence of Instrumental Resolution

The intensity $I(Q_r, \omega)$ measured on a three-axis spectrometer consists of a convolution of the inelastic structure factor $S(Q_r, \omega)$, which characterizes the properties of the sample, with the instrumental resolution function $R(Q_r, \omega)$. We will see in the following, that $R(Q_r, \omega)$ shows significant changes throughout the four-dimensional (\mathbf{Q}, ω) -space probed by the instrument.

As explained in section 3.3.1, two types of inelastic scans are common: constant-energy scans $S(Q_r, \omega = \text{const.})$, and constant-Q scans $S(Q_r = \text{const.}, \omega)$, also referred to as energy-scans. For liquids the peaks corresponding to inelastic excitations are naturally broad and have small amplitudes compared to other contributions to the inelastic signal due to damping (cf. 3.2.3). The choice of the scan-type taken in a specific (Q_r, ω) -regime is one of the features that contribute to a resolution optimized measurement of an excitation. Another is placing the longest axis of the so-called resolution ellipsoid $R(\omega_0 + \Delta\omega, Q_0 + \Delta Q)$ along the gradient of the dispersion surface in the direction of the scan as is shown in Fig. 3.7.

Since the early development of instrumental neutron scattering techniques in the late 1940's, continuous effort has been made to describe the corresponding resolution properties theoretically. For three-circle single-crystal as well as powder

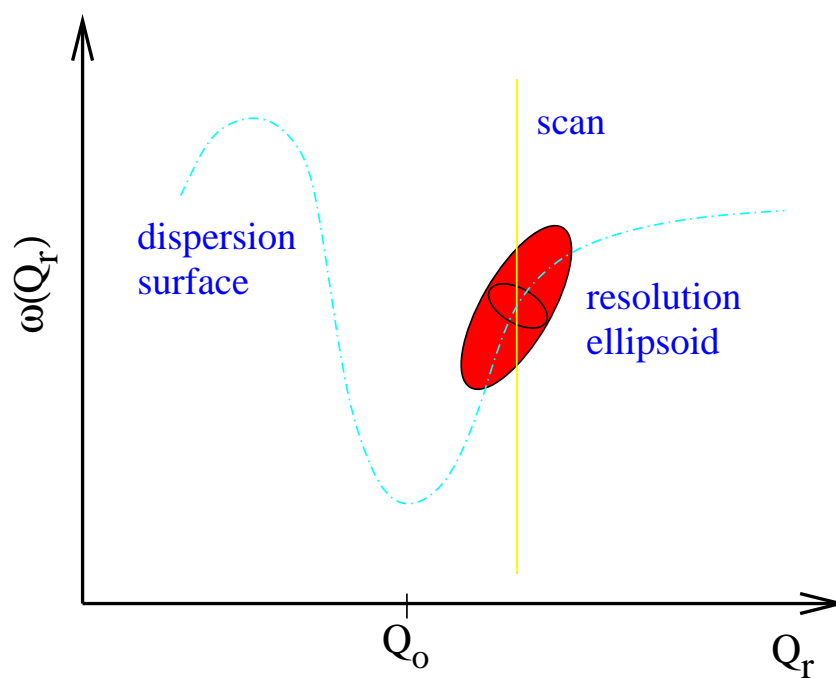


Figure 3.7: Optimum resolution for the measurement of a liquid dispersion (blue curve) is achieved when the longest axis of the resolution ellipsoid is placed along the gradient of the dispersion surface in scan direction. The yellow line indicates an energy scan, which intersects the dispersion surface.

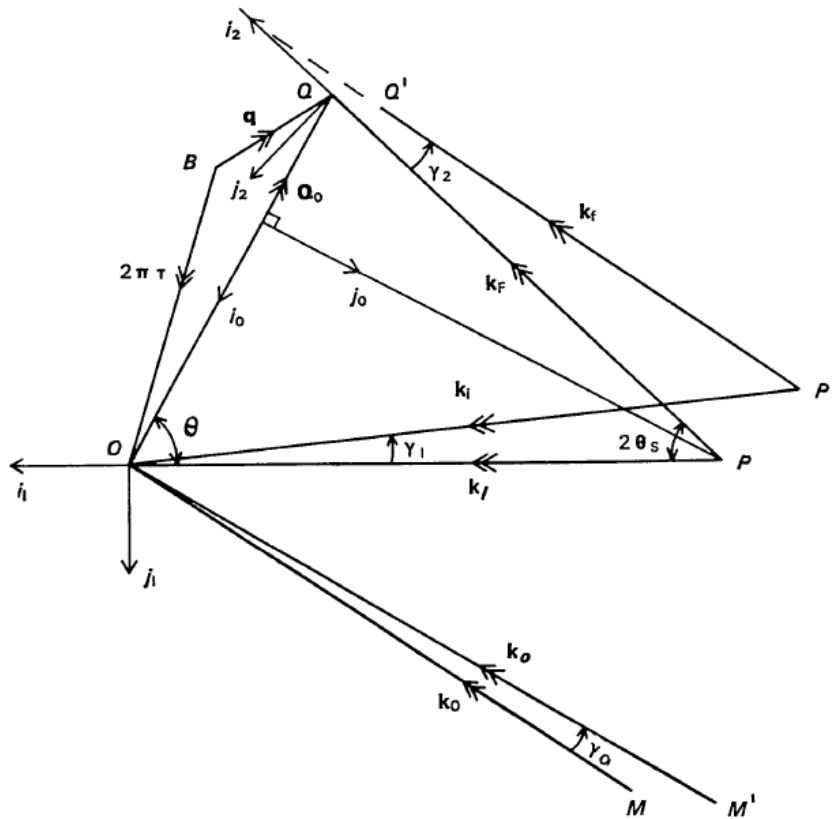


Figure 3.8: Vector diagram showing a general scattering process [93].

diffractometers examples can be found in literature, e. g. [91, 92]. The two most common theoretical approaches for the calculation of the 4-dimensional resolution function $R(\mathbf{Q}, \omega)$ shall be introduced, one by Cooper and Nathans, the other by Popovici. Both types of calculations are implemented in the ILL three-axis matlab data evaluation package 'Rescal' (cf. Appendix), which provides options of scan simulation and data deconvolution.

Cooper and Nathans Cooper and Nathans derive the resolution function for a three-crystal diffractometer by describing experimental arrangements in terms of angular distributions under the assumption of Gaussian mosaic and collimation functions [93].

In order to illustrate how the total probability of reflection can be derived for a neutron, a vector diagram for a general scattering process in reciprocal space is shown in Fig. 3.8: $\mathbf{k}_I(PO)$ is the wave vector of most probable incident neutron from monochromator and \mathbf{k}_i wave vector of any incoming neutron; $\mathbf{k}_F(PQ)$ is the wave vector of the most probable incident neutron after scattering at an angle $2\theta_s$ and an energy transfer for optimum acceptance by the analyzer with \mathbf{k}_f wave vector of the

corresponding neutron. Therefore one can define $\Delta\mathbf{k}_i = \mathbf{k}_i - \mathbf{k}_I$ and $\Delta\mathbf{k}_f = \mathbf{k}_f - \mathbf{k}_F$, as well as the horizontal and vertical divergence angles γ_i and δ_i (for $i = 0, 1, 2, 3$).

The authors express the total probability of reflection of the neutron under the assumption of optimum crystal reflectivities at the monochromator (P_M) and analyzer (P_A), respectively, as well as the corresponding Gaussian mosaic spreads η_M and η_A [93].

In reciprocal space (ω, \mathbf{Q}) , an inelastic scattering process is associated with a neutron's loss/gain of energy for a specific momentum transfer, $\hbar Q$, thereby defining a specific point (ω_0, Q_0) . The resolution function of the instrument is then the probability of detection of the neutron as a function of $\Delta\omega$ and $\Delta\mathbf{Q}$, when the instrument has been set to measure a scattering process corresponding to the point (ω_0, \mathbf{Q}_0) . The value of the resolution function at a given point in (ω, \mathbf{Q}) -space is obtained by integrating the probability over all possible paths $(\mathbf{k}_i, \mathbf{k}_f)$ to that point:

$$R(\omega, \mathbf{Q}) = \int P(\omega, \mathbf{Q}) d\mathbf{k}_i d\mathbf{k}_f \quad (3.19)$$

After transforming the integration variables into (ω, \mathbf{Q}) -space the resolution function can be expressed in the form of a 4-dimensional ellipsoidal [93]:

$$R(\omega_0 + \Delta\omega, \mathbf{Q}_0 + \Delta\mathbf{Q}) = R_0 \cdot \exp\left\{-\frac{1}{2} \underbrace{\sum_{k=1}^4 \sum_{l=1}^4 M_{kl} X_k X_l}_{:=p}\right\} \quad (3.20)$$

In this equation (eq. 3.20) the variables are denoted as follows: $X_1 = \Delta Q_x$, $X_2 = \Delta Q_y$, $X_3 = \Delta Q_z$, $X_4 = \Delta\omega$ and $R_0 = R(\omega_0, Q_0)$ is the optimum value of the resolution function. R_0 and M_{kl} are involved functions of k_I , ω_0 and Q_0 , as well as the intrinsic properties of the collimators, the monochromator and analyzer. A convenient visualization of the resolution function is an ellipsoid with a specifically defined constant probability p , for which the resolution equals exactly 50% of R_0 .

The intensity observed in an experiment can now be expressed for a given scattering cross section σ :

$$I(\omega_0, \mathbf{Q}_0) = \int R(\omega_0 + \Delta\omega, \mathbf{Q}_0 + \Delta\mathbf{Q}) \cdot \sigma(\omega_0 + \Delta\omega, \mathbf{Q}_0 + \Delta\mathbf{Q}) \Delta\mathbf{Q} \Delta\omega \quad (3.21)$$

Up to this point, we have focussed on the resolution function in relation to the energy lost by the neutron as a function of momentum transfer \mathbf{Q} , namely the scattering cross section as the dispersion surface $\omega(\mathbf{q})$ and the momentum of the created phonon $-\hbar\mathbf{q}$ (\mathbf{q} denotes a vector in \mathbf{Q} -space from the Bragg point of

interest). It is convention to plot $\omega(\mathbf{q})$ positive for phonon creation (energy loss) and negative for phonon annihilation (energy gain).

Germanium crystals are commonly used as a reference system to compare with instrumental resolution, since its dispersive behavior has been well established in the past 50 years, e. g. [94, 95]. This is the case for two reasons: On the one hand the crystal has a simple well-known lattice structure. On the other hand it consists of two atoms per unit cell and therefore exhibits optical as well as acoustic vibrations.

It can be shown that the experimental resolution function obtained from measurements with a perfect single-crystal of germanium has the form predicted by the analytic expression [93]. Therefore a direct comparison with the instrumental parameters is possible as well as a theoretical derivation of the resolution function at any point in (ω, \mathbf{Q}) -space.

The most common type of focussing is the so-called 'gradient focussing' which is applied when the orientation of the ellipsoid is given in a manner that the longest principal axis is aligned in the dispersion surface. The asymmetry of the cuts through the ellipsoid evokes pronounced focussing or defocussing effects. A focussing position for energy loss corresponds to a defocussing position for energy gain and vice versa.

Optimum resolved scans are therefore obtained on the one hand through selection of defined points in reciprocal space where a specific phonon can be measured, on the other hand through the choice of the instrumental parameters, such as for example the material of monochromator (d_M) and analyzer (d_A) or the scattering sense configuration.

Popovici Popovici formulates the resolution function for a three-axis spectrometer, not only taking into account the angular transmission function described above, but also the spatial configuration of the experimental set-up and the curvature of the monochromator and analyzer crystals [96]. Instead of the angular variables used before, now the initial variables are the coordinates \mathbf{r}_i of the points where the neutrons are emitted from the source (\mathbf{r}_0), reflected in the monochromator (\mathbf{r}_1), scattered in the sample (\mathbf{r}_2), reflected again in the analyzer (\mathbf{r}_3) and finally detected (\mathbf{r}_4) (see Fig. 3.9). The axes y_1 , x_2 and y_3 are directed along the bisectors of the corresponding scattering angles $2\theta_i$, the distances between the origins of the corresponding reference systems are denoted by L_i ($i = 0, 1, 2, 3$).

The shape of the crystals and the sample is described by probability distributions $p_i(\mathbf{r}_i)$ in the normal approximation. Popovici shows that, when spatial effects are included, the covariance matrix of the probability distribution changes significantly

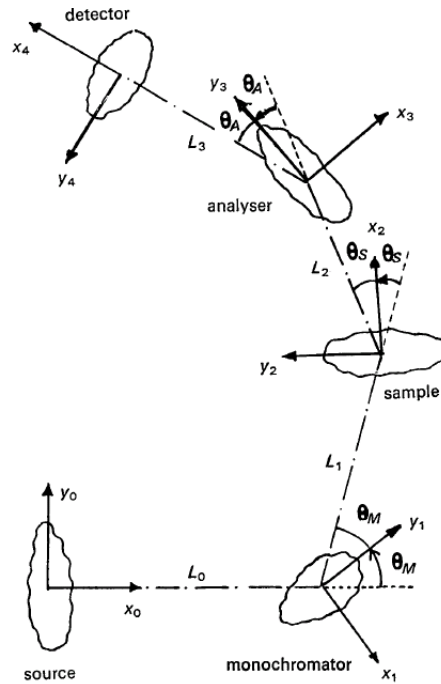


Figure 3.9: Geometry of a neutron scattering experiment with the coordinate systems used in computations indicated. All scattering angles are shown in the positive sense [96].

in comparison to the previously introduced formalism by Cooper and Nathans: the finite sample dimensions introduce a coupling between the monochromator and the analyzer units which is stronger the smaller their mosaic spread [96]. Except for very small samples it is no longer possible to express $P(\mathbf{k}_i, \mathbf{k}_f)$ as a product of two independent transmission functions. The new expression derived for the resolution matrix takes into account the absolute intensity dependence on the distances L_i , the dimensions and shape of the crystals and sample as well as the exposed areas of the neutron source and detector and the divergence of the Soller collimators if included.

3.3.4 Data Treatment of Inelastic Energy-Scans

Absorption Correction: In all of the presented experiments inelastic energy scans were performed in constant k_f mode. The non-cylindrical geometry of the sample used causes absorption that needs to be corrected for scans with $\Delta\omega \neq 0$. Only for elastic scans with $\Delta\omega = 0$ it is positioned in the geometrical middle of the angle between k_i and k_f (Fig. 3.10, a)). For inelastic scans, however, it continuously changes position with respect to k_i and k_f (Fig. 3.10, b) and c)), which has to be taken into account in order to obtain intensity balanced of data.

The absorption α can be described through an analytic expression as a superposition of the absorption occurring with respect to k_i (dominant for $\Delta\omega < 0$) and the

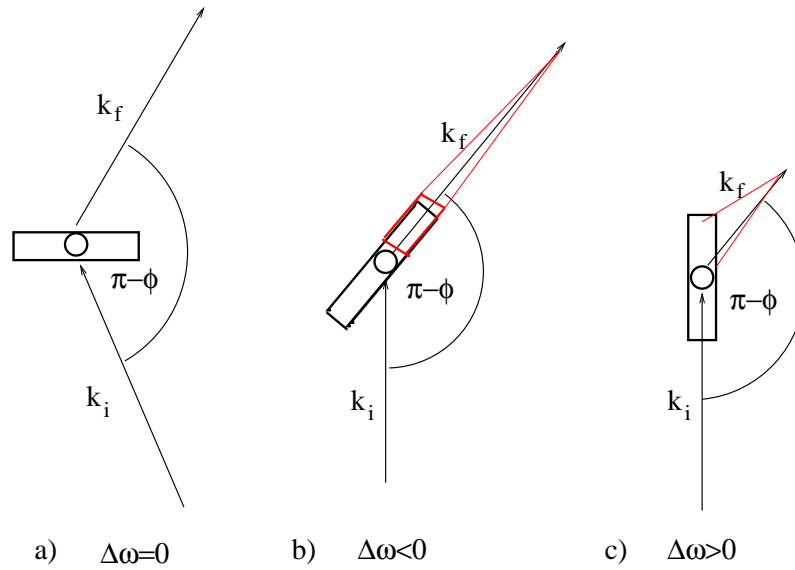


Figure 3.10: Total absorption of incoming (k_i) and final beam (k_f) due to sample geometry changes throughout inelastic energy-scan : a) symmetric absorption is obtained around the elastic line; b) maximum absorption in k_f occurs when the long axis of the sample is directed parallel to the final beam; c) overall maximum absorption occurs when the long sample axis lies parallel to the incoming beam k_i .

absorption occurring with respect to k_f (dominant for $\Delta\omega > 0$).

The expression used for the implementation of the absorption correction is:

$$\alpha = 2 \cdot \sqrt{\left(1 + \left(\frac{5}{2}\right)^2\right) \cdot \left(\sin^2\left(\frac{\pi}{2} - \omega\right) + \cos^2(\pi - \phi - \omega)\right)} \quad (3.22)$$

The factor ' $\frac{5}{2}$ ' stems from sample geometry itself, ϕ is the angle between k_i and k_f and ω is the angle at which the sample has to be turned in order to close the scattering triangle.

Detailed Balance Correction: The inelastic scattering function $S(\mathbf{Q}, \omega)$ is a direct representation of fluctuations in the sample depending on the corresponding momentum and frequency. Before further treatment of the data obtained through fits of energy-symmetric functions it is important to take into account the principle of 'detailed balance': $S(-\mathbf{Q}, -\omega) = e^{-\hbar\omega/k_B T} \cdot S(\mathbf{Q}, \omega)$. The correction is based on the idea that the probability of a transition in the sample depends on the statistical weight factor for the initial state. This population of states is by nature lower for excitation annihilation than for excitation creation of a phonon (Fig. 3.11).

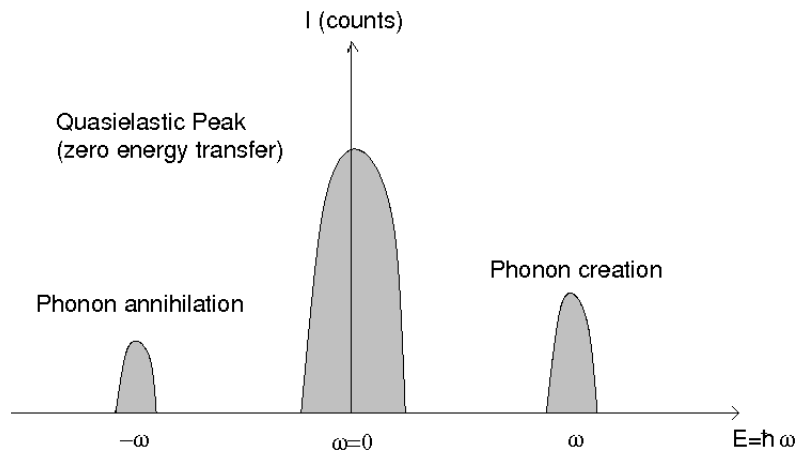


Figure 3.11: The phonon creation state is by definition more populated than the phonon annihilation state. The 'detailed balance'-correction performed on the inelastic energy-scans takes into account that a stronger signal is obtained for positive energy transfers on the phonon creation side, than for negative energy transfers on the phonon annihilation side.

Chapter 4

Single Component Model Membrane: DSPC-d70

The collective in-plane density fluctuations of a model membrane such as DSPC-d70 in comparison with the previously studied DMPC-d54 [8, 97] are interesting for different reasons: A possible connection between the 'critical swelling' that accompanies the main phase transition in several phospholipids such as DMPC, but not DSPC, [25, 26], and the observation of a typical liquid dispersion curve is investigated. Differences in the bilayer ordering and corresponding in-plane packing of the lipid molecules are observed by x-ray and complementary neutron diffraction and give an indication for the changes in the in-plane density distribution of the lipid acyl chains. These can be linked to possible variations in the modulation of propagating sonic waves, which are the origin of the collective in-plane density fluctuations.

4.1 X-ray Diffraction: Structural Phase Characterization

For extensive structural characterization of model membrane systems prior to an inelastic neutron scattering experiment the IRP inhouse diffractometers are well suited, complementing the diffraction results obtained from a neutron three-axis spectrometer. For the x-ray experiments solutions of multilamellar vesicles (MLV's) were chosen as samples. Since the oriented multilayer samples used in the neutron experiments are immersed in heavy water vapor and their lamellar repeat spacing D_z depends on humidity [98], reference values for full hydration of the derived structural quantities were obtained from x-ray diffraction.

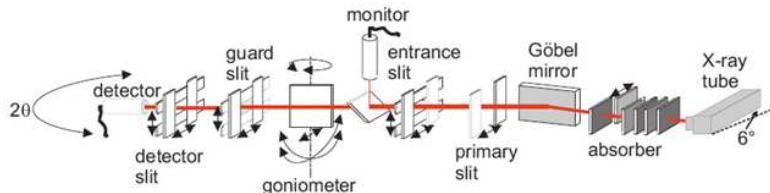


Figure 4.1: Schematic of the IRP in-house diffractometer (WENDI) at a sealed tube x-ray source.

4.1.1 Experimental

Samples: The phospholipids DMPC and DSPC were purchased from Avanti (Alabaster, AL) and dissolved in a (1:1) mixture of TFE/Chloroform. The solvent was subsequently evaporated in a vacuum oven for two days. The dried lipids were then hydrated with Millipore water at a concentration of 200 mg/ml, heated from room temperature up to 60°C, ultrasonicated in a bath and cooled down to room temperature again three times subsequently. The suspension was then kept at a constant temperature of 36°C and 60°C, respectively, over night to allow the formation of multilamellar vesicles (MLV's).

The x-ray absorption in water as a function of the diameter of the sample capillaries was calculated according to $I_x = I_0 \cdot \exp -(\frac{\mu}{\rho})\rho \cdot x$. Taking into account the material specific absorption factor μ/ρ and the given intensities we chose to use Quarz-capillaries of 1.5 mm diameter that were sealed air tight.

The in-house sealed tube diffractometer setup (WENDI): The instrument (Fig. 4.1) consists of a sealed tube source (Cu: k_α , $12 \cdot 0.4 \text{ mm}^2$ line focus), bent collimating Göbel multilayer mirrors, motorized slits, automatic attenuators and a fast NaI scintillation counter (Cyberstar, Oxford Instruments, Abingdon). Scans are run by the scientific software package Spec (Certified Scientific Software, Cambridge, MA).

Typical scans obtained from solutions of multilamellar vesicles are shown in Fig. 4.2: at low angles, that is small Q-values, the bilayers' repeat-spacing was derived from the 'Bragg'-condition. At high angles, thus large Q-values the acyl-chain correlation was observed. The temperature dependent x-ray diffraction measurements consisted of small-angle scans (SAXS) in the range of $Q_z=0.05$ to $Q_z=0.13 \text{ \AA}^{-1}$ counting 80 points for 10 sec and wide-angle scans (WAXS) in the range of $Q_r=1.0$ to $Q_r=1.8 \text{ \AA}^{-1}$ counting 100 points for 120 sec. Additional small-angle scans ranging from $Q_z=0.05$ to $Q_z=0.5 \text{ \AA}^{-1}$ were taken counting 100 points for 500 sec in order to compare the results. For SAXS scans the slits were set to $s1 = 0.1 \text{ mm}$, $s2 = 0.4 \text{ mm}$

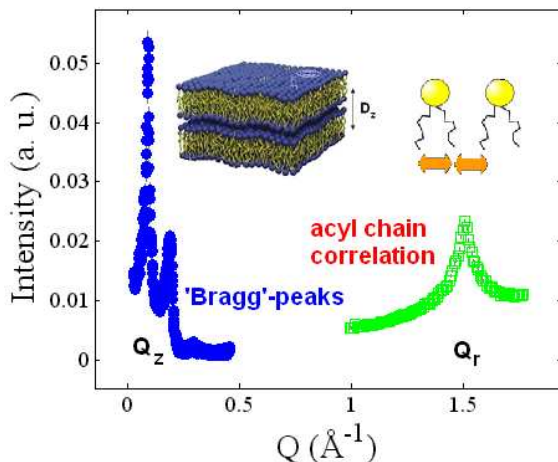


Figure 4.2: Typical SAXS- and WAXS-scans taken on WENDI for solutions of multilamellar DMPC-vesicles (MLV's); low Q -range: quasi- Bragg peaks $S(Q_z)$ yielding the bilayer repeat-spacing D_z ; high Q -range: the acyl-chain correlation peak $S(Q_r)$ corresponds to the in-plane aggregation of (lipid) molecules.

and $s_3 = 0.2$ mm, for WAXS scans to $s_1 = 0.5$ mm, $s_2 = 0.5$ mm and $s_3 = 1$ mm. Representative macros for both types of measurements are given in Appendix A.1.1 and A.1.2.

The sample-holder containing the different capillaries was inserted into a temperature chamber made of aluminum with capton windows. The accuracy in the external temperature control with this chamber was better than $\pm 0.5^\circ\text{C}$ (Pt 100 temperature sensor fastened 5 cm above sample). It was operated by a standard thermostatic bath (Julabo F25), which was also steered by the diffractometer control software spec.

4.1.2 Effect of Lipid Chain Length: Bilayer and In-plane Ordering

To distinguish between the temperature-dependent structural properties of the two single lipid model membranes DMPC and DSPC, all characteristic scans are first discussed for the short chain lipid DMPC, then compared to corresponding results for the long chain lipid DSPC.

The temperature-dependent changes in the lamellar repeat distance were obtained from the peak positions ($D_z = 2\pi/Q_z$) of the measured SAXS-scans through a matlab function that determines maximum coordinates (cf. Appendix A.2.2, A.2.3). The bilayer spacing D_z is plotted as a function of the effective temperature difference from the respective main phase transition temperature T_m . The data is shown in 3-d intensity plots of the first order 'Bragg' peak $S(Q_z)$ for DMPC (Fig. 4.3) and

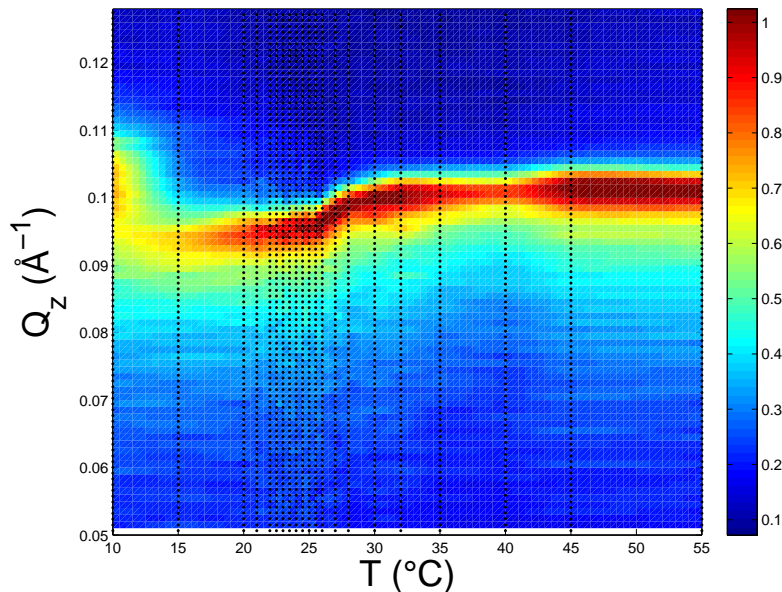


Figure 4.3: Change in Q_z around first DMPC SAXS peak from 10° to 55°C. Black dotted lines indicate the single scans in between which the intensity (normalized to maximum peak) is interpolated. Note, that the main phase transition was anticipated at a lower temperature (cf. text).

for DSPC (Fig. 4.4). The logarithmic intensity scaling is interpolated between scans at different temperatures (dotted lines).

The data for DMPC show two phase transitions (Fig. 4.3): at 12°C the membrane undergoes the 'pretransition' from the gel ($L_{\beta'}$) to the ripple ($P_{\beta'}$) phase (cf. 2.2.1). The associated peak shift towards lower Q_z corresponds to an increase in the lamellar D_z -spacing (Fig. 4.5) as vertical ripples along the bilayer normal are induced. Another shift in the peak position is observed towards larger Q_z at 25°C (Fig. 4.3). The literature value for the main phase transition lies at $T_m = 24.3^\circ\text{C}$. The deviation slightly exceeds the accuracy of the chamber regulation due to a systematic error in the calibration of the PT 100 temperature sensor in the sample chamber. The decrease in the D_z -spacing with rising temperature is related to the reduction of the lipid's effective acyl chain length due to the formation of multiple *gauche* isomers (cf. 2.2.2).

The corresponding temperature-dependent plot for DSPC exhibits only a slight shift around the main phase transition temperature observed at 56.5°C (literature value: $T_m = 55^\circ\text{C}$, [15]). The pretransition is not observed for DSPC within the available Q_z -resolution (literature: 51°C [15]). The derived temperature-dependent D_z -spacings for DMPC agree well with literature values [23, 25, 26], a systematic

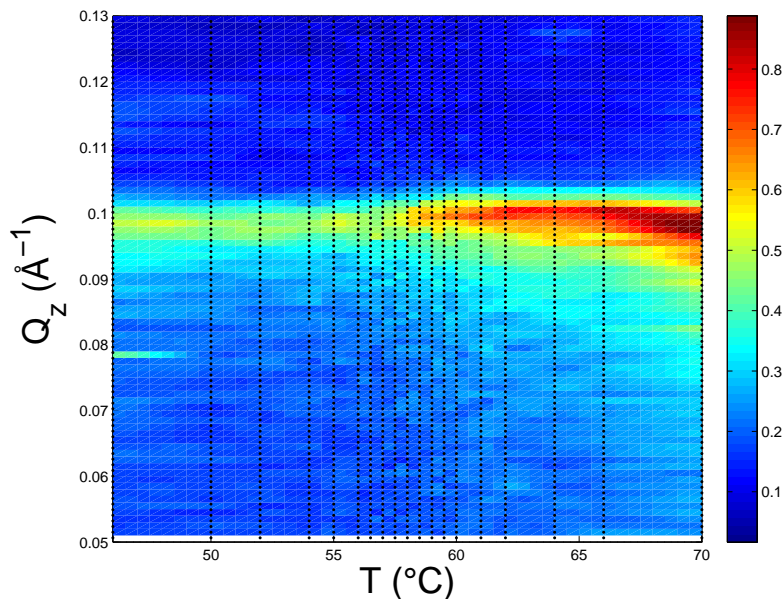


Figure 4.4: Change in Q_z around first DSPC SAXS peak from 45° to 70°C. Black dotted lines indicate the single scans, in between which the intensity (normalized to maximum peak).

shift towards lower D_z -spacings can be linked to the asymmetry in the peak broadening observed at temperatures above the main phase transition.

The temperature-dependent DMPC acyl chain correlation peak $S(Q_r)$ shows a distinct shift around the main phase transition at 25°C (Fig. 4.6). The peaks were fitted by Lorentzians after taking into account an underlying intensity contribution of the water peak at 2.0 \AA^{-1} by subtracting a linear background. Examples for temperatures well within the gel phase (20°C), around the main phase transition (25°C) and well within the fluid phase (30°C) are plotted (Fig. 4.7, *left*). The overall fit results corresponding to the data shown in Fig. 4.6 are plotted in Fig. 4.7 (*right*). When the sample is heated from the gel to the fluid phase, the peak position shifts to smaller Q_r -values (larger average nearest neighbor distances) and its width increases, corresponding to a less ordered packing of the lipid acyl chains. The latter is quantified in Fig. 4.7 (*right*) in terms of the correlation length $\xi_r = 1/\text{HWHM}$ (HWHM: Lorentzian half width at half maximum). Within the experimental errors discussed, the results match the ones obtained from previous neutron experiments on oriented samples [8].

The temperature-dependent changes of the DMPC (short chain) and DSPC (long chain) acyl chain correlation peaks exhibit striking differences: a clear phase coexistence over a temperature range of several degrees is observed for DSPC (Fig. 4.8),

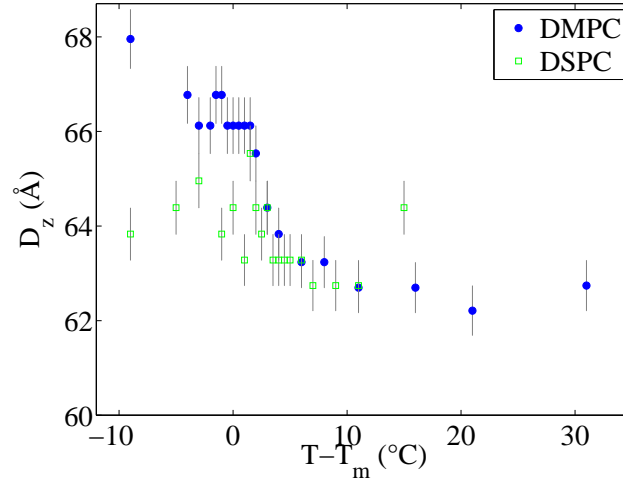


Figure 4.5: Comparison of the temperature-dependence of the lamellar repeat spacings D_z for DMPC and DSPC, derived from respective peak positions in SAXS-scans (cf. Fig. 4.3, 4.4). The error bars result from the accuracy of single scans in the temperature ramps (cf. Appendix A.2.3: exemplary scans, data treatment).

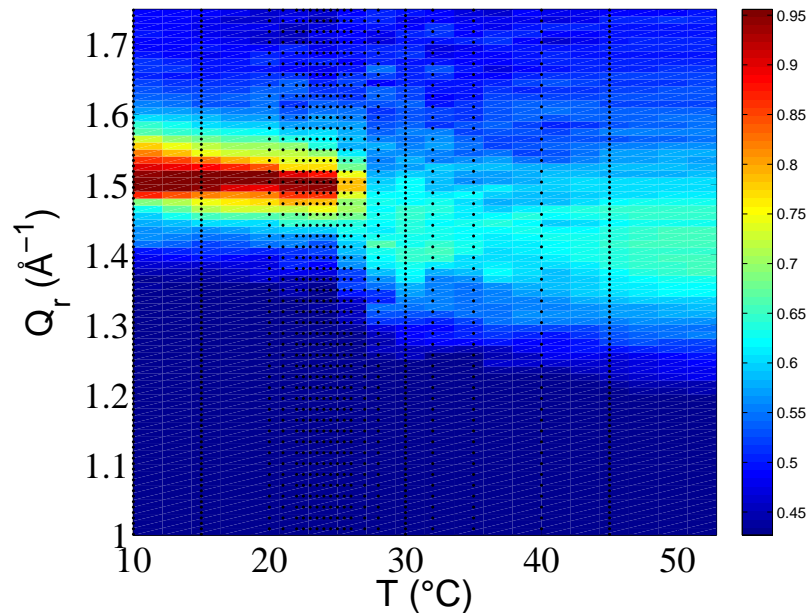


Figure 4.6: Change in Q_r around the DMPC acyl chain correlation peak $S(Q_r)$ from 10° to 55°C observed by x-ray diffraction. Black dotted lines indicate points of the single scans, in between which the intensity (normalized to maximum peak) is interpolated. Cf. Fig. 4.7 for corresponding fits.

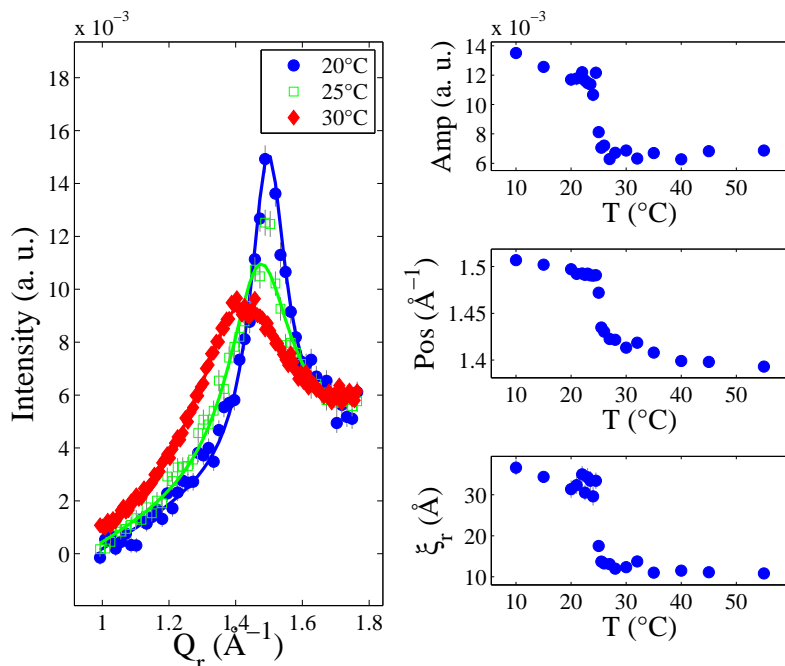


Figure 4.7: DMPC elastic structure factor $S(Q_r)$ obtained by x-ray diffraction: (left) Lorentzian fits of the interchain correlation peak at temperatures 20°, 25°, and 30°C; (right) peak intensity, position and correlation length for all measured temperatures T .

that does not occur for DMPC.

Corresponding fits consist of two separate Lorentzians and are shown in Fig. 4.9. Therefore the existence of two different correlation lengths characteristic for each of the respective phases has to be assumed for DSPC. The broader peak corresponding to a weaker correlation of less organized chains appears over nearly the entire temperature range (Fig. 4.8). The difference in the peak widths corresponding to the respective lipid's gel and fluid phase is much more pronounced for DSPC than for DMPC. This point will be discussed in more detail later on along with the corresponding neutron diffraction results obtained for DSPC-d70.

In summary, the investigation of temperature-dependent structural changes of the two single component model membranes show pronounced differences in their respective in-plane and bilayer arrangement of lipid molecules upon undergoing the main phase transition. Moreover, the acyl chain correlation peak for the lipid with the longer chain length, DSPC, exhibits a phase coexistence that is not observed for DMPC. In the following section the implications of the distinct chain correlation of each of the two lipids on the collective in-plane dynamics are discussed.

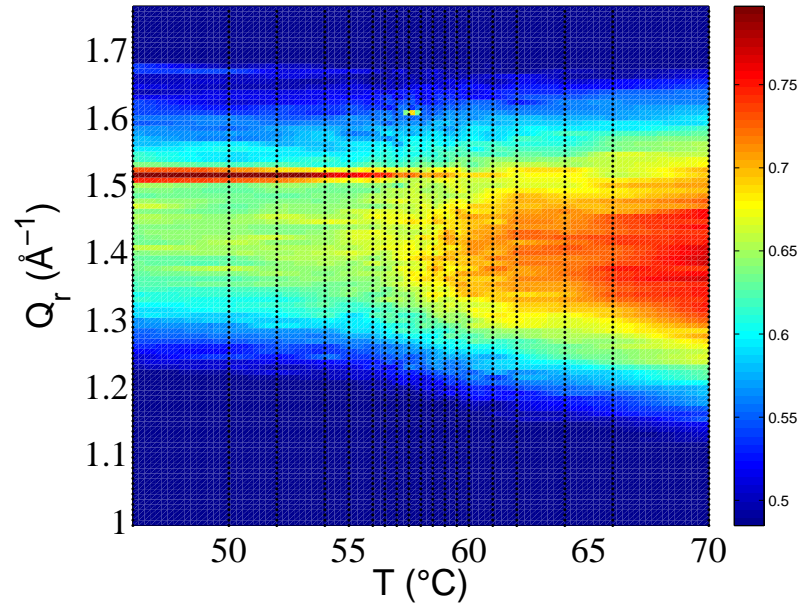


Figure 4.8: Change in Q_r around the DSPC acyl chain correlation peak $S(Q_r)$ from 45° to 70°C. Black dotted lines indicate single scans, in between which the intensity (normalized with respect to maximum peak) is interpolated. Corresponding fits are shown in Fig. 4.9. Between 56° and 59°C a coexistence of the lipid's gel and fluid phase is indicated by the superposition of two acyl chain correlation peaks.

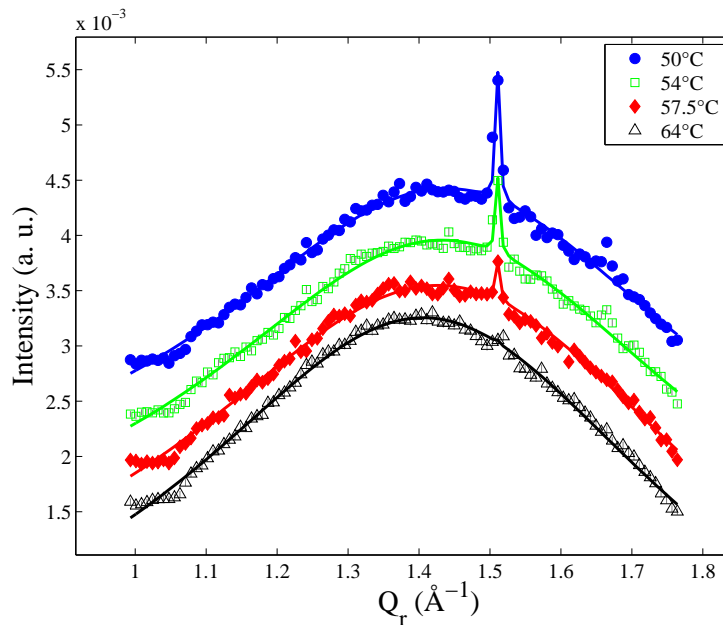


Figure 4.9: DSPC elastic structure factor $S(Q_r)$ obtained by x-ray diffraction: a peak coexistence in the acyl chain correlation is visible over a broad range of temperatures (fit: two Lorentzians). The main phase transition temperature lies at $T_m = 55^\circ\text{C}$. Cf. Fig. 4.8.



Figure 4.10: Photo of a typical 'sandwich sample': 20 silicon wafers, each supporting several hundreds of highly oriented phospholipid bilayers are placed on top of each other in an aluminum frame, separated by a pair of aluminum spacers. This allows the D_2O -vapor to flow between single wafers.

4.2 Neutron Scattering: Structure and Collective Dynamics

To obtain specific points of the DSPC-d70 dispersion curve in its respective gel and fluid phases, an inelastic neutron scattering experiment was performed on the V2-Flex three-axis spectrometer at the HMI, Berlin. Reflectivity scans $S(Q_z)$ were taken and the temperature-dependent in-plane static structure factor $S(Q_r)$ was carefully investigated in order to compare to the x-ray diffraction results presented in section 4.1. The structural results for the two model membranes, which vary in the respective lipid chain length (cf. 2.3.1), indicate significant differences in the size of domains of lipids in the gel and in the fluid phase which are formed around the main phase transition temperature. These characteristic domains are assumed to influence the corresponding collective in-plane fluctuations.

4.2.1 Sample Preparation and Experiment

The sample was prepared from 400 mg DSPC-d70 (partially deuterated in the acyl chains to enhance coherent scattering), ordered at Avanti Polar Lipids. The phospholipid powder was dissolved in a mixture of TFE/Chloroform (1:1) at a concentration of 20 mg/ml. In order to yield an oriented sample the solution was spread onto 20 silicon wafers, with each wafer holding several hundred aligned multilayer membrane stacks. After letting the solvent evaporate for 1-2 hours, the wafers were put into a vacuum oven over night, before being arranged on top of each other into a 'sandwich' sample (see Fig. 4.10).

The sample environment consisted of an aluminum chamber in which the tem-

perature was regulated by a standard water bath and the humidity with a potassium nitrate salt solution ($\approx 85\%$ RH at 50°C [99]; the literature value for lamellar spacing in DSPC MLV's at full hydration lies at $D_z=69 \text{ \AA}$ [26]). Aluminium and silicon are highly transparent for neutrons. In order to achieve the desired scattering contrast and minimize unwanted incoherent scattering by water molecules, heavy water vapor was used inside the chamber. Because of a high gradient towards room temperature (measurements were taken between 50°C in the gel and 65°C in the fluid phase) an additional tent made of aluminum foil (air in between chamber and foil) was added. The Haake bath was programmed and controlled by a separate computer. By monitoring the lamellar spacing derived from the first Bragg peak of reflectivity curves, the maximum humidity was achieved ($D_z = 60.24(1) \text{ \AA}$).

The course of such a three-axis experiment with the aim of combined elastic and inelastic measurements is as follows: The sample is alternately aligned on the first Bragg peak of the lamellar repeat spacing with subsequent rocking scans. Long reflectivity curves $S(Q_z)$ are taken in order to characterize the sample in terms of humidity and bilayer ordering. In a next step, the scattering geometry is changed into the 'in-plane'-configuration by turning the sample around an angle of 90° . The scattering vector \mathbf{Q} now lies within the plane of the membrane, allowing the measurement of the static structure factor $S(Q_r)$, the acyl chain correlation peak. Inelastic measurements consist either of constant-energy or constant- Q_r scans and are on a cold three-axis spectrometer usually taken at constant $k_f = 1.5 \text{ \AA}^{-1}$.

All inelastic scans were simulated on the respective instrument computer before running under the scientific ILL software package MAD. Prior to actual measurements, various properties of instrumental resolution are taken into account using the ILL matlab software package 'Rescal' which implements resolution calculation according to Cooper and Nathans as well as Popovici (cf. 3.3.3, Appendix B.5). The experiment was performed under the proposal PHY-02-0531 at HMI: *Role of collective fluctuations in model membranes with respect to two competing theoretical scenarios for the main phase transition*. We chose to measure the dispersion relation on the three-axis spectrometer V2-FLEX, because of its extremely low instrumental background. However, an additional background evoked by scattering contributions of the aluminium sample environment was encountered with unexpected intensity.

4.2.2 Diffraction: Bilayer Repeat Spacing and Chain Correlation

To complement the information on the lamellar bilayer repeat ordering gained by x-ray scattering, characteristic reflectivity scans were taken well within the gel and

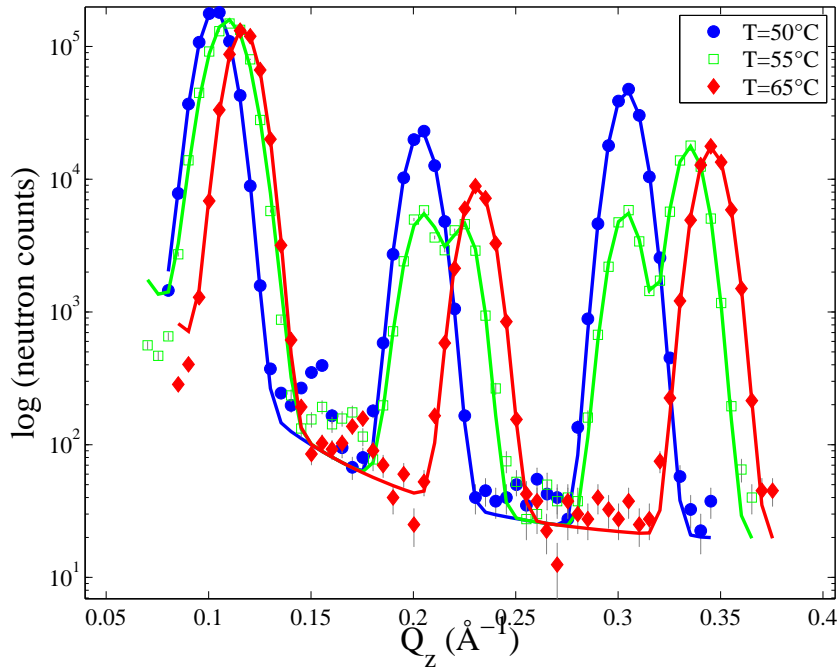


Figure 4.11: DSPC-d70 reflectivity-scans: taken in gel-phase (blue), fluid phase (red) and at main phase transition (green). The respective fits (solid lines) consist of multiple Gaussians with a Q_z^{-4} -background. A coexistence of the lipid gel and fluid phase around 55°C is visible in the peak splitting.

the fluid phase, as well as at the main phase transition temperature (Fig. 4.11).

The peaks were fitted by multiple Gaussians taking into account a Q^{-4} -decrease as background that is due to the reflectivity contribution of the silicon wafer. The curves reflect the decrease of the bilayer thickness D_z with rising temperature due to the effective shortening of the acyl chains with increasing kink formation (cf. Table 4.1). The peak splitting observed for DSPC-d70 near the main phase transition, where domains of both gel and fluid phases are largest, points towards a phase coexistence that could not be seen in analogous scans taken on DMPC-d54. This could be explained by the formation of significantly larger domains for DSPC-d70 which allow separate probing of a bilayer spacing for each specific phase.

In the corresponding temperature-dependent SAXS scans on unoriented DSPC samples (MLV's), on the other hand, a peak splitting was not observed, but a notable peak broadening upon changing into the lipid's fluid phase (Fig. 4.4).

Investigation of the temperature-dependent elastic structure factor $S(Q_r)$ for both phospholipids shows a significant difference in the in-plane correlation of the lipid acyl chains. For DMPC, which consists of 14 acyl segments in the lipid chains, a continuous shift in the position of the acyl chain correlation peak $S(Q_r)$ was observed

T (°C)	phase	D_z -spacing (Å)
50	gel	61.6(82)
55	gel	60.2(73)
55	fluid	56.5(70)
65	fluid	54.2(73)

Table 4.1: Lamellar repeat spacings D_z obtained from fit of DSPC-d70 reflectivity curves in Fig. 4.11.

by x-ray (section 4.1.2) and neutron diffraction [8] while undergoing the lipids main phase transition temperature.

The x-ray diffraction results for DSPC exhibit a coexistence of two chain correlation peaks linked to the lipid’s gel and fluid phase, respectively, over a temperature range of several degrees (Fig. 4.8). Neutron diffraction measurements of the elastic in-plane structure factor $S(Q_r)$ also show a coexistence of distinctly separate chain correlation peaks. However, this coexistence is visible mainly around the main phase transition temperature $T_m = 55^\circ\text{C}$ (Fig. 4.13).

The temperature-dependent acyl chain correlation peak probed by x-ray diffraction on DSPC shows a strong fluid-phase chain correlation peak (Fig. 4.9). Fits of the neutron diffraction results on the same model system (Fig. 4.12, (*left*)) exhibit a comparably more pronounced contribution of the lipid’s gel-phase chain correlation peak (Fig. 4.13). Parameters of the Lorentzian fit of this particular peak are shown in Fig. 4.12 on the right, parameters corresponding to the specific peaks shown in Fig. 4.12, (*left*) are given in Table 4.2. The difference in the respective peak positions and widths is attributed to the varying hydration conditions and has already been qualitatively observed for other model membranes [100] and quantitatively described for DMPC [98].

The humidity was controlled through different saturated salt solutions, which means that different levels of hydration have to be taken into account for the two lipids: near its main phase transition DMPC-d54 was measured at $\approx 95\%RH$ (at 20°C), DSPC-d70 on the other hand at $\approx 85\%RH$ [99]. The corresponding x-ray diffraction results for the temperature dependence of the acyl chain correlation peak of the two model systems, on the other hand, were obtained from fully hydrated samples (MLV’s) and show a qualitative agreement with the neutron diffraction results.

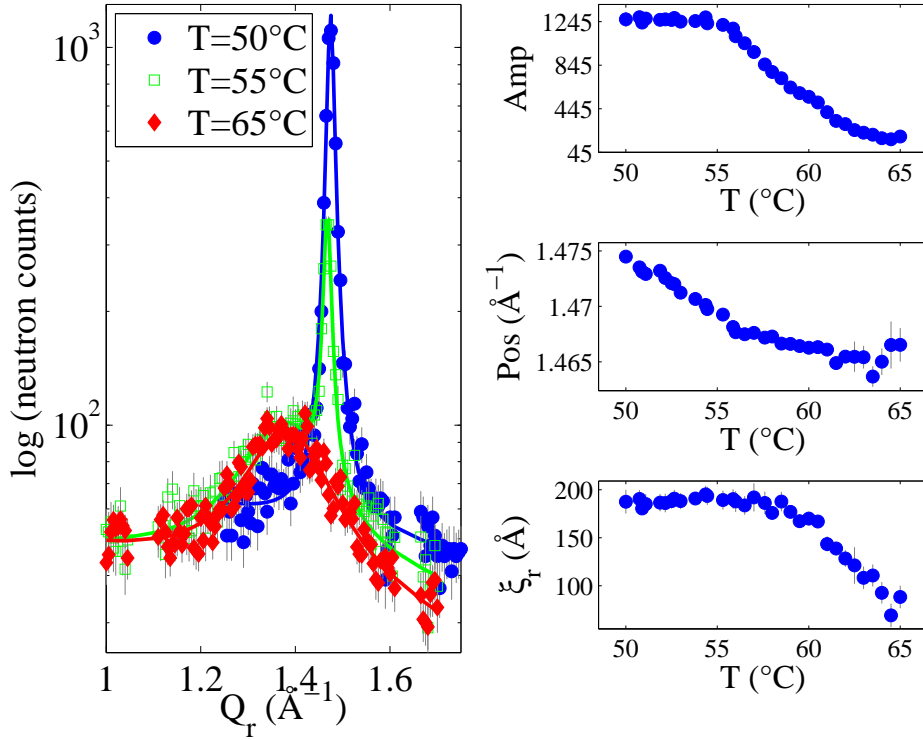


Figure 4.12: (*left*) DSPC-d70 elastic structure factor $S(Q_r)$ measured with the cold three-axis spectrometer V2-Flex (HMI, Berlin) at temperatures 50° (gel phase), 55° (gel/fluid phase), and 65°C (fluid phase): a phase coexistence around the main phase transition at 55°C is clearly visible, which was fitted by two Lorentzians, each of which correspond to a distinct phase (Table 4.2). (*right*) Peak intensity, position and correlation length of the narrow peak for the lipid's gel phase as fitted for all measured temperatures. Cf. Fig. 4.7 for corresponding DMPC chain peak obtained by x-ray diffraction.

peak	T (°C)	amp (n. c.)	pos (Å ⁻¹)	ξ_r (Å)
gel	50	1169(36)	1.4747(2)	234.6(72)
gel	55	299(15)	1.4679(4)	230(158)
fluid	55	60.1(28)	1.3728(54)	19.0(18)
fluid	65	62.5(20)	1.3833(31)	19.0(12)

Table 4.2: Parameters of the Lorentzian fits of the DSPC-d70 elastic structure factor $S(Q_r)$ shown in Fig. 4.12 (*left*), the correlation length is determined according to $\xi_r = 1/\text{HWHM}$.

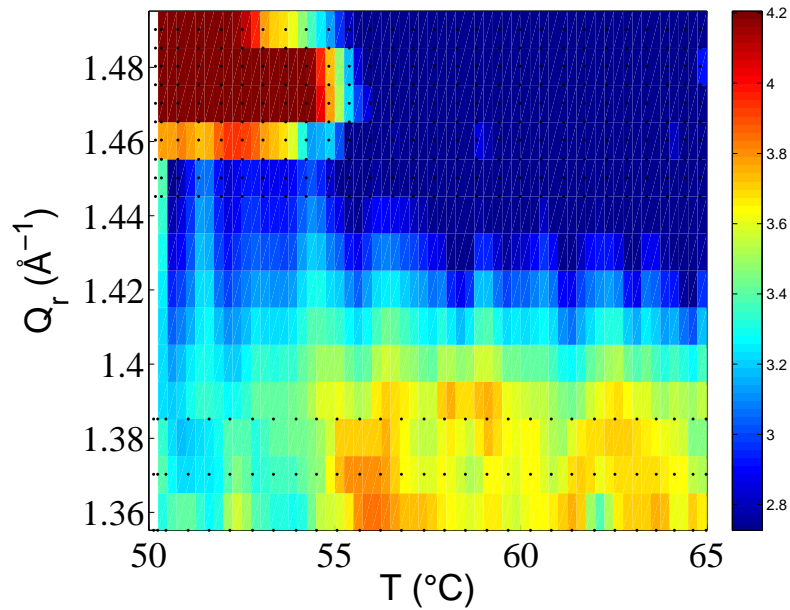


Figure 4.13: Change in Q_r around the DSPC-d70 acyl chain correlation peak $S(Q_r)$ from 50° to 65°C obtained on the cold three-axis spectrometer V2-Flex (HMI, Berlin). Black dotted lines indicate single scans, in between which the intensity (logarithmic scaling, cf. Fig. 4.12) is interpolated.

4.2.3 Extracting Points of a Liquid Dispersion Curve

The experiments described in the following were based on the assumption that, if the DSPC-d70 model membrane showed similar liquid dispersive behavior, it would most likely resemble the liquid one for DMPC-d54, especially in the low- Q_r and high- Q_r ranges. Obtaining differences in the position and energy-depth of a potential dispersion minimum was therefore most emphasized.

The constant-energy scans were taken, where the slope of the curve is assumed to be steepest, energy-scans were taken immediately around the nearest neighbor peak position (Fig. 4.12), as well as in the high- Q_r and low- Q_r regime.

Because the excitations measured in liquids are weak due to a strong damping, the varying resolution properties of the two respective instruments had to be taken into account for specific Q_r - and energy-ranges. This was realized using the ILL matlab software package 'Rescal' (cf. Appendix B.5) which is optimized to deconvolute the specific instrumental resolution and the dynamic structure factor in the corresponding (Q_r, ω) -range from the measured intensities. The method of Popovici was applied because of its greater accuracy in comparison to the Cooper Nathans method (cf. 3.3.3).

Constant-energy Scans: Constant-energy scans obtained for DSPC-d70 at varying constant energies taken in the lipid's fluid phase are shown in Fig. 4.14. The data was fitted with a constant background and multiple Gaussians with the respective peak width fixed to the corresponding instrumental resolution at a specific point in reciprocal space (cf. Appendix B.5). This was necessary due to the weak Q -resolution of the cold three-axis instrument V2, as well as the in comparison large background. All scans shown in the following were smoothed with a Gaussian convolution of data points with the width 0.01 \AA^{-1} prior to fitting. The orientation of the instrument resolution ellipsoid calculated for specific points in (Q, ω) -space corresponds to the respective resolution focus visible in the data (cf. 3.3.3, Fig. 3.7): the excitations are broader at smaller Q_r and less intense than the more narrow ones at larger Q_r . Moreover, the excitations move apart in Q_r the higher the energy. An additional intensity contribution from the elastic chain peak at 1.47 \AA^{-1} can be distinguished at 3.0 meV (not fitted). However, even taking resolution effects into account, the results obtained from constant-energy scans are in this case no unambiguous evidence for the presence of excitations. Therefore we shall in the following mainly consider the energy scans that were taken.

Energy Scans: Energy scans obtained well within the respective gel and fluid phases for three distinct Q_r -values (1.0 \AA^{-1} , 1.47 \AA^{-1} and 2.3 \AA^{-1}) and, in the case of a potential minimum, also around the main phase transition at 55°C were evaluated based on the effective eigenmode model introduced in 3.2.3. The fits were performed after 'detailed balance' and absorption correction on the raw data (cf. 3.3.4, Appendix B.4.1, B.4.2).

Since the damped harmonic oscillator function converges towards a Lorentzian [101, 102], the latter was fitted to the data obtained for $Q_r = 1.0 \text{ \AA}^{-1}$ (Fig. 4.15) together with a constant background. A signal increase at low energies due to a quasielastic contribution, as well as a signal increase at high energies due to a contribution of the primary beam are observed in the raw data and have been subtracted as separate quadratic backgrounds prior to further evaluation.

The scans taken at $Q_r = 2.3 \text{ \AA}^{-1}$ (Fig. 4.17) did not cover the elastic line. A constant background was derived from the intensity contribution at high energies and fixed, the Gaussian width was held according to the instrumental resolution around the elastic line. The Lorentzian amplitude was approximated to the known contribution obtained for the elastic structure factor $S(Q_r)$. The excess intensity was then fitted by a damped harmonic oscillator.

For $Q_r = 1.47 \text{ \AA}^{-1}$ the scans were fitted simultaneously for three temperatures

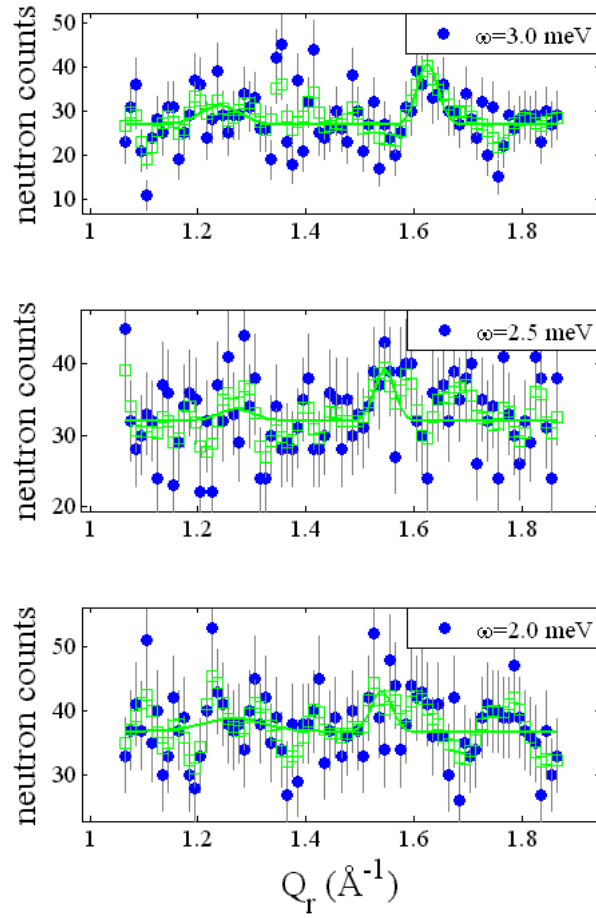


Figure 4.14: DSPC-d70 constant-energy scans at varying energies, measured in the fluid phase (65°C) on V2-Flex (HMI, Berlin). Blue dots correspond to raw data, green squares show smoothed data (see more in text), the green line corresponds to the fit of respectively two Gaussians (held fixed to instrumental resolution at specific point in (Q_r, ω)) with a constant background.

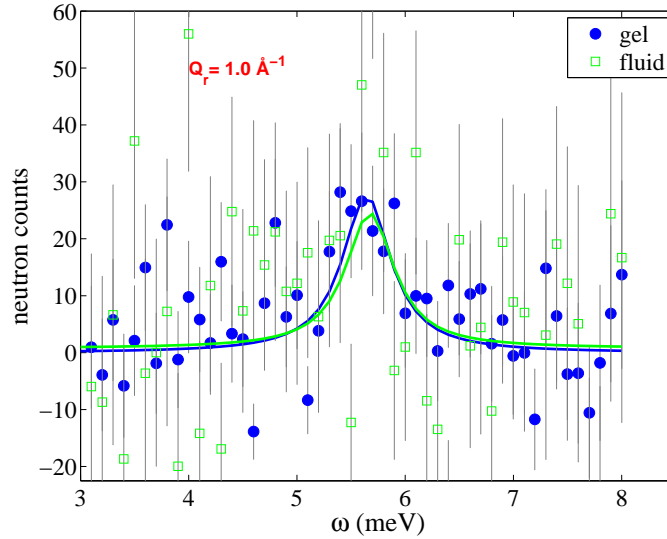


Figure 4.15: Energy-scans (V2) at $Q_r = 1.0 \text{ \AA}^{-1}$ taken at 50°C (gel phase, $\chi^2 = 0.85$) and at 65°C (fluid phase, $\chi^2 = 1.23$): Lorentzian fit (width fixed to resolution) with constant background could indicate an excitation near 5.7 meV in each of the respective phases, but gives no unambiguous proof of its existence due to the poor data quality.

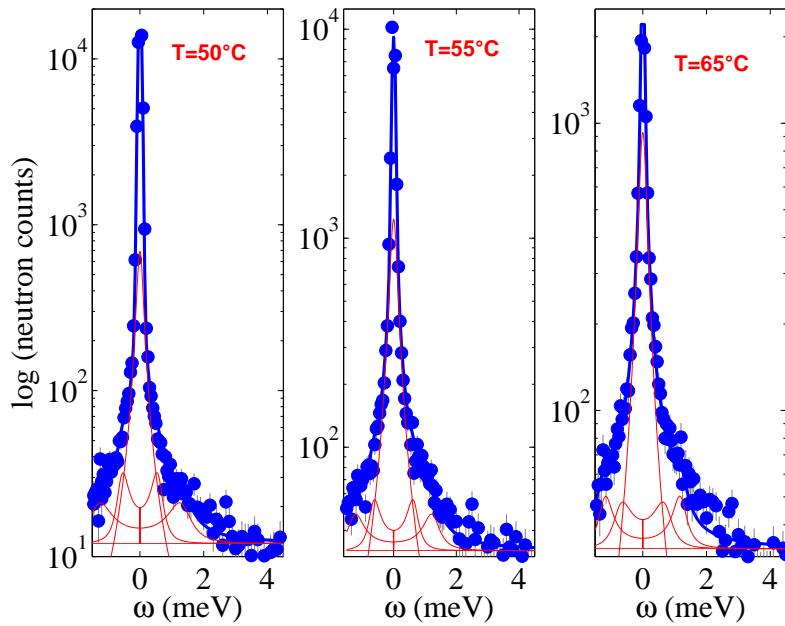


Figure 4.16: Energy-scans (V2) at $Q_r = 1.47 \text{ \AA}^{-1}$ (minimum): Fit of Gaussian (instrumental resolution around elastic line: width 0.05 meV), Lorentzian (quasielastic contribution, red line), two damped harmonic oscillators (inelastic excitations, red lines).

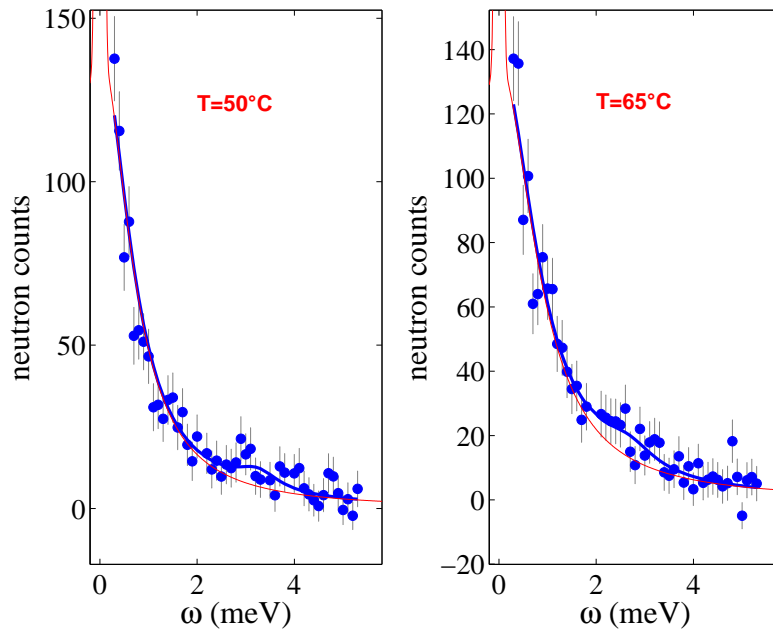


Figure 4.17: Energy-scans (V2) at $Q_r = 2.3 \text{ \AA}^{-1}$: Fit of Gaussian centered around elastic line with fixed width of 0.05 meV (instrumental resolution), Lorentzian centered around elastic line fixed according to corresponding elastic structure factor $S(Q_r)$, damped harmonic oscillator (inelastic excitation).

(Fig. 4.16) after subtracting a constant background. In addition to a central Gaussian and a central Lorentzian, two inelastic excitations were fitted with damped harmonic oscillators for the remaining excess intensity. For these excitations the positions were kept fixed at 0.7 \AA^{-1} and at 1.2 \AA^{-1} , as well as the resolution width. This way it was possible to show that the amplitude of the high- Q_r excitation grows with rising temperature, while the amplitude of the low- Q_r excitation decreases (Fig. 4.16), which again suggests a coexistence of the lipid's gel and fluid phases over a broad temperature range.

4.2.4 Summary and Conclusion

Apart from DSPC neutron reflectivities $S(Q_z)$, which point towards a phase coexistence around the main phase transition, in contrast to the previously investigated DMPC, temperature-dependent x-ray diffraction results support these findings of a phase coexistence in the chain peak $S(Q_r)$.

For both lipids the temperature-dependent acyl chain correlation peak $S(Q_r)$ was evaluated by Lorentzian fits. The inverse peak width ($1/\text{HWHM}$) yields the characteristic acyl chain correlation length $\xi_r(T)$, which for DSPC-d70 in the fluid

phase is by a factor of two larger than for DMPC-d54 [8]. The assumption of significantly larger in-plane domains around the main phase transition for DSPC-d70 (longer chains) is supported by the combined results for the in-plane and bilayer ordering obtained both by x-ray and neutron diffraction. Taking into account a neutron coherence length which lies in the order of 100 Å, one might obtain an average over domains of lipids in the gel and in the fluid phase for DMPC, while single domains of either phase could actually be probed for DSPC.

Analysis of the fluid chain peak (cf. Table 4.2) yields a larger in-plane correlation length $\xi_r(T)$ for DSPC than for DMPC in similar temperature ranges around the respective main phase transitions [8]. The correlation length $\xi_r(T)$ is related to decaying positional correlations which are considered to be a decisive criterium for the cooperativity of the phase transition. A quantification of the cooperativity of the main phase transition in phospholipid model membranes can be obtained from calorimetric scans (cf. 2.2.2) through the width of a $\Delta c_p(T)$ - peak. The cooperative units are domains of phospholipid molecules in either the lipid's gel or fluid phase. The melting enthalpy obtained from an excess heat capacity profile can therefore be linked to the size of domains around the transition temperature for each lipid (cf. 2.2.2). This unit size is significantly larger for DSPC than for DMPC.

The in-plane correlation length $\xi_r(T)$, in general, describes the positional correlations within each phase specifically. Analysis of the respective temperature dependent chain peaks with neutron diffraction shows that the in-plane correlations are for DSPC-d70 in every phase significantly larger than for DMPC-d54. The DSPC-d70 acyl chains seem to be able to collectively interact at the same energy exchange on a larger length scale than the DMPC-d54 chains, thereby evoking a distinct modulation of the propagating sound wave.

The collective in-plane density fluctuations can be related to changes in the properties of the bilayer bending modulus K_B . According to Heimburg et al. [67, 103] the bending modulus as well as the in-plane area compressibility $\kappa_T(T)$ depend on lateral area fluctuations, which are related to a distinct domain size through the characteristic melting enthalpy ΔH (Fig. 2.1, 2.7). A decrease in the bending modulus K_B and an increase in the area compressibility κ_T with increasing chain length match the observed energy minima obtained for respective points of the two dispersion relations.

Previous studies have investigated the influence of fluctuations in the membrane plane on its passive permeability (cf. 2.4.1). Nagle et al. link the in-plane correlation length ξ_r of the membrane to its lateral compressibility, which shows a proportionality to the permeability. In a series of experiments Paula et al. systematically vary

the bilayer thickness as well as the permeating molecules. The presented data show a distinct relationship between acyl chain length and collective in-plane dynamics, which is likely to influence membrane permeation.

Altogether, it seems that the 'anomalous swelling' which occurs in the lamellar D_z -spacing of several phospholipids is not coupled to the collective in-plane fluctuations. The observation of a phase coexistence in the inelastic data and the elastic data, as well as the indications found for the existence of a dispersion minimum in the inelastic data strongly suggests that the 'weak crystallization' theory is indeed the favorable one.

Chapter 5

Cholesterol in Model Membranes

In this chapter the structure and collective dynamics of a DMPC/Cholesterol model membrane are studied. Cholesterol is known to regulate membrane fluidity, permeability and the lateral mobility of proteins. The physical properties and the corresponding biological functionality induced by Cholesterol strongly depend on the way it partitions in the membrane (cf. 2.3.2). In the first section of this chapter the DMPC/Cholesterol system is characterized by concentration- and temperature-dependent small-angle and wide-angle x-ray diffraction on solutions of multilamellar vesicles (MLV).

Within distinct phases identified in the x-ray experiments, complementary neutron diffraction measurements were performed on oriented samples. The results are shown and discussed the corresponding collective in-plane dynamics. The observations are compared to experimental findings for single lipid membranes as described in the previous chapter as well as molecular dynamics simulations of simple model membranes consisting of pure DMPC [8, 80]. For single lipid membranes the results yield a typical liquid dispersion relation, which shows a 'de Gennes'-type behavior: A minimum in the dispersion curve is located at the position of the nearest neighbor peak. In the second section of this chapter it is investigated, how the insertion of Cholesterol changes the structure and the collective density fluctuations of the lipid acyl chains, and more specifically the liquid type of behavior observed in single lipid membranes.

5.1 X-ray Diffraction: DMPC/Cholesterol Phase Diagram

The structural characterization of the DMPC/Cholesterol phase diagram was performed on two different setups: The in-house diffractometer WENDI (cf. 4.1.1), provides information on the temperature-dependent structural changes at small an-

gles at varied concentration. In addition, detailed information on the temperature and concentration dependent wide-angle structure factor was obtained. Additional concentration dependent small-angle x-ray scattering scans taken at the ID02 beamline (ESRF in Grenoble, France) complement the in-house results and provide higher resolution.

5.1.1 Experimental

Samples The composite membrane samples for both x-ray diffraction experiments consisted of multilamellar vesicles (MLV's) like for the previously discussed single component model membranes DMPC and DSPC. The lipids (DMPC, Cholesterol) were purchased from Avanti (Alabaster, AL) and dissolved in Chloroform/TFE (1:1) in the desired molar proportions to achieve a homogenous mixture of the components. The solvent was subsequently evaporated over the course of two days at room temperature in a vacuum oven and the dry lipids were hydrated with Millipore water at a concentration of 200 mg/ml, heated from room temperature up to 60°C, ultrasonicated in a bath and cooled down to room temperature again several times subsequently. The suspension was then kept at a constant temperature of 36°C overnight to ensure the formation of MLV's (multilamellar vesicles).

WENDI-Experiment: A description of the instrumental setup of the in-house diffractometer is given in the previous chapter. Temperature dependent x-ray diffraction measurements consisted of small-angle scans in the range from $Q_z=0.05$ to $Q_z=0.5 \text{ \AA}^{-1}$ taken with 500 points counting for 30 sec and wide-angle scans in the range from $Q_r=1.0$ to $Q_r=1.8 \text{ \AA}^{-1}$ counting 100 points for 120 sec.

In addition to single SAXS measurements, continuous temperature ramps on the first 'Bragg' peak were taken running from 60°C down to 10°C for several Cholesterol ratios counting 80 points for 10 sec. The sample-holder for the different capillaries was inserted into a temperature chamber already used in the previous experiment on this instrument (cf. 4.1). This chamber is made of aluminum with capton windows and was operated by a standard thermostatic bath steered by the diffractometer control software 'spec'.

ID02-Experiment: Due to the high brilliance of an undulator source this instrument is well suited to study the microstructure and non-equilibrium dynamics of soft matter systems, allowing combined small-angle and wide-angle scattering within a Q-range of 0.01 nm^{-1} and 40 nm^{-1} at a wavelength of 0.1 nm. The distance of the SAXS area detectors can be varied between 1 m and 10 m with a Q-resolution of

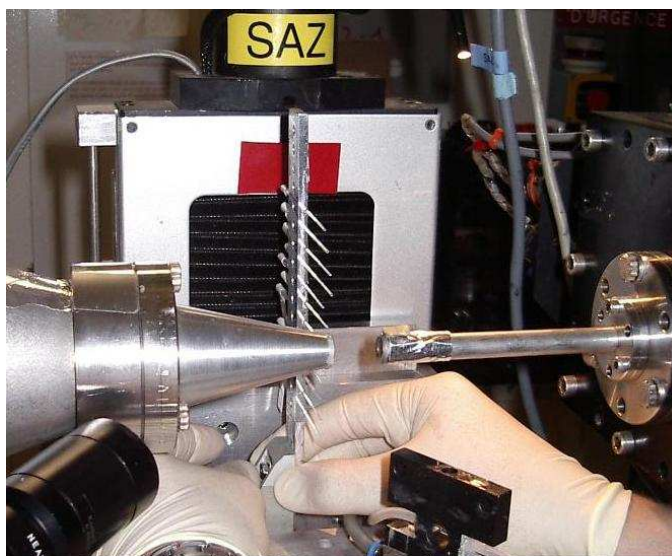


Figure 5.1: Photo take at ID02-beamline: adjustment of capillary holder; the beam impinges from the right, the detector tube is visible on the left.

about 0.003 nm^{-1} at the maximum detector distance for the mentioned wavelength. The beam size and detector resolution lie at $100 \mu\text{m}$.

A special feature of the beamline is the very low background due to the high degree of collimation of the undulator beam and widely separated optical components.

Sample capillaries were inserted into a standard sample holder offered at the beamline (photo, Fig. 5.1). No additional sample environment was included, all measurements were therefore carried out at room temperature around 22°C . For five Cholesterol concentrations (0, 5, 11, 20 and 40mol%), capillaries of 0.7 mm diameter at 12 different positions were inserted. Several scans were taken at each position with exposure times of 0.01 s and 0.1 s and detector distances of 2 m and 0.8 m, respectively.

5.1.2 Temperature Dependence

In order to obtain information on the overall molecular packing of lipid and sterol components, a combination of small-angle and wide-angle scans was taken for all concentrations and over a broad temperature range on the in-house diffractometer WENDI. This allows a distinct analysis of the in-plane order (acyl chain correlation) and corresponding bilayer stacking (lamellar repeat spacing) of the two components at varying conditions.

The results obtained for pure DMPC, which are presented in the previous chapter, serve as a reference for the discussion of the composite membrane. Temperature

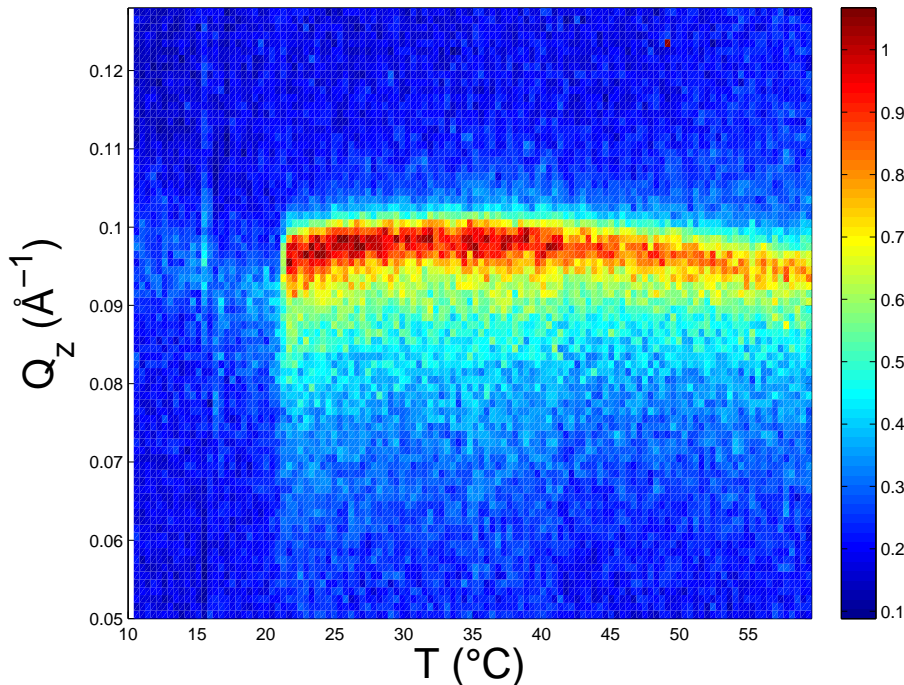


Figure 5.2: Change in Q_z around first SAXS peak from 10° to 60°C (temperature steps of 0.41°C in between single scans; normalized to maximum peak) for DMPC with 5mol% of Cholesterol (cf. Fig. 4.3 for pure DMPC). The signal weakness below the main phase transition at $T_m = 21^\circ\text{C}$ is explained assuming measurement along a concentration phase boarder within the temperature range shown.

ramps measured continuously around the first lamellar peak from 60°C down to 10°C (Fig. 5.2-5.8) for Cholesterol concentrations of 5, 12, 20 and 40mol% are discussed. The temperature intervals between single scans remained constant within each set of measurements and varied between 0.4° and 0.5°C for every Cholesterol ratio. Amplitudes and D_z -spacings were derived from analysis of the single scans and are shown in Fig. 5.10 and Fig. 5.11, respectively.

The temperature-dependent molecular in-plane ordering of DMPC and Cholesterol molecules is addressed simultaneously in the following. The temperature dependence of the acyl chain correlation peak at different Cholesterol ratios is shown in Fig. 5.3-5.9. The data was fitted with (two) Lorentzians and a linear background which is attributed to a contribution of the water peak located at 2.0 \AA^{-1} . The corresponding fit parameters are given in Table 5.1.

For 5mol% Cholesterol (Fig. 5.2), a clear drop in intensity in the temperature regime between $10^\circ - 20^\circ\text{C}$ occurs. The cause for this is seen in moving exactly on a concentration phase boundary within the observed temperature range. Around

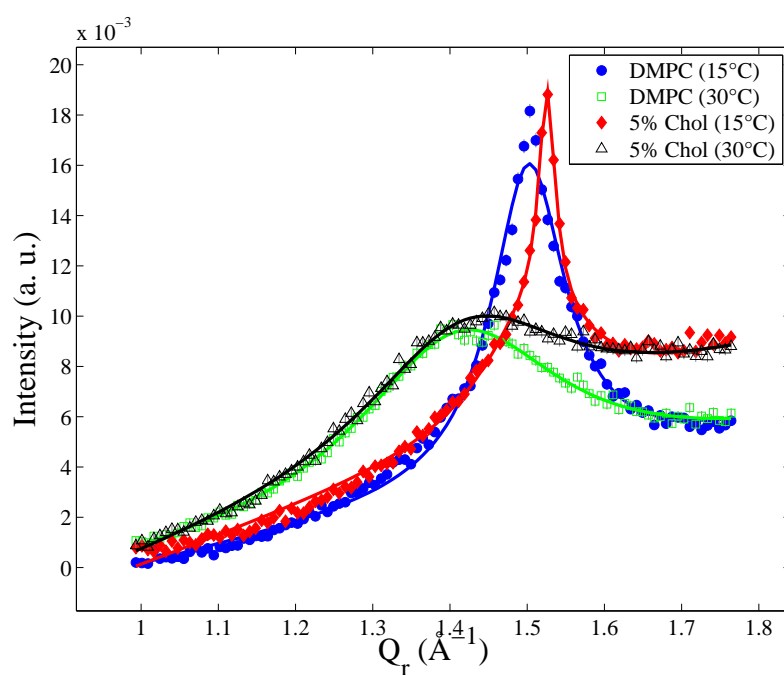


Figure 5.3: Temperature-dependence of acyl chain correlation peak measured at 5mol% Cholesterol in the solid S -phase at 15°C and in the liquid disordered L_D -phase at 30°C. Parameters of the Lorentzian fits are given in Table 5.1. Corresponding results obtained for pure DMPC in the gel phase at 15°C and in the fluid phase at 30°C are shown for comparison.

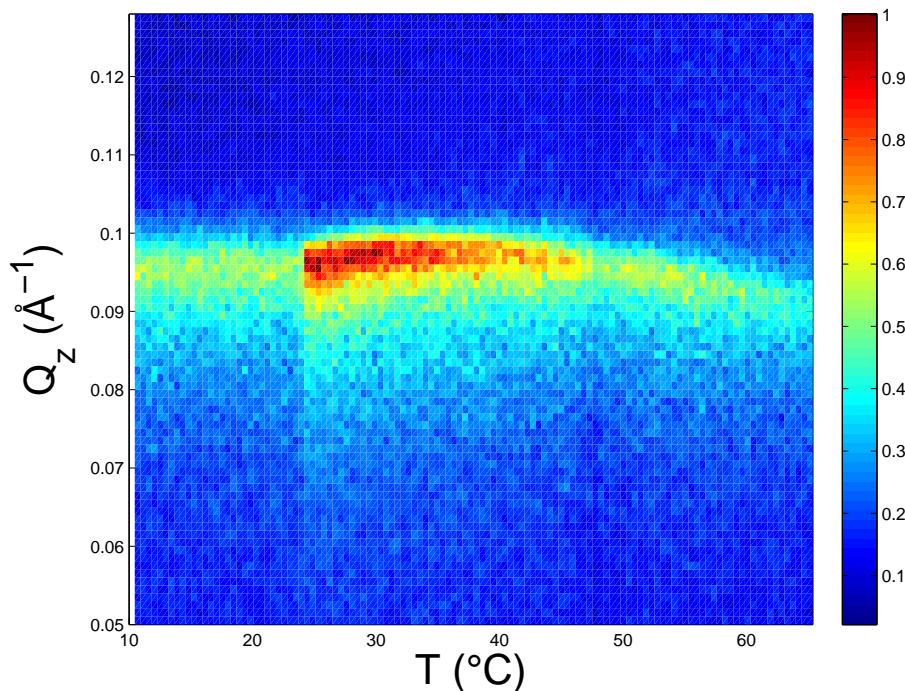


Figure 5.4: Change in Q_z around first SAXS peak from 10° to 60°C (temperature steps of 0.44°C in between single scans; normalized with respect to maximum peak) for DMPC with 12mol% of Cholesterol. Two phase barriers are crossed, one at 23.5°C, the other at 47.5°C.

16°C the temperature ramp shows a constriction which is attributed to the 'pre-transition' from the solid S -phase (cf. 2.3.2) to a less ordered ripple-phase. Until the main phase transition is reached at 21°C, a significant increase in the lamellar D_z -spacing is therefore observed (Fig. 5.11, (*top left*)). Here the lipids form vertical ripples which seem to be more pronounced than the ones observed in the pure DMPC membrane. This could be an indication that the origin of the ripples is no longer solely related to a headgroup tilt, but also a mechanism to overcome a mismatch between lipids in the solid S -phase and lipids in the liquid-ordered L_o -phase. Note that in a phospholipid/sterol membrane the L_o -phase is formed when Cholesterol moves below the lipid's headgroup at higher concentrations in order to avoid exposure to the interbilayer water ('umbrella model', cf. 2.3.2). Therefore a mismatch between lipids with and lipids without headgroup tilt occurs below the main phase transition temperature when the liquid-ordered L_o -phase is partially induced. Further evidence, that a concentration phase border is crossed in the low temperature regime, is found in the fit of a double Lorentzian (cf. Table 5.1) in the corresponding chain correlation peak (Fig. 5.3).

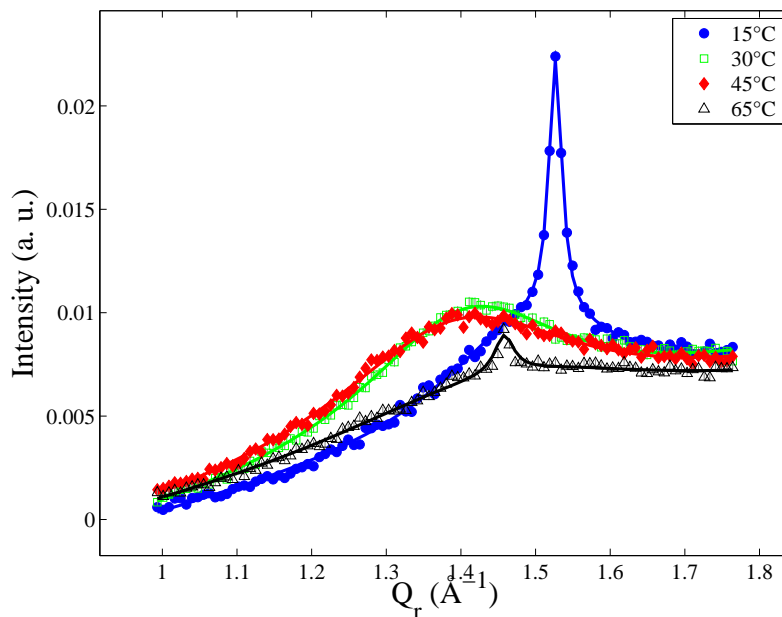


Figure 5.5: Temperature-dependence of acyl chain correlation peak measured at 12mol% Cholesterol: Note, that the temperature-dependence of the first SAXS peak (Fig. 5.4) indicates that a second transition occurs at 48°C, which marks the upper boundary of the liquid-liquid immiscibility gap (cf. Fig. 5.4).

At a ratio of 12% Cholesterol (Fig. 5.4), the temperature ramp shows constrictions at 23.5°C and 47.5°C, whereas at a ratio of 20% Cholesterol (Fig. 5.6) there are constrictions at 22.5°C and at 46.5°C. This strongly indicates the existence of two phase transitions for both concentrations. The one at the lower temperature is a remnant of the main phase transition, the one at the higher temperature is considered to indicate an upper boundary of the coexistence regime of the two liquid phases in the phase diagram.

Above the main phase transition, the lipids move apart due to the formation of kinks along their acyl chains (cf. 2.2.2), thus a free volume is created in the membrane plane into which the Cholesterol molecules can fit. Therefore a decrease in the D_z -spacings is observed in the corresponding temperature regime (Fig. 5.4 and 5.6; (*top right*), (*bottom left*)). This observation is supported by the fits of the corresponding chain peaks (Fig. 5.5 and 5.7) which consist of two Lorentzians below the respective main phase transition and single Lorentzians above (cf. Table 5.1). The origin of the separable peaks, which represent two types of in-plane correlations at 15°C is assumed to lie in a periodic height modulation along the bilayer normal. As this modulation ceases to exist at 30°C (Fig. 5.5 and 5.7), above the main phase transition, only a single average correlation between lipids in the liquid

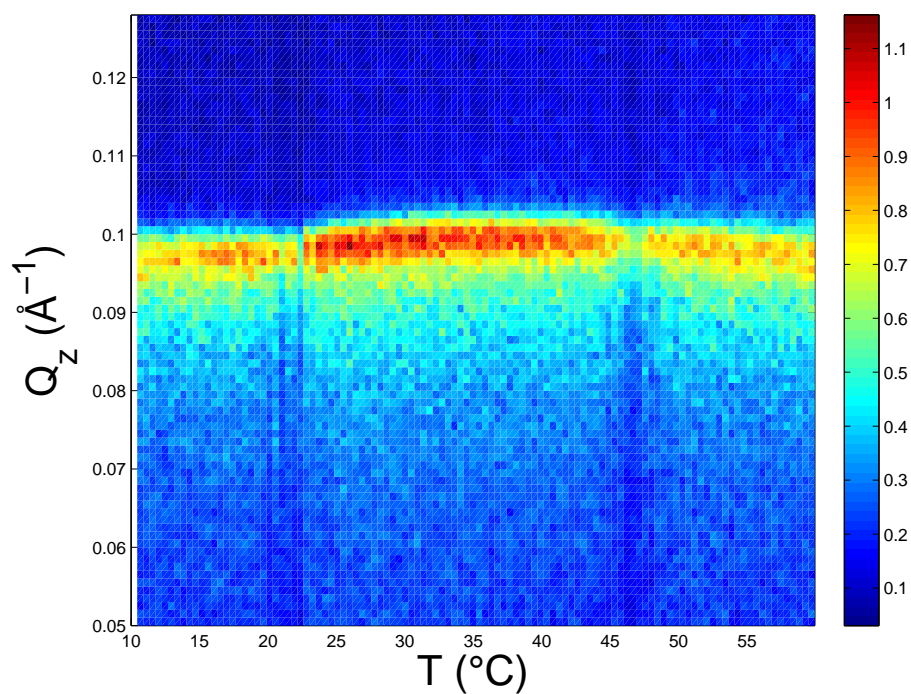


Figure 5.6: Change in Q_z around first SAXS peak from 10° to 60°C (temperature steps of 0.45°C in between single scans; normalized with respect to maximum peak) for DMPC with 20mol% of Cholesterol. Two phase barriers are crossed, one at 22.5°C , the other at 46.5°C .

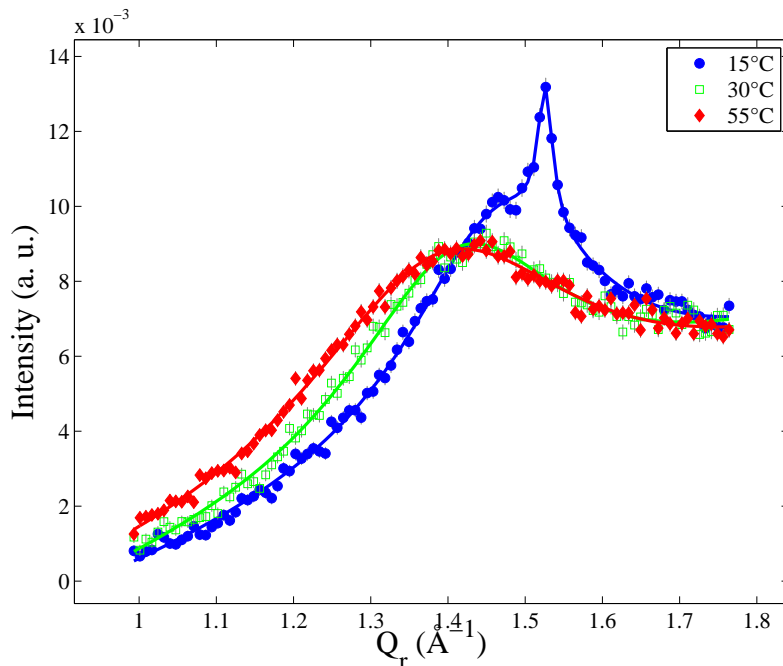


Figure 5.7: Temperature-dependence of acyl chain correlation peak measured at 20mol% Cholesterol: at 15°C, in the regime of the coexistence of the solid S - and the liquid-ordered L_o -phase, two peaks can be clearly separated.

disordered L_d - and the liquid-ordered L_o -phase can be distinguished. As the temperature increases further and a second phase boundary is crossed (Fig. 5.4 and 5.6), Cholesterol molecules can not only move along the direction of the bilayer normal, but also laterally to it [6, 51]. This combination of vertical and horizontal rearrangement of the sterol molecules in the membrane could eventually evoke a second type of ripple formation along the bilayer normal. This is indicated by the coexistence of two in-plane correlation peaks for 12mol% at 65°C, as well as by an increase in the bilayer repeat spacing D_z for both concentrations (Fig. 5.11, (*top right*), (*bottom left*)) in the corresponding temperature regime. The crossing of two temperature phase barriers is accompanied by distinct changes in the peak intensity, quantified in Fig. 5.10.

Because of its frequent occurrence in physiological membranes, the Cholesterol concentration of 40mol% is particularly interesting in terms of phase behavior (cf. 5.2). The 3-d plot of the temperature-dependency of the first lamellar peak (Fig. 5.8) yields no immediately visible phase transition. However, the temperature-dependent plot of the peak intensity (Fig. 5.10, *bottom right*) still suggests a remnant of the main phase transition, also observed at lower Cholesterol concentrations, around 20°C. This is only a weak indication, since in the same temperature-range the corre-

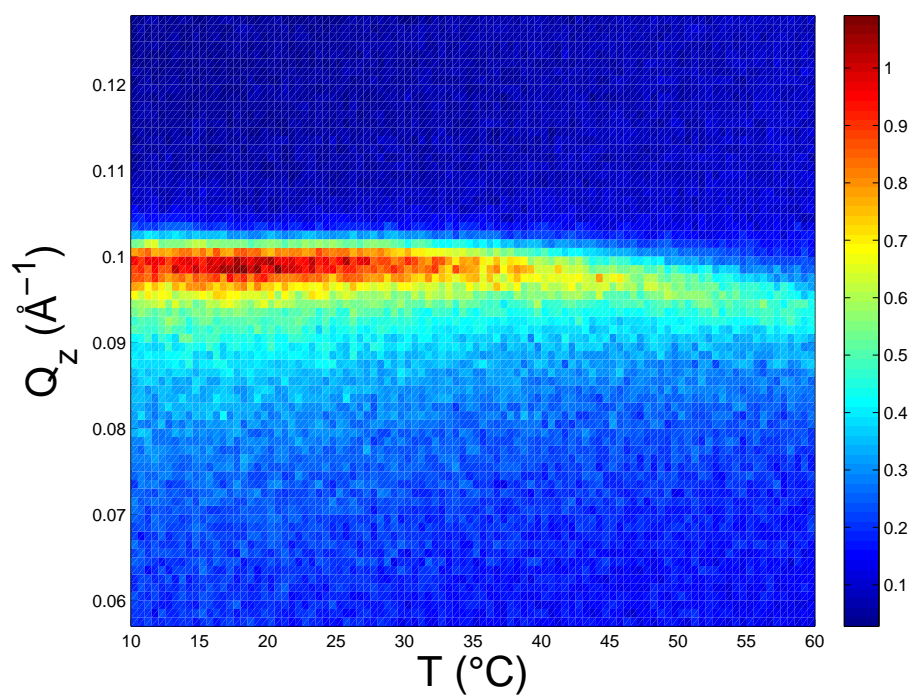


Figure 5.8: Change in Q_z around first SAXS peak from 10° to 60°C (temperature steps of 0.5°C in between single scans; normalized with respect to maximum peak) for DMPC with 40mol% of Cholesterol. No phase barrier is crossed.

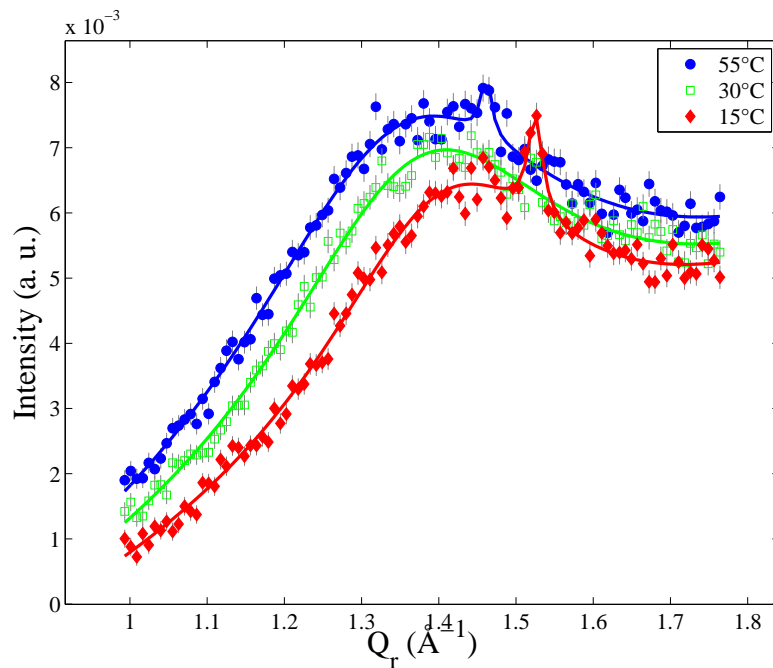


Figure 5.9: Temperature-dependence of acyl chain correlation peak measured at 40mol% Cholesterol; three different regions of the phase diagram can be distinguished: at 15°C the coexistence-regime of the solid S - and the liquid-ordered L_o -phase is observed, at 30°C merely the liquid-ordered L_o -phase and at 55°C a new phase, which has already been observed above the liquid-liquid immiscibility gap (cf. 12mol% Cholesterol at 65°C, Fig. 5.5, Table 5.1).

sponding D_z -spacing remains nearly constant at 64 \AA^{-1} , well below the corresponding values at lower concentrations (Fig. 5.11). At temperatures above 40°C , an increase in the lamellar repeat spacing is observed which exceeds the ones at lower Cholesterol ratios in the corresponding regime by several \AA 's. This could indicate that at least a fraction of the sterol molecules moves between the bilayer leaflets in order to obtain hydrophobic shielding, thereby reducing the effective in-plane Cholesterol concentration. Fits of the acyl chain peak at 40mol% Cholesterol at varying temperatures also suggest a weak presence of three distinguishable phases (Fig. 5.9): the double peak observed at 15°C is attributed to the previously discussed coexistence of the solid S - and the liquid-ordered L_o -phase. At a temperature of 30°C only a single peak is visible which differs from all other peaks in position and width (Table 5.1). It is therefore attributed to the purely liquid-ordered L_o -phase. At 55°C again a peak coexistence is found which, together with the previously mentioned strong increase in the lamellar repeat spacing D_z in this temperature regime, indicates the crossing of the second weak phase barrier. The position of the fitted satellite peak corresponds to the one found for 12mol% Cholesterol at 65°C (cf. Table 5.1).

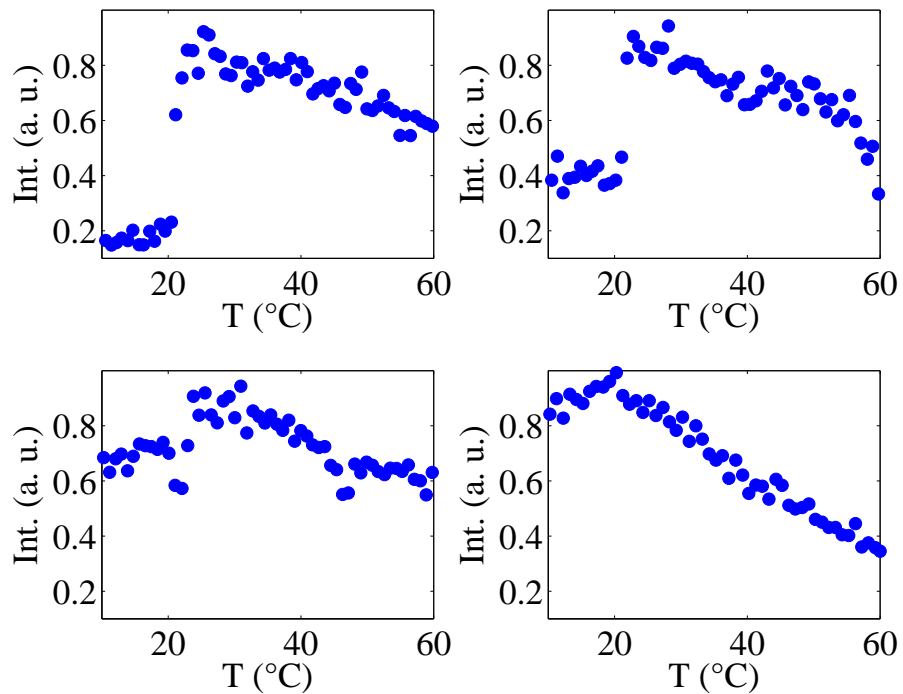


Figure 5.10: Intensity of the first lamellar 'Bragg' peak *vs* temperature obtained from temperature ramps for various DMPC/Cholesterol-ratios:

(*top left*) 5mol% Cholesterol (Fig. 5.2); (*top right*) 12mol% Cholesterol (Fig. 5.4);

(*bottom left*) 20mol% Cholesterol (Fig. 5.6); (*bottom right*) 40mol% Cholesterol (Fig. 5.8).

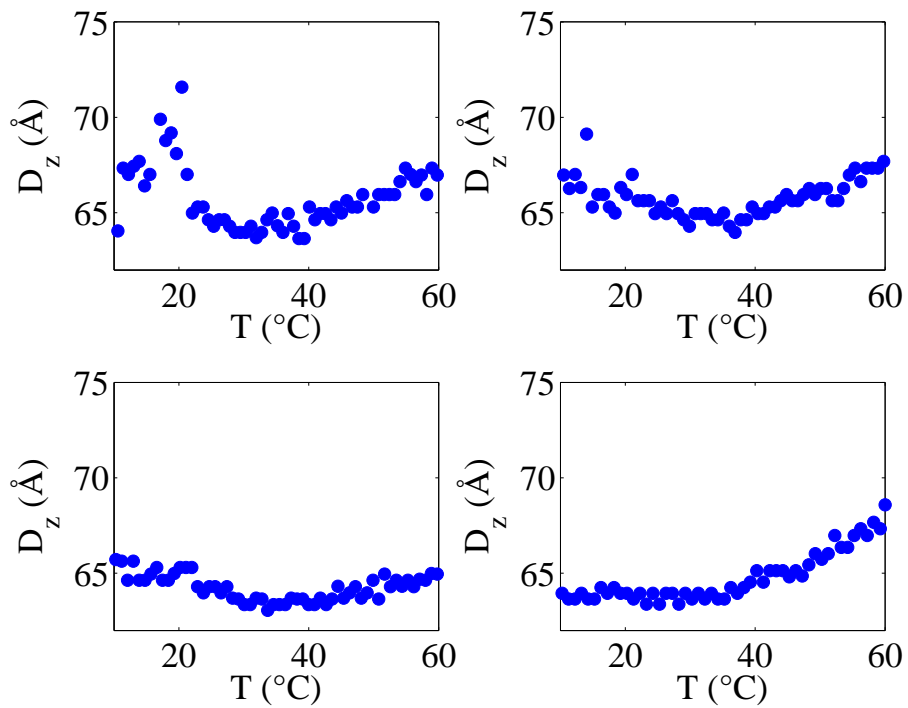


Figure 5.11: D_z -spacing derived from position of first lamellar 'Bragg' peak *vs* temperature obtained from temperature ramps for various DMPC/Cholesterol-ratios: (top left) 5mol% Cholesterol (Fig. 5.2); (top right) 12mol% Cholesterol (Fig. 5.4); (bottom left) 20mol% Cholesterol (Fig. 5.6); (bottom right) 40mol% Cholesterol (Fig. 5.8).

x_c (mol%)	T (°C)	Amp. (a. u.)	Pos. (\AA^{-1})	HWHM (\AA^{-1})	Amp. (a. u.)	Pos. (\AA^{-1})	HWHM (\AA^{-1})
0	15	0.0126(2)	1.5020(9)	0.0291(9)			
0	30	0.0069(1)	1.4133(14)	0.0811(18)			
5	15	0.0046(4)	1.5124(32)	0.0437(44)	0.0086(5)	1.5256(7)	0.0066(7)
5	30	0.0056(1)	1.4216(22)	0.0832(29)			
12	15	0.0052(2)	1.4926(27)	0.0730(33)	0.0125(3)	1.5267(3)	0.0053(2)
12	30	0.0065(1)	1.4070(16)	0.0856(22)			
12	45	0.0064(1)	1.3943(22)	0.1023(32)			
12	65	0.0038(3)	1.4497(71)	0.1432(11)	0.0019(0)	1.4580(14)	0.0080(0)
20	15	0.0064(1)	1.4694(25)	0.0755(22)	0.0036(3)	1.5260(8)	0.0059(7)
20	30	0.0058(1)	1.4137(24)	0.0872(32)			
20	55	0.0061(1)	1.3916(25)	0.1099(38)			
40	15	0.0041(1)	1.4093(40)	0.1009(51)	0.0015(2)	1.5250(0)	0.0059(0)
40	30	0.0048(1)	1.3766(33)	0.1165(53)			
40	55	0.0053(2)	1.3532(37)	0.1275(59)	0.0009(2)	1.4617(20)	0.0041(0)

Table 5.1: Parameters of fit of acyl chain correlation peak with (two) Lorentzians for temperatures and concentrations measured on in-house diffractometer WENDI.

5.1.3 Concentration Dependence

The influence of the Cholesterol concentration on the in-plane ordering of the phospholipid acyl chains and effects on the corresponding bilayer ordering are discussed. The chain peaks for all concentrations in temperature regimes above and below the main phase transition are shown in Fig. 5.12 and 5.13. Parameters of the corresponding fits of two Lorentzians are given in Table 5.1.

At 15°C the lipid molecules are generally packed closely together in the membrane plane. Partially inducing Cholesterol evokes a phase mismatch between lipid molecules, which exhibit a headgroup tilt with respect to the bilayer normal (solid S - and liquid disordered L_d -phase), and straightened lipid molecules (liquid-ordered L_o -phase). The latter have changed conformation under the influence of sterol molecules seeking hydrophobic shielding beneath the lipid headgroups [45]. For a DPPC/Cholesterol the formation of ripples along the bilayer normal as a mechanism to adjust to the mentioned phase mismatch has been studied [47, 49]. In this membrane, the in-plane periodicity of the height modulation normal to the bilayer was found to be linked to the sterol ratio.

The present data obtained for DMPC/Cholesterol at 15°C for varying concentrations (Fig. 5.12) might be interpreted in a similar manner. Previously discussed results on temperature-dependent bilayer ordering have suggested a concentration phase barrier of 5mol% Cholesterol. Therefore the well-known ripple phase $P_{\beta'}$, which occurs in pure DMPC membranes (cf. 2.2.1), is assumed to still be partially present. For higher Cholesterol concentrations the intensity of the small satellite peak decreases with rising sterol ratios (cf. Table 5.1). At the same time the width of the underlying acyl chain correlation peak increases, while its position changes to smaller Q_r (larger average in-plane distances of the lipid chains). This could be taken as an indication that the sterol molecules move towards the bilayer center and in between the lipid chains as the ripple periodicity increases with rising sterol concentration. The fact that the satellite hardly changes position or width at varying concentrations, could indicate that it might stem from an in-plane correlation of the sterol tail and lipid acyl chains evoked by the tight height modulated packing.

For varying Cholesterol concentrations around the liquid-liquid immiscibility gap at 30°C (Fig. 5.13) no peak coexistence is found. This suggests that above the main phase transition the in-plane distance of lipid molecules is large enough for Cholesterol to be inserted without ripple formation along the bilayer normal. In combination with the results for the corresponding bilayer ordering shown in Fig. 5.14-5.15, however, distinct phase regimes can be identified from the Lorentzian fits of the

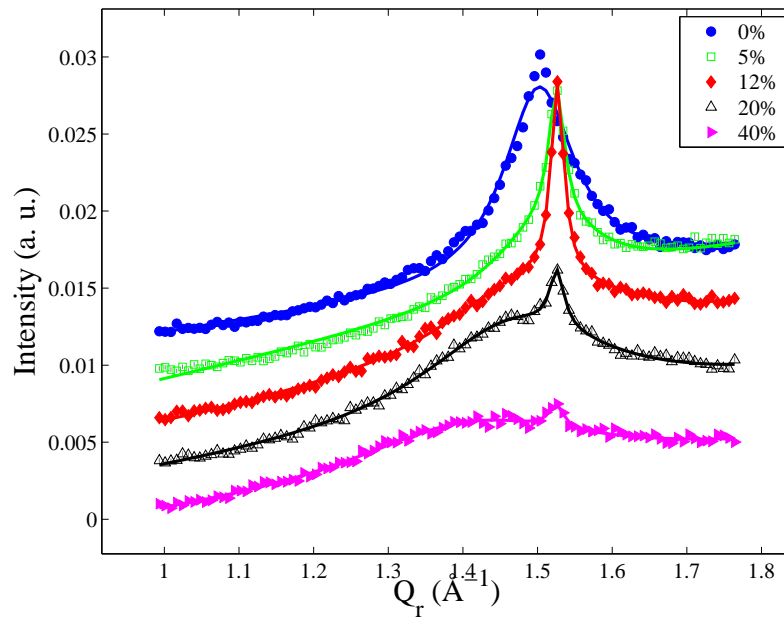


Figure 5.12: Concentration-dependence of acyl chain correlation peak at 15°C. Fits consist of two Lorentzians (solid lines). Corresponding fit parameters are summarized in Table 5.1. A constant offset on the intensity-axis was added for better visibility.

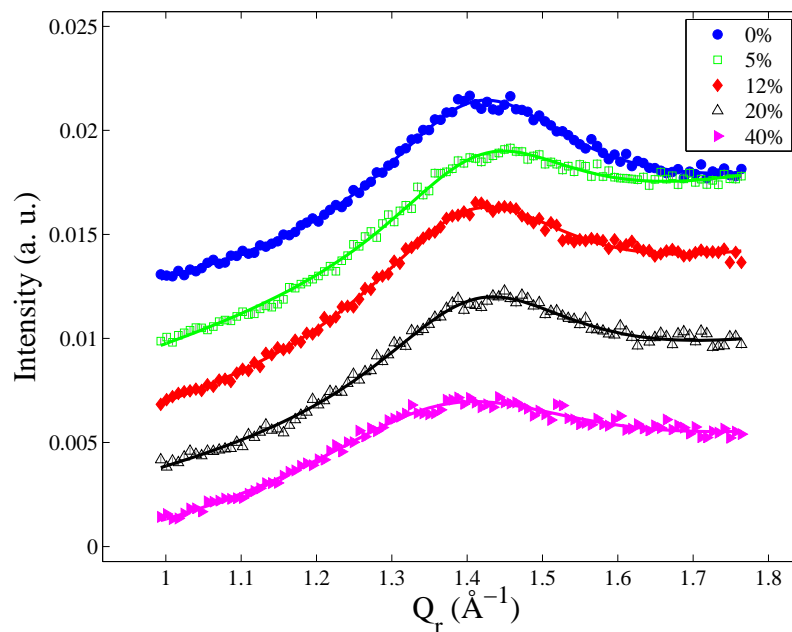


Figure 5.13: Concentration-dependence of acyl chain correlation peak at 30°C: A clear distinction between the liquid-ordered L_o - and the liquid disordered L_d -phase in the form of separate peak contributions is not possible (cf. Fig. 5.15). Therefore, single Lorentzians are fitted for each concentration (solid line). Corresponding fit parameters are summarized in Table 5.1. A constant offset on the intensity-axis was added for better visibility.

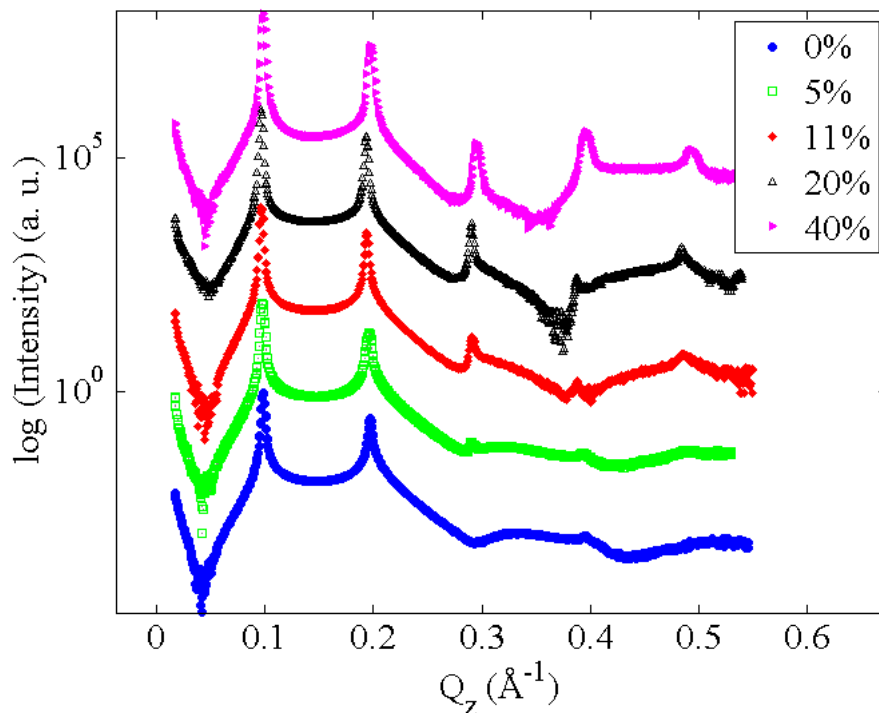


Figure 5.14: Semilogarithmic plot of SAXS scans measured at the ID02-beamline (ESRF in Grenoble, France) on solutions of multilamellar vesicles (MLV's) at room temperature. The detector distance was 0.8 m, the exposure time 0.1 s. A constant shift was added along the intensity-axis for better visibility.

chain peaks in the plane of the membrane (Table 5.1).

Despite having the largest in-plane distance (smallest chain peak position in Q_r), the lipid molecules seem to be the most homogeneously ordered into bilayers with 40mol% Cholesterol inserted (Fig. 5.14). The small lamellar repeat spacing D_z observed (Fig. 5.16) for the largest Cholesterol concentration, despite the sterol's tendency to straighten the lipid acyl chains by suppressing the formation of gauche isomers, seems counter-intuitive at first. However, it points towards a unique feature of this particular sterol in the liquid-ordered L_o -phase which has been described previously in literature: the partial protrusion of Cholesterol molecules into the opposite bilayer leaflet, which mends both monolayers together and thus stabilizes the membrane [6, 51, 104, 105].

In the coexistence regime of the liquid disordered L_d - and the liquid-ordered L_o -phase, a characteristic in-plane correlation length of 12 Å is obtained from the peak width for both concentrations according to $\xi_r = 1/\text{HWHM}$ (Table 5.1). The higher the Cholesterol ratio, however, the more the lipid molecules are pushed together by the sterol molecules, as indicated by the peak shift towards larger Q_r (Table 5.1).

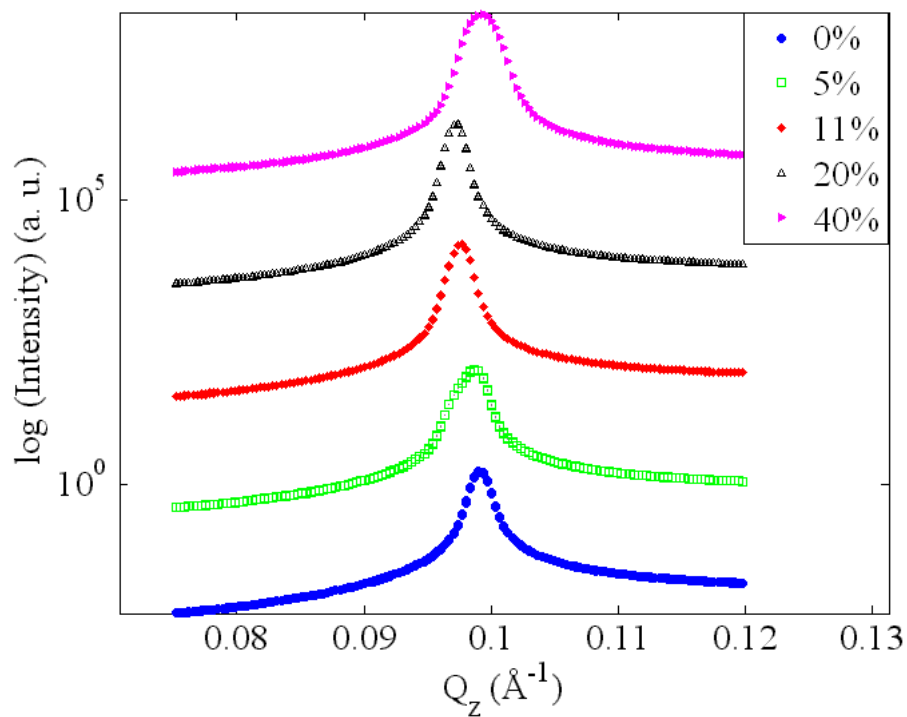


Figure 5.15: Semilogarithmic plot of SAXS-scans measured on solutions of multi-lamellar vesicles (MLV's) at room temperature. The first 'Bragg'-peak of the data plotted in Fig. 5.14 is shown. Scans were taken at a detector distance of 2 m and an exposure time of 0.1 s. After subtraction of a constant background, a shift along the intensity-axis was added for better visibility.

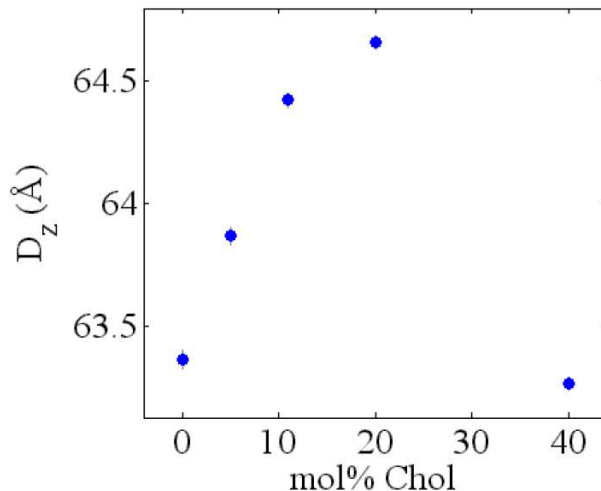


Figure 5.16: Lamellar repeat spacing D_z vs Cholesterol concentration as obtained from SAXS-scans on vesicle solutions above the main phase transition temperature (Fig. 5.15). The spacing is derived from Gaussian fits of the first 'Bragg'-peak.

Correspondingly, an increase in the lamellar repeat spacing D_z is observed (Fig. 5.15 and 5.16).

For a Cholesterol ratio of 5mol% above the main phase transition, the position of the chain correlation peak at larger Q_r indicates that the phospholipid acyl chains arrange closer together than for pure DMPC (Table 5.1). The straightening effect of the sterol molecules on the lipid acyl chains is also reflected in an increase of the corresponding bilayer spacing D_z (Fig. 5.16). A small additional peak shoulder towards smaller Q_z -values indicates the crossing of a concentration phase boundary towards the immiscibility gap (Fig. 5.15).

5.1.4 Summary and Conclusion

The results of the temperature- and concentration-dependent structural phase characterization are summarized in Fig. 5.17 and shall be discussed in the following. A qualitative resemblance with previously published phase diagrams is observed [37, 38, 42]. However, a few distinct observations were made regarding the phase barriers surrounding the immiscibility gap.

Comparison of the temperature-ramp of the first lamellar peak and the corresponding chain peak of the membrane containing 5mol% Cholesterol to the ones for 12mol% Cholesterol and pure DMPC, suggests the crossing of more than one phase barrier. The significant drop in the peak intensity could be an indication for moving along a concentration phase barrier in the corresponding temperature regime. In

addition to this, a 'pretransition' can be clearly distinguished at 16°C, as well as the main phase transition at 21°C. Whether or not the intermediate phase consists of lipids in the $P_{\beta'}$ -phase known to occur for pure DMPC, or a ripple phase P_{β} that is unique to phospholipid/Cholesterol membranes and was first introduced for DPPC/Cholesterol membranes, [47, 49] remains to be investigated.

For the higher concentrations the formation of P_{β} -ripples, which exhibit larger in-plane periodicities with increasing sterol ratio, as a mechanism to overcome a phase mismatch, could explain the data for the coexistence regime of the solid S and the liquid-ordered L_o -phase in a DMPC/Cholesterol membrane as well. Above the main phase transition no height modulation due to the lateral arrangement of coexisting phases can be distinguished, but three separate phase regimes are obtained from the analysis of the respective acyl chain correlation peaks in terms of the average distance of lipid chains as well the corresponding in-plane correlation length $\xi_r = 1/\text{HWHM}$.

The exact nature of the phase at high temperatures above the fluid-fluid immiscibility gap is still a matter of debate. On the basis of a time-resolved small-angle x-ray diffraction study, Richter et al. [41] suggest that in the liquid-ordered L_o -phase sterol molecules move towards the interior of the bilayer. This matches the observation of an increase in the lamellar D_z -spacing (Fig. 5.11). Corresponding diffusion processes of Cholesterol molecules have been observed with quasielastic neutron scattering (QENS) [6, 51].

The present study indicates that boundaries in the DMPC/Cholesterol phase diagram towards higher sterol concentrations are reached gradually as the product of a stepwise structural rearrangement of both molecules with respect to each other, laterally and along the bilayer normal. Unlike for single lipid membranes like DMPC or DSPC, where increased domain fluctuations occur around one prominent main phase transition, in a phospholipid/Cholesterol membrane controlled adjustment of phases over a broad range of temperatures and sterol concentrations is possible. Due to its largely hydrophobic nature, the Cholesterol molecule exhibits a general tendency to seek shelter from the inter-bilayer water below the headgroups of surrounding phospholipids ('umbrella model', cf. 2.3.2). Phase coexistences seem not to be accompanied by the formation of domains as it is observed, e.g. in single lipid model membranes around the main phase transition or membranes consisting of varying mixtures of phospholipids. Therefore phospholipid/Cholesterol systems in the purely liquid-ordered L_o -phase serve as stable barriers against transmembrane diffusion, whereas domain fluctuations [106] as well as the collective short wavelength in-plane chain dynamics have occasionally been linked to such transport phenomena [1, 2, 8].

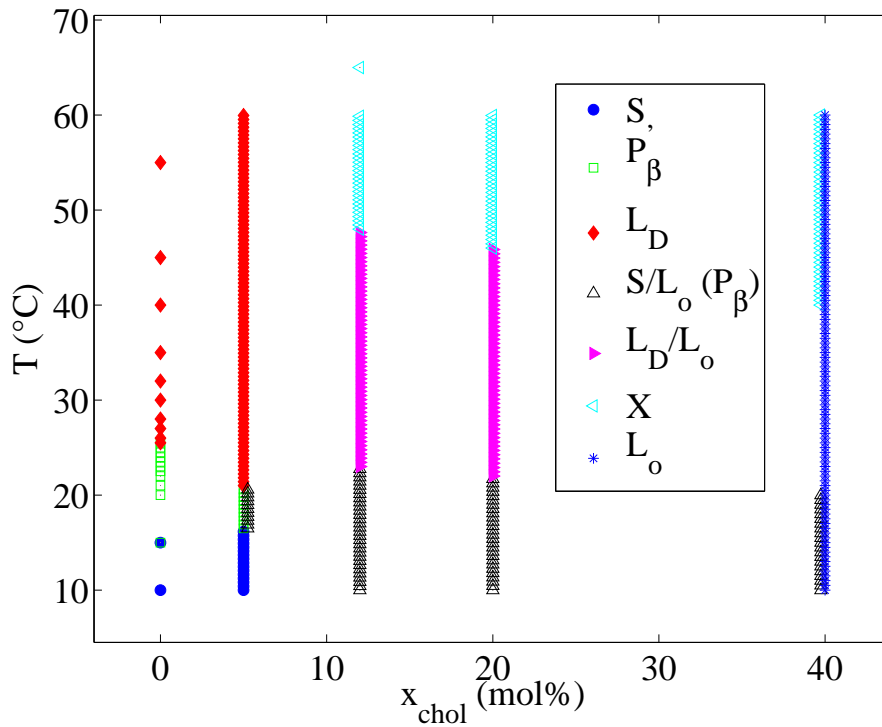


Figure 5.17: Overview of distinct phases in the DMPC/Cholesterol phase diagram as studied with small-angle (SAXS) and wide-angle x-ray scattering (WAXS) at the in-house diffractometer WENDI and at the ID02-beamline (ESRF). Lamellar phases (cf. 2.2.1): the solid S -phase corresponds to the pure lipid's gel phase, ripple phase ($P_{\beta'}$) and the liquid disordered L_d -phase which corresponds to the pure lipid's fluid phase; liquid-ordered L_o -phase (2.3.2): lipid serves as an 'umbrella' to shield Cholesterol from water, therefore its headgroup tilt ceases to exist and the acyl chains straighten; coexistence regime of solid S and liquid-ordered L_o -phase seems to exhibit a characteristic height modulation (P_{β}), which can be distinguished from the lamellar ripple phase; a new phase X is found above the coexistence regime of the two liquid phases.

5.2 Neutron Scattering

DMPC-d54 bilayers with two different Cholesterol concentrations were investigated in a combined study on the three-axis spectrometers IN8 and IN12 to study the influence of the membrane-active molecule Cholesterol on the structure as well as the collective in-plane dynamics. In the previous section we have discussed the structural changes in significant regimes of the DMPC/Cholesterol concentration/temperature phase diagram obtained by x-ray diffraction on fully hydrated samples. Now we focus on the structure and corresponding short wavelength dynamics of a lipid bilayer under the influence of Cholesterol as simultaneously probed by the neutron three-axis technique.

5.2.1 Sample Preparation and Experiment

Highly oriented membrane stacks on silicon wafers were used, as in previous three-axis experiments (cf. 4.2.1), with a mosaicity better than 0.6 deg. The chain deuterated phospholipid DMPC-d54 as well as Cholesterol, both ordered from Avanti Polar Lipids with a total mass of about 400 mg, were dissolved in TFE/Chloroform (1:1) in the desired molar ratios of 5mol% and 40mol%. For each sample the solution with a concentration of 20 mg/ml was spread on 600 μm thick silicon wafers. The single wafers were placed on top of each other separated by small air gaps (cf. Fig. 4.10).

The high degree of order allowed to align the sample with respect to the incoming beam and distinguish between Q_z and Q_r (the component perpendicular and parallel to the membrane surface, respectively). The samples were kept in a vertically mounted temperature- and humidity-controlled chamber. For each concentration and temperature reflectivities $S(Q_z)$ were taken before changing to the in-plane scattering geometry to measure the corresponding elastic $S(Q_r)$ and inelastic structure factors $S(Q_r, \omega)$.

The experiments were performed at the ILL under the combined IN12 and IN8 Proposal CRG-958: *Collective dynamics in phospholipid model membranes studied by inelastic neutron scattering*.

5.2.2 Neutron Diffraction: Specific Points in Phase Diagram

The neutron diffraction results presented complement the previously shown x-ray diffraction results in two ways: On the one hand a contrast is obtained through the fact that neutrons probe the sample nuclei instead of its electron hull. On the other hand, an additional contrast was added by selective deuteration of the

mol% Chol	T (°C)	phase	D_z (Å)
5	15	S	60.64
5	35	L_d	52.46
40	24	L_o	55.34

Table 5.2: Lamellar repeat spacing D_z as derived from the maximum peak positions of reflectivity-scans in three distinct phases of the DMPC-d54/Cholesterol phase diagram (Fig.'s 5.18, 5.19), obtained on IN8.

phospholipid acyl chains. In contrast to the x-ray data, the chain correlation peaks and reflectivities shown therefore represent the phospholipids' in-plane and bilayer ordering, respectively, depending on temperature and sterol concentration, but probe the Cholesterol molecules themselves considerably weaker.

Reflectivity: Bilayer Repeat Spacing

Reflectivity scans $S(Q_z)$ were taken for 5mol% Cholesterol at 15°C and at 35°C and for 40mol% Cholesterol at 24°C. Fig. 5.18 shows reflectivity scans taken for 5mol% Cholesterol in the solid S -phase and in the liquid-ordered L_o -phase, respectively. The corresponding D_z -spacings as derived from the maximum positions of the peaks are given in Table 5.2.

At low Cholesterol concentrations the sterol binds preferably to the lipid head-groups [46, 107, 108, 109, 110], therefore the decrease in the bilayer thickness with rising temperature visible in Fig. 5.18 can be explained through a decrease in the effective length of the acyl chains due to the formation of kinks above the main phase transition which occurs around 21°C (cf. Fig. 5.2).

Fig. 5.19 shows reflectivity scans taken in the two distinct liquid phases, the liquid disordered L_d -phase for 5mol% at 35°C and the liquid-ordered L_o -phase for 40mol% Cholesterol at 24°C. Cholesterol has a highly ordering effect on neighboring phospholipids, which is marked by two major features comparing the two concentrations (Fig. 5.19): first, at 40mol% Cholesterol more higher order peaks appear with significantly larger amplitudes and no lower order peaks are suppressed in between. Second, the corresponding lamellar D_z -spacing is significantly larger than for the liquid disordered phase (Table 5.2). This indicates that the lipid acyl chains are either extended to a larger amount of *trans* configurations (cf. Fig. 2.5) in order to pack in-plane with the neighboring Cholesterol molecules, or that sharper interfaces between the bilayer and water layer occur at higher concentrations. The effect is in good agreement with the previously presented ID02 data (Fig. 5.14), which also

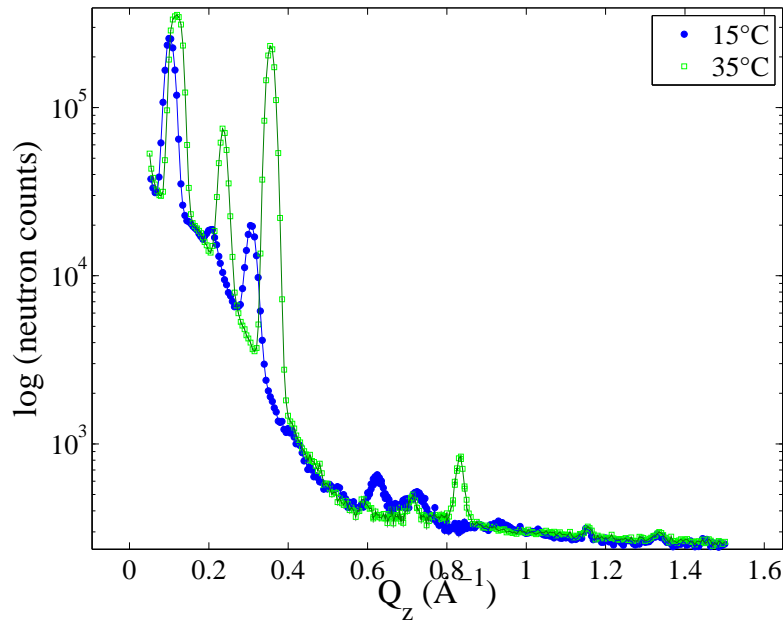


Figure 5.18: Temperature-dependence: reflectivity-scans for 5mol% Cholesterol taken on IN8; at 15°C in the solid S -phase, and at 35°C in the liquid disordered L_d -phase.

show an increase in the higher order peaks for the L_o -phase.

Acyl Chain Correlation: In-plane Ordering

The acyl chain correlation peak $S(Q_r)$ yields valuable information on the in-plane packing of the phospholipids under the influence of Cholesterol in each of the respective phases.

This information is needed in order to model the in-plane dynamics obtained from measuring $S(Q_r, \omega)$. Fig. 5.20 shows the Lorentzian fitted chain peaks in the three distinct phases: solid S for 5mol% Cholesterol at 15°C, liquid disordered L_d for 5mol% Cholesterol at 35°C and liquid-ordered L_o for 40mol% Cholesterol at 24°C. The position of the peak corresponds to an average in-plane distance of the lipid acyl chains in reciprocal space, its HWHM is inversely related to the in-plane chain correlation length ξ_r , according to [126]. Fit parameters are given in Table 5.3.

The position of the chain peak in the solid S -phase slightly deviates from the one obtained for pure DMPC which lies at about 1.475 \AA^{-1} . This can be explained with the additional in-plane volume used by the sterol molecules, which causes an increase in the lipid distance. The in-plane nearest neighbor distance as the inverse of the HWHM obtained from Lorentzian fits of the phospholipid/sterol system in the L_d -phase notably differs from the one observed for pure DMPC-d54 in its fluid

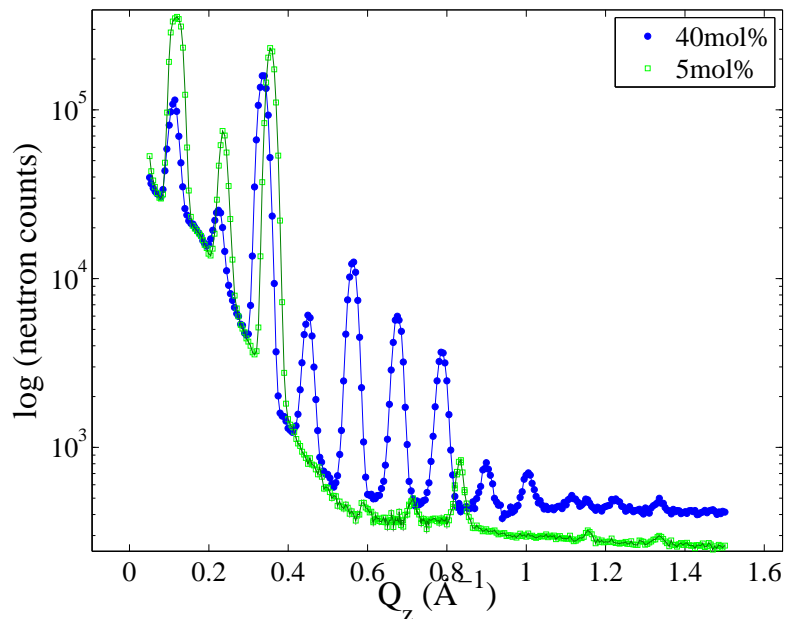


Figure 5.19: Concentration-dependence: reflectivity-scans in the two distinct liquid phases taken on IN8; the liquid disordered L_d -phase for 5mol% Cholesterol at 35°C, and the liquid-ordered L_o -phase for 40mol% Cholesterol at 24°C.

mol% Chol	T (°C)	position (\AA^{-1})	HWHM (\AA^{-1})
5	15	1.4658(10)	0.0351(9)
5	35	1.3659(46)	0.0818(35)
40	24	1.3601(15)	0.0754(11)

Table 5.3: Parameters of Lorentzian fit of the acyl chain correlation peak in the three distinct phases investigated (cf. Fig. 5.20).

phase at 1.465 \AA^{-1} (Table 5.3). This can be explained through the additional steric hindrance between the kinks in the lipid's acyl chains and the Cholesterol molecules. Thus, the temperature-dependent shift in the peak position from the S - to the L_d -phase is more pronounced than for the pure lipid [8].

The higher degree of in-plane ordering in the solid S -phase in comparison to the liquid disordered L_d -phase is reflected in the significantly larger amplitude and smaller width of the corresponding peak (Fig. 5.20, Table 5.3). The shift in the peak position at 5mol% Cholesterol to smaller Q_r with rising temperature reflects larger in-plane distances of the lipid molecules due to the greater space occupied by the acyl chains.

The chain correlation peak in the two liquid phases, the liquid disordered L_d - and the liquid-ordered L_o -phase, strongly resemble each other in peak position and

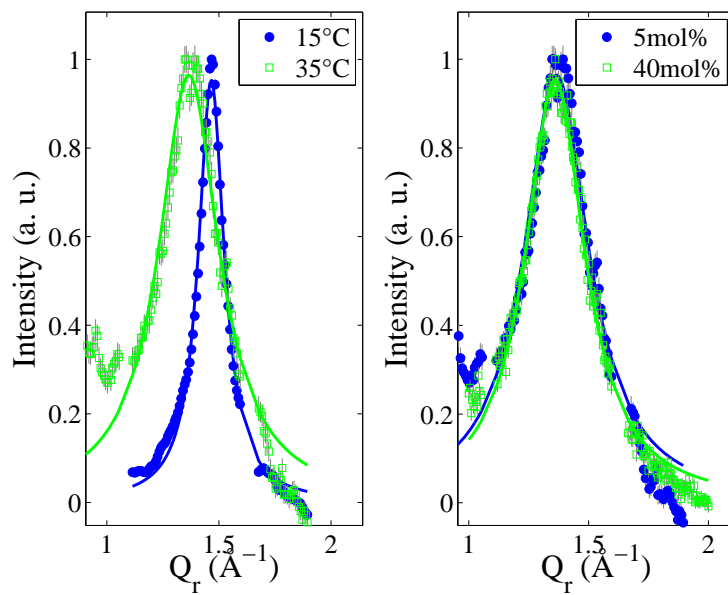


Figure 5.20: Acyl chain correlation peak in three distinct phases (IN8): (*left*) temperature-dependence: solid S -phase (blue) and the liquid disordered L_d -phase (green), (*right*) concentration-dependence: the liquid disordered L_d -phase (blue) and the liquid-ordered L_o -phase (green). The data was normalized to the respective maximum intensity. Strong aluminium contributions on both sides of the peaks stemming from the sample holder and environment were cut out prior to fitting, a constant background was subtracted. Parameters of the Lorentzian fits are given in Table 5.3.

width (Fig. 5.20, Table 5.3). It therefore seems likely that in both phases the lipid acyl chains show a similar degree of disorder and that the average lipid distance is determined mainly by the in-plane volume occupied by the rigid part of the sterol molecule.

5.2.3 Collective In-plane Dynamics in a Composite Membrane

The collective dynamics were investigated within the liquid disordered L_d - and the liquid-ordered L_o -phase at Cholesterol concentrations of 5mol% and 40mol%, respectively. The inelastic structure factor $S(Q_r, \omega)$ was measured by energy- and constant-energy scans. As a cold three-axis spectrometer with an energy resolution of about 300 μeV , IN12 is well suited for measuring inelastic excitations in the low energy regime of several meV. The main advantage of the thermal three-axis spectrometer IN8 for investigating the collective short wavelength dynamics is its sharp Q_r -resolution, which is well suited for constant-energy scans. Constant-energy scans were taken at lower energies at Q_r -values around the respective chain peaks (Fig. 5.20). The corresponding dynamics of single-lipid membranes and phospholipid model membranes under the influence of the sterol are compared.

For 5mol% Cholesterol (Fig. 5.21) the slope of the inelastic curve at high as well as at low Q_r yields information on the curvature of the dispersion. The inflection points shown by red lines mark intersections between different (inelastic) scattering contributions, one of which is for all scans located notably around the position of the acyl chain correlation peak and diminishes at higher energies (Fig. 5.20).

For 1.5 meV (Fig. 5.21, (*left*)) these inflection points appear at $Q_r = 1.0 \text{ \AA}^{-1}$ and at $Q_r = 1.7 \text{ \AA}^{-1}$ and move towards $Q_r = 1.0 \text{ \AA}^{-1}$ and at $Q_r = 2.0 \text{ \AA}^{-1}$, respectively, for 2.0 meV (Fig. 5.21, (*right*)). For 3.0 meV, the elastic contribution decreases and a clear change in the curvature occurs at about $Q_r = 1.8 \text{ \AA}^{-1}$. The slope of the curve for higher Q_r corresponds to the slope of the underlying dispersion relation. Fig. 5.22 exemplarily shows a constant-energy scan in the liquid-ordered L_o -phase which qualitatively resembles the ones in the liquid disordered L_d -phase.

Energy-scans taken on IN12 for both Cholesterol concentrations are shown together for varying Q_r in Fig. 5.23-5.26. The fits consist of a Gaussian for instrumental resolution around elastic line (red), Lorentzian for quasielastic contribution (magenta), damped harmonic oscillators for inelastic excitations (red), constant background (green). The blue line shows the overall fit.

A pairing of two sharp excitations is observed which are of significantly longer lifetime and occur with higher intensity than the corresponding ones observed in pure

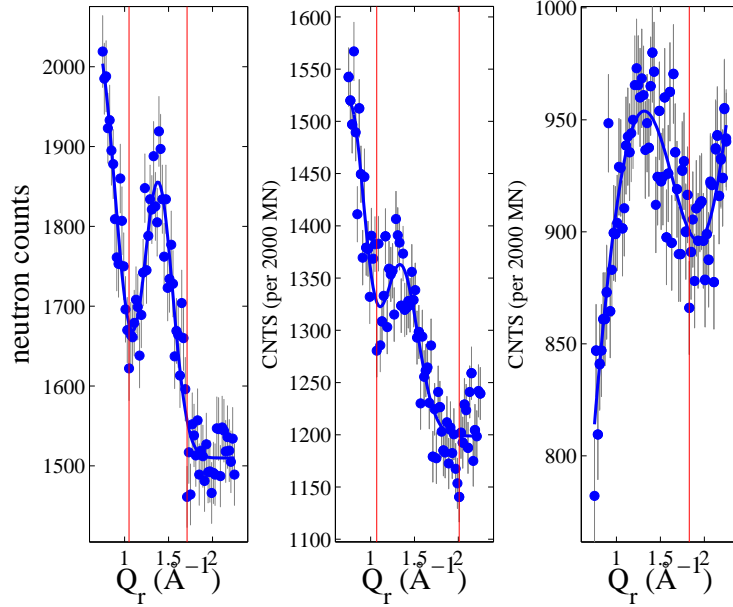


Figure 5.21: Constant-energy scans for 5mol% Cholesterol at 35°C (L_d -phase) as measured with $k_f = 2.662 \text{ \AA}^{-1}$ on IN8: (left) 1.5 meV; (middle) 2.0 meV; (right) 3.0 meV. A strong (inelastic) contribution is observed at the position of the lipid acyl chain correlation peak around 1.36 \AA^{-1} (cf. Fig. 5.20) for all three constant energies measured. Inflection points were determined as local minima and mark intersections between different (inelastic) contributions (red lines drawn to guide the eye).

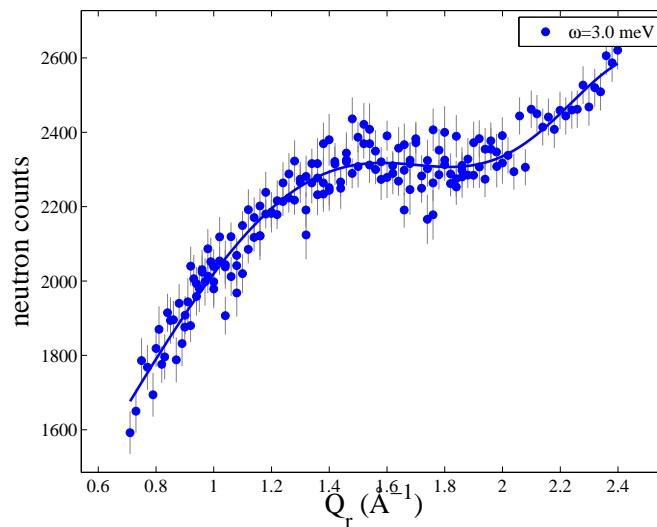


Figure 5.22: Constant-energy scan at 3 meV for 40mol% Cholesterol at 24°C (L_o -phase) measured on IN8 with $k_f = 2.662 \text{ \AA}^{-1}$. A strong (inelastic) scattering contribution is observed around the position of the elastic chain peak at 1.36 \AA^{-1} (cf. Fig. 5.20).

DMPC [8]. These excitations do not resemble the broad and highly damped ones obtained for liquids. Therefore a typical liquid dispersion curve with a minimum at the position of the nearest neighbor peak, following the predictions of de Gennes, is not obtained, although dispersive effects are observed. In the following, the energy scans shall therefore be discussed with respect to the effect of Cholesterol on the modulation of the collective chain fluctuations.

It is striking, that the position of the excitations hardly seems to depend on the Cholesterol concentration as does the acyl chain correlation peak $S(Q_r)$ (Fig. 5.20), despite the significant phase dependent changes in the bilayer repeat spacing $S(Q_z)$ (Fig. 5.19).

The most pronounced excitations for both concentrations are observed for $Q_r = 1.36 \text{ \AA}^{-1}$ (Fig. 5.24), the position of the acyl chain correlation peak (cf. Fig. 5.20, Table 5.3) in each of the respective phases. For $Q_r = 1.2 \text{ \AA}^{-1}$ similarly sharp but less intense excitations are visible. At $Q_r = 1.5 \text{ \AA}^{-1}$, on the other hand, energy scans show no excitation for both sterol concentrations. Therefore, the insertion of Cholesterol into the membrane seems to evoke a mechanism of mode selection. The characteristic nature of the latter Q_r -value in the two model systems remains to be discussed.

High Q_r -values correspond to small in-plane distances, therefore energy scans reflect single-particle behaviour [8]. For $Q_r = 2.5 \text{ \AA}^{-1}$ a difference between the excitations occurring for the two different model systems is clearly visible: while in the liquid disordered L_d -phase a pairing of excitations is again visible, only one of the excitations appears in the liquid-ordered L_o -phase. It strongly resembles the one observed in pure lipid membranes, such as DMPC-d54 and DSPC-d70 in position and width and can therefore be attributed to the collective motion of the phospholipid acyl chains. This particular excitation also occurs in the liquid disordered L_d -phase, but it is accompanied by another excitation which has a longer life time, but seems to be suppressed in the Cholesterol-rich liquid-ordered L_o -phase.

For $Q_r = 3.0 \text{ \AA}^{-1}$ a high energy excitation is observed at 15.2(6) meV in the liquid disordered L_d -phase and at 16.0(2) meV in the liquid-ordered L_o -phase (Fig. 5.27). In molecular dynamics simulations by Tarek et al. such a non-dispersive high frequency optical mode is predicted for pure DMPC and attributed to a rotation of the terminal methyl groups of the lipids' acyl chains directed towards the bilayer center [80]. According to the simulations, the mode is located at about 15 meV in the gel phase and moves to a lower frequency of 7 meV in the fluid phase. As the L_d -phase resembles the DMPC fluid phase, Cholesterol seems to shift the excitation towards energies otherwise found in the gel phase by straightening the lipid acyl chains.

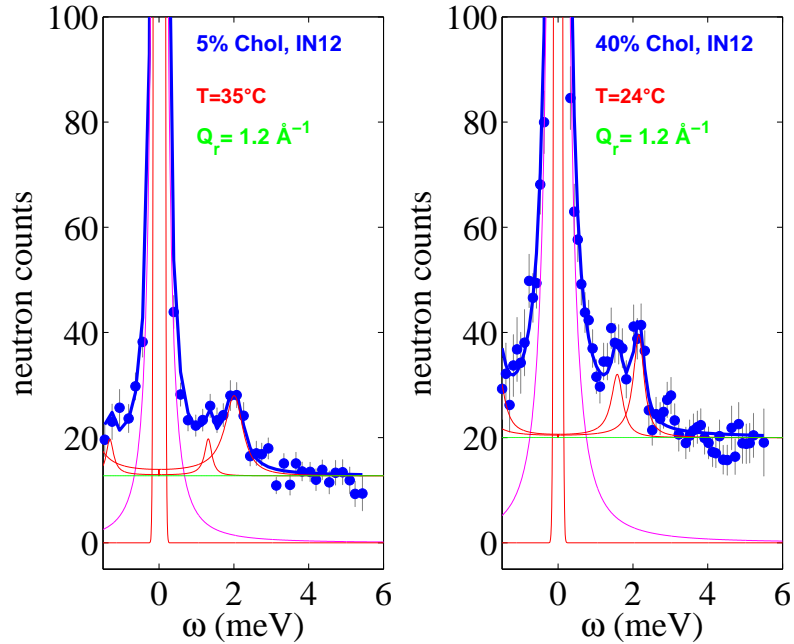


Figure 5.23: Energy-scans (IN12) at $Q_r = 1.2 \text{ \AA}^{-1}$ for 5mol% in the liquid disordered L_d -phase (*left*) and for 40mol% in the liquid-ordered L_o -phase (*right*). Fits consist of a sum of the central elastic peak (Gaussian, red), a broad quasielastic contribution (Lorentzian, magenta), a constant background (green), as well as the inelastic excitations in the form of two symmetric satellites (damped harmonic oscillators, red). The blue line shows the overall fit.

x_c (mol%)	Q_r (\AA^{-1})	amplitude (a.u.)	position (meV)	width (meV)
5	1.2	0.0111(92)	1.3271(768)	0.1178(1315)
		0.0920(217)	2.0500(604)	0.2921(905)
	1.36	0.0890(0)	1.7713(0)	0.1576(0)
		0.2604(579)	2.5591(387)	0.2422(665)
	2.5	0.1049(143)	3(0)	0.5770(907)
		0.0689(106)	4(0)	0.2332(473)
40	1.2	0.0363(443)	1.6032(1881)	0.1861(2459)
		0.0740(608)	2.1722(1058)	0.1716(1829)
	1.36	0.1422(693)	1.9195(1199)	0.2503(1486)
		0.1940(800)	2.6590(612)	0.1659(932)
	2.5	0.1424(325)	2.9064(1264)	0.5465(0)

Table 5.4: Fit parameters for inelastic excitations in IN12 energy-scans with damped harmonic oscillators shown in Fig.'s 5.23-5.26: (*top*) 5mol% Cholesterol at 35°C; (*bottom*) 40mol% at 24°C.

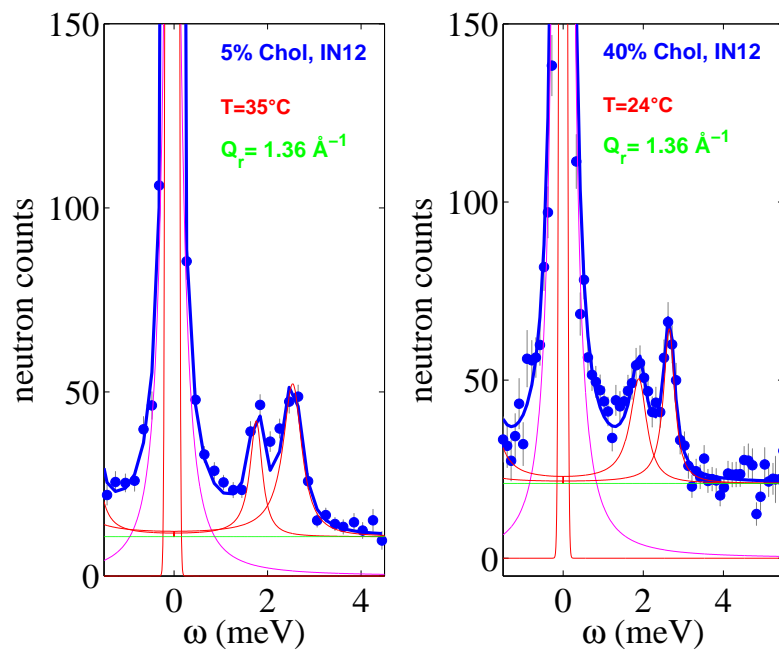


Figure 5.24: Energy-scans (IN12) at $Q_r = 1.36 \text{ \AA}^{-1}$ for 5mol% in the liquid disordered L_d -phase (*left*) and for 40mol% in the liquid-ordered L_o -phase (*right*). Fits consist of a sum of the central elastic peak (Gaussian, red), a broad quasielastic contribution (Lorentzian, magenta), a constant background (green), as well as the inelastic excitations in the form of two symmetric satellites (damped harmonic oscillators, red). The blue line shows the overall fit.

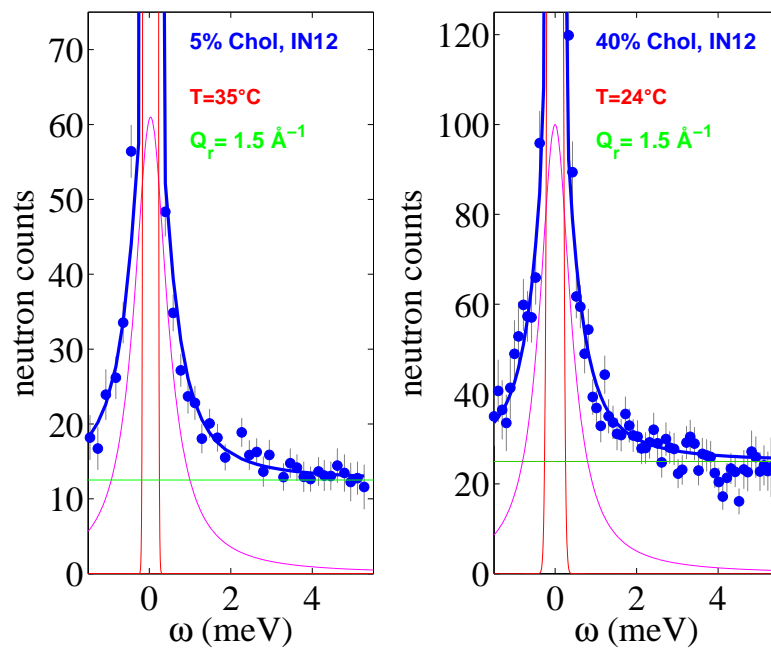


Figure 5.25: Energy-scans (IN12) at $Q_r = 1.5 \text{ \AA}^{-1}$ for 5mol% in the liquid disordered L_d -phase (*left*) and for 40mol% in the liquid-ordered L_o -phase (*right*). Fits consist of a sum of the central elastic peak (Gaussian, red), a broad quasielastic contribution (Lorentzian, magenta) and a constant background (green). Inelastic excitations observed at other Q_r -values for are fully suppressed. The blue line shows the overall fit.

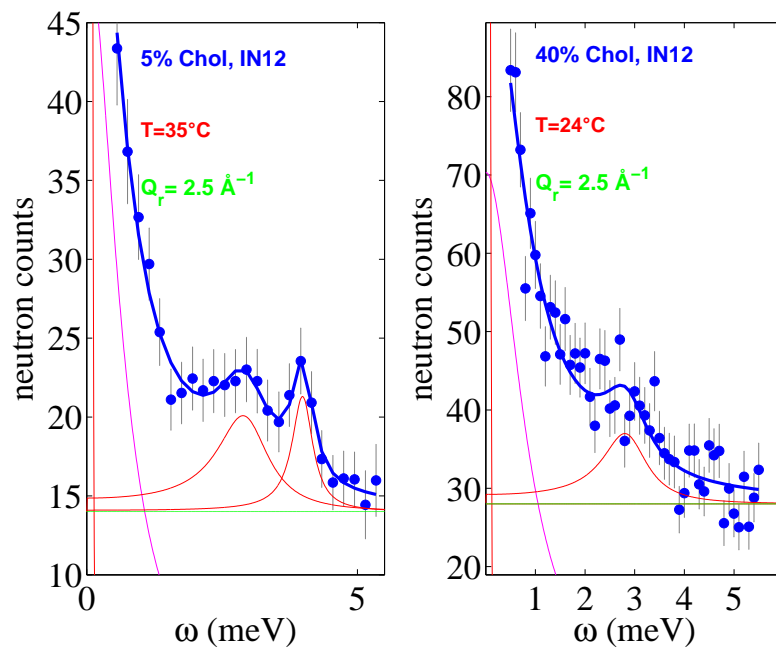


Figure 5.26: Energy-scans (IN12) at $Q_r = 2.5 \text{ \AA}^{-1}$ for 5mol% in the liquid disordered L_d -phase (*left*) and for 40mol% in the liquid-ordered L_o -phase (*right*). Fits consist of a sum of a broad quasielastic contribution (Lorentzian, magenta), a constant background (green), as well as the inelastic excitations in the form of (two) satellites (damped harmonic oscillators, red). The blue line shows the overall fit.

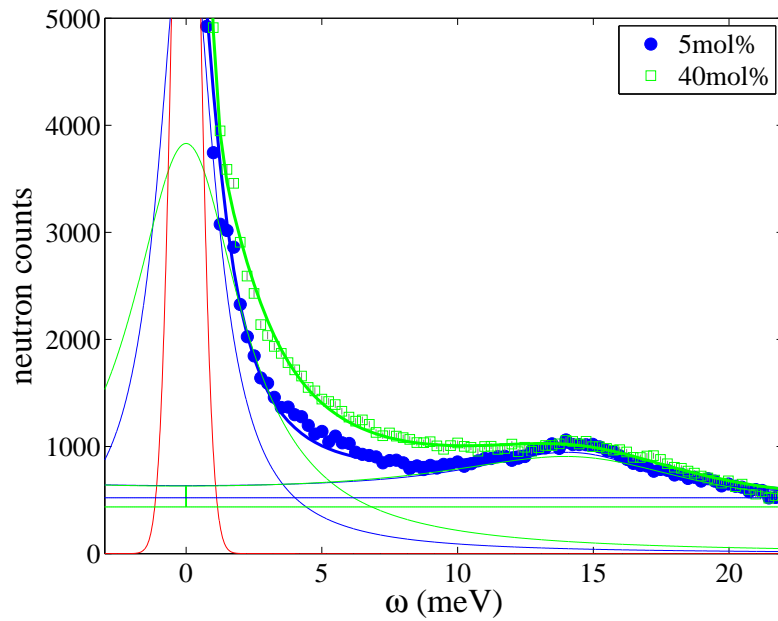


Figure 5.27: High-frequency energy scans (INS) at constant $Q_r = 3.0 \text{ \AA}^{-1}$ for 5mol% Cholesterol in the liquid disordered L_d -phase, and for 40mol% in the liquid-ordered L_o -phase. Fits consist of a sum of the central elastic peak for the instrumental resolution (Gaussian, red), a broad quasielastic contribution around the elastic line (Lorentzian), a constant background, as well as the inelastic excitation corresponding to a non-dispersive optical mode (damped harmonic oscillator). The overall fits are indicated by the bold lines.

5.2.4 Discussion

Model membranes consisting of single lipids have often been described as liquid crystalline phases in literature [111, 112, 113]. At the same time, the collective in-plane dynamics of these systems has been shown to exhibit properties similar to 3-d crystals investigated in solid state physics (such as the existence of optical and acoustic phonons) on the one hand, on the other hand properties of classical monoatomic liquids (de Gennes narrowing) [8, 80, 81]. In order to understand the effect of Cholesterol on the dynamics of the phospholipid acyl chains in a composite model membrane, both properties of a liquid and of a crystalline system have to be taken into account.

The origin of the two coexisting excitations at the dispersion minimum for pure lipid membranes (previous chapter) was explained by the coexistence of phases with gel and fluid domains, which each evoke a distinct modulation of the propagating sonic wave. Note that the in-plane sound velocity can be described as a function of area compressibility and area density according to $c_s = \sqrt{\frac{1}{\kappa_s \rho}}$ (κ_s : in-plane area density of lipid chain segments). The origin of the two sharp excitations in the composite membrane, can also be related to two distinct modulations of the collective in-plane density fluctuations of the lipid acyl chains. However, special care was taken in the preparation of the inelastic experiments to remain in single defined phases at all times (cf. section 5.1).

Despite the observation of distinct concentration-dependent superlattice structures of phospholipids and Cholesterol in literature [114, 115], the formation of domains with diameters larger than a few molecule distances can be excluded in all phases, which is explained by the 'umbrella model' (cf. 2.3.2): Due to its hydrophobicity Cholesterol seeks shelter from inter-bilayer water in close proximity to the surrounding phospholipids. Therefore it seems justified to assume that the two different excitations are caused by varying modulations of the collective motions of the lipid acyl chains themselves. The fact that the pairing of the two excitations observed in both phases do not differ much in their energy-positions and lifetimes suggests a rather robust and conformation and concentration independent mechanism.

In MD-simulations a significant change in the influence of Cholesterol on the lipid acyl chains for the two concentrations is observed only for the middle segments (6-10) [107] with slight deviation in its position along the bilayer normal. In a mechanical view the segments of the same chain can be regarded as linked to each other. One can assume that in a pure DMPC-d54 model membrane several coexisting modes

propagate as well as interfere. The sterol rings in the composite membrane can then be regarded as obstacles which could act similar to hinges, thus limit the propagation of certain modes and thereby evoke only specific interferences. In this picture one of the excitations would be linked to the collective motion of whole lipid acyl chains, the other to the collective motion of partial chains. In order to explain the similarity in the energy-position of the two excitations in both model membranes, the position of the sterol molecule along the bilayer normal would, however, have to remain approximately constant.

A variety of views have been offered regarding the exact vertical position of the sterol molecule in the lipid membrane throughout the phase diagram. Richter et al. use time resolved small-angle x-ray diffraction to investigate the molecular aggregation of DMPC and Cholesterol at varying temperatures and concentrations [41]. They propose that at higher temperatures in the liquid-ordered L_o -phase the sterol molecules diffuse towards the interior of the bilayer leaflet. Concluding from their MD-simulations of a membrane with 12.5mol% sterol Tu et al. state that Cholesterol has no preference to interact with a specific phospholipid molecule part with its hydroxyl group [110]. In fact at this particular concentration the rigid part of the sterol molecule can be distributed within a range of approximately 6 Å along the bilayer normal. Therefore the model system might also be considered as a 2-dimensional liquid consisting of two types of thin (chain segment) layers: one where a propagating sonic wave encounters the rigid body of a sterol molecule which has to be circumsized and one which can be passed directly via collective chain movement.

The two approaches might indeed both be seen as valid if one takes into account the motion of Cholesterol molecules along the bilayer normal in a phospholipid membrane in the liquid-ordered L_o -phase as observed in quasielastic neutron scattering studies [6, 51]. The authors study the motional degrees of freedom the sterol molecule has within the lipid membrane at varying temperatures. Whether or not a long range diffusion of Cholesterol into opposite bilayer leaflets can occur is determined by the conformation of the phospholipid acyl chains. At low temperatures the *all-trans* configuration is the predominant one, therefore the sterol molecules are tightly packed in between the lipid chains. With rising temperatures the in-plane distances of lipid molecules increase due to kink formation as do the motional degrees of freedom of Cholesterol molecules seeking hydrophobic shelter. This means also the number of end-*gauche* isomers in the lipid chains increases, which enables a protrusion of sterol molecules into the opposite monolayer. As a consequence, the two monolayers are bound together, which not only stabilizes the whole bilayer in comparison to other phases, but also forms distinctly sharper interfaces between

layers. The latter effect is observed in the SAXS-scans shown, as well as in neutron reflectivities.

The intensity of the paired excitations with respect to each other, however, depends on the Cholesterol concentration (cf. Table 5.4) and therefore suggests a distinct population of states for each of the respective phases.

The energy position of the high-frequency mode does not change with the phase of the DMPC-d54/Cholesterol system (L_o/L_d). For pure DMPC-d54 the excitation is related to a rotation of the chain's terminal methyl groups and its position depends on the lipid phase [80]. The position of the excitations observed here lies close to the one in the pure lipid's gel phase [8]. This can be taken as an indication that the rigid part of the sterol induces an alignment of the lipid's acyl chains along the bilayer normal closely resembling the *all-trans* configuration. Since the formation of multiple *gauche* isomers ('kinks') along the whole chains is at least partially suppressed in the given temperature and concentration range due to steric reasons, also the rotation of the terminal methyl groups is energetically less favorable.

5.3 Summary and Conclusion

In conclusion, what can be learned about the structure and collective in-plane dynamics from the presented study: The collective in-plane density fluctuations of the lipids under the influence of Cholesterol show only weak dispersive effects compared to pure DMPC. Excitations observed in the energy scans seem to be suppressed selectively, but are at the same time stronger and less damped than in their pure lipid counterpart. This is in particular the case at the nearest neighbor distance. A pronounced (inelastic) scattering contribution is observed around the position of the acyl chain correlation peak in the constant-energy scans. As in DMPC a high frequency optical excitation is observed, however, in contrast to the pure lipid's energy-position remains independent of the actual phase of the membrane. This can be understood on the basis of the ordering influence the hydrophobic rigid part of the Cholesterol molecules has on the lipids' acyl chains in either of the two phases. Since modes can no longer propagate isotropically, the DMPC/Cholesterol membrane can not be regarded similar to a simple liquid as modeled by de Gennes. Note, that single excitations as described by an effective eigenmode model (cf. 3.2.3) cannot be expected to describe a binary liquid [88].

Neither the position of the observed excitations nor their distinct life-time seems to show a pronounced dependence on the position of the sterol molecule along the bilayer normal. However, the relative intensity of the paired excitations changes

with respect to each other, depending on the phase. Apart from Cholesterol and saturated phospholipids, such as DMPC, neural membranes are known to also contain smaller amounts of unsaturated phospholipids which have a low affinity to bind to sterol molecules [70, 116, 117]. Studies of the interaction of these lipids with varying degrees of unsaturation with Cholesterol have revealed a tendency to regulate the effective in-plane sterol concentration [117, 118], which indicates a naturally occurring mechanism.

Based on the observed excitations, a picture is proposed where the rigid part of the Cholesterol molecule effectively shields parts of a fraction of the phospholipid acyl chains from propagating, and leads to a selection of specific modes. Through its position, as well as its effective in-plane concentration, a distinct modulation of the sonic wave is achieved by the rigid sterol body. Whether this modulation can be specifically influenced, would be interesting to study or by changing further parameters that determine the state of the membrane, e. g. pressure or ph-value.

Chapter 6

Ethanol in Model Membranes

In this chapter a composite DMPC/Ethanol membrane is investigated. Due to its small size and similar solubility with respect to unpolar and polar media, Ethanol increases the interfacial area of lipid and water. Concentration dependent bilayer unbinding gives valuable qualitative insight into membrane interaction potentials (cf. 2.2.4), as well as a possible structural reorganization, which accompanies the decay. As is common also to anesthetics (cf. 2.3.3), Ethanol induces a lateral pressure into the membrane. The effects of this lateral pressure are studied by adding varying osmotic pressures through a polymer osmolyte. High Ethanol concentrations, like high osmotic pressures, are found to induce a (partial) interdigitation (cf. 2.3.3).

A complementary structural characterization of the bilayer decay on a significantly larger time scale is given as obtained by neutron scattering. The observed lamellar repeat spacings D_z shows that the interdigitated phase was at least partially induced, which suggests significant changes in the corresponding collective chain dynamics. Scattering contributions to the elastic in-plane structure factor $S(Q_r)$ are introduced and possible implications for the observation of the coherent in-plane density fluctuations of the lipid acyl chains are discussed.

6.1 X-ray Reflectivity on Model Membranes

When measuring a reflectivity curve, the x-ray beam is commonly collimated to the order of hundreds of a degree and impinges on the sample at a glancing incidence angle α_i . The reflected intensity is recorded under specular conditions, therefore with an exit angle of $\alpha_f = \alpha_i$. Typically, the data is corrected for partial illumination of the sample on the one hand, as well as for a contribution of underlying diffuse scattering, which is subtracted. The diffuse scattering contribution is accounted for by an offset scan, which means by adding a slight offset $\Delta\alpha_i$ to the previous

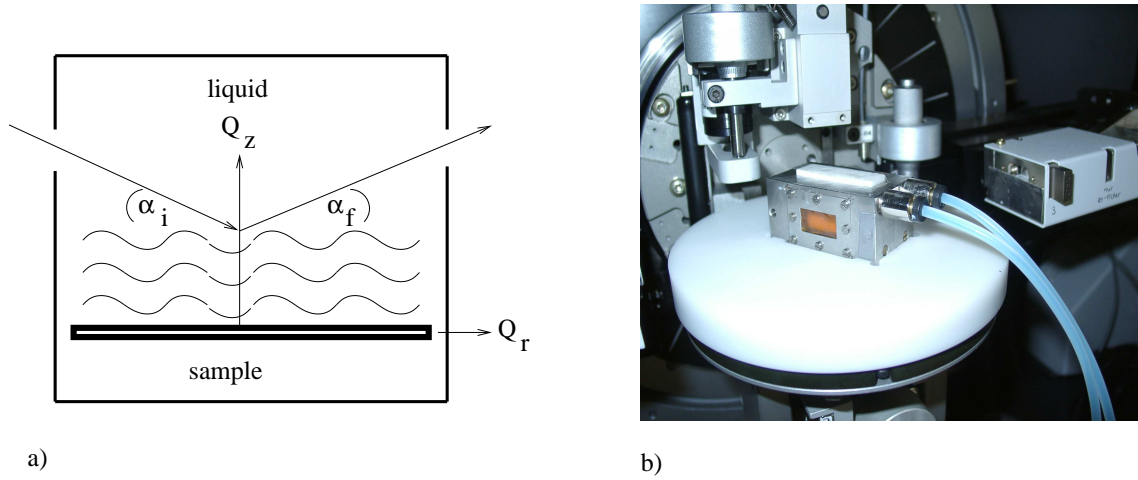


Figure 6.1: a) Schematic of the liquid cell for reflectivity measurements on highly oriented membranes in fluid environment; b) Photo of setup with sample tray for D8 Advance diffractometer: Teflon liquid cell (white) inside aluminum temperature block. The x-ray beam impinges on sample from the left side through Kapton windows, the detector tube with exchangeable slit is shown on the right.

calibration of α_i with respect to α_f . If the incident wave vector is denoted k_i and the exit wave vector k_f , the momentum transfer of the elastic scattering is always along Q_z , with a z -axis parallel to the membrane normal (Fig. 6.1, a)).

The x-ray reflectivity from an interface is determined by an electron density profile $\rho(z)$ between two media of electron densities ρ_1 and ρ_2 and is in the semi-kinematic approximation given by eq. (6.1) [119, 120].

$$R(Q_z) = R_F(Q_z) |\phi(Q_z)|^2 = R_F(Q_z) \left| \frac{1}{\Delta\rho_{12}} \int \frac{\partial\rho(z)}{\partial z} e^{iQ_z z} dz \right|^2 \quad (6.1)$$

R_F is the Fresnel reflectivity of an ideal (sharp) interface between the two media, $\Delta\rho_{12}$ the density contrast between them. If absorption effects are neglected, $R_F(Q_z)$ can be rewritten as a function of a critical momentum transfer Q_c , which corresponds to a critical angle α_c , at which total reflection of the x-ray beam occurs on an ideal smooth surface. Both quantities directly depend on the density contrast between the two media via $Q_c = \frac{4\pi}{\lambda} \cdot \sin \alpha_c \cong 4\sqrt{\pi r_0 \Delta\rho_{12}}$, where r_0 is the classical electron radius. Medium 1 is in this case water, medium 2 corresponds to the solid silicon substrate. It can be shown that for $Q_z \gg Q_c$ the Fresnel reflectivity $R_F(Q_z)$ decreases with Q_z^{-4} . The multilamellar bilayer stack is modelled by an interface with a partially oscillatory density profile [121]. Expression 6.1 implicitly consist of two parts, of which one regards the density increment at the substrate, and the other exclusively describes the bilayer stack. The latter is a product of the form factor $f(Q_z)$ and the

structure factor $s(Q_z)$ which are denoted in eq. (6.2).

$$\begin{aligned} s(Q_z) &= \sum_{n=1}^N e^{i(nQ_z D_z)} \\ f(Q_z) &= \int_{-D_z/2}^{D_z/2} \frac{\partial \rho(z)}{\partial z} e^{iQ_z z} dz \end{aligned} \quad (6.2)$$

The form factor is characteristic of the electron density distribution. The corresponding electron density profile of the bilayer is commonly parametrized in terms of its Fourier coefficients eq. (6.3).

$$\rho(z) = \sum_{n=1}^N v_n f_n \cos\left(\frac{2\pi n z}{D_z}\right) \quad (6.3)$$

Due to the mirror plane symmetry of the bilayer the phase coefficients, the v_n are reduced to ± 1 . After applying a (Lorentz) correction factor of Q_z^{-1} to the raw data [122, 123], the coefficients f_n can in a suitable approximation be related to the integrated peak intensities by $f_n \propto \sqrt{n I_n}$ [100, 121]. Therefore the electron density of the bilayer lipid membrane can be derived from the measured intensities according to eq. (6.4).

$$\rho(z) = \sum_{n=1}^N \sqrt{n I_n} v_n \cos\left(\frac{2\pi n z}{D_z}\right) \quad (6.4)$$

6.1.1 Sample Preparation and Environment

The phospholipid DMPC was purchased from Avanti (Alabaster, AL), dissolved in Chloroform/TFE (1:1) and spread on 600 μm thick rectangular silicon wafers (10 mm x 15 mm). The solvent evaporated over the course of two days in a vacuum oven at a temperature of 35°C. The samples were put in a freezer for ca. 12 h, before being defrosted at room temperature. The experiments were performed on a commercial AXS D8 Advance diffractometer (Bruker). The instrument is optimized for reflectivity measurements on liquid surfaces through a Göbel mirror which yields an intense parallel x-ray beam (Mo, K_α , $E=17.48$ meV), as well as the θ/θ goniometer which ensures a horizontal position of the sample at all times. To be able to measure reflectivities in a liquid water/Ethanol environment, the samples were inserted into a liquid cell consisting of teflon with windows made of Kapton foil. The solutions were added through one of two pinholes and extracted through the other with a pipette. All measurements were performed at a constant temperature of 30°C. The

temperatures was achieved through a temperature block consisting of an aluminum frame with Kapton windows that was hollow on the inside so it could be flooded through a standard water bath (Julabo). The liquid cell was inserted into this block (Fig. 6.1, b)).

Reference measurements were performed on silicon wafers with DMPC-multilayers immersed in Millipore water (double distilled, deionized) at 30°C. A D_z -spacing of 62.8 Å was obtained. For dry DMPC samples, the D_z -spacing at the same temperature lay at 54.4 Å. The mixing of water and Ethanol in various concentrations was automated through a pump (Jasco: HPLC PU-2080), which was connected to the white liquid cell shown in Fig. 6.1, b).

In order to study the influence of osmotic pressure on the phospholipid/Ethanol membrane, the long chain polymer PEG 20000 (Polyethylenglycol, Fluka), which is well soluble in water, was added in varying concentrations. Due to its size the polymer is unable to diffuse into the water layers in between single bilayers. This causes a pressure gradient between the outer and the inner part of the membrane, which in turn causes the bilayer repeat spacing to decrease until a new equilibrium is reached. Therefore, the osmotic pressure induced can be regarded as an additional attractive potential $V(d_w) = \Pi_{osm} \cdot d_w$ (cf. 2.8), which one can systematically vary through the concentration of the long chain polymer in water.

6.1.2 Effect of Ethanol concentration

Due to its distinct solubility with respect to water and the phospholipid, changes in Ethanol-concentration are directly reflected in changes in the inter-bilayer forces which determine the lamellar repeat spacing D_z . Fig. 6.2 shows reflectivity-scans for a DMPC membrane in water/Ethanol at 30°C for various alcohol concentrations. The curves are shifted vertically for clarity, a reference curve for DMPC in pure water is added (blue curve). The reflectivity is plotted as a function of momentum transfer Q_z after subtraction of the diffuse scattering (offset scan) and after illumination correction and show features typical of highly oriented multilamellar films: a plateau of total reflection at small Q_z , followed by sharp and intense Bragg-peaks towards larger Q_z . Commonly oriented samples are investigated in water-vapor environment, where stable humidities of up to 99Rh% are reached, e. g. reported in [100, 124]. In this case however, the oriented membranes were immersed in a liquid environment (100Rh%), since the bilayer repeat spacing D_z is determined by a balance of attractive and repulsive inter-bilayer forces, and therefore strongly depends on sample humidity.

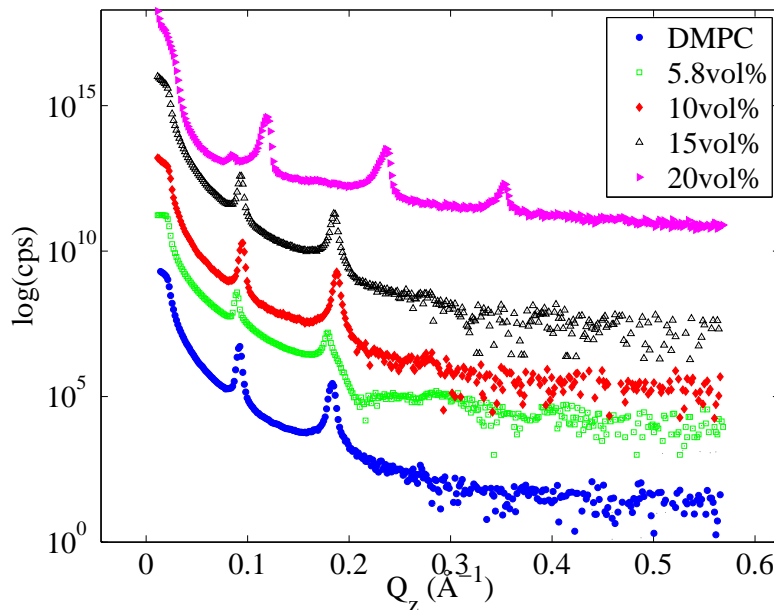


Figure 6.2: Reflectivity-scans of DMPC in water/Ethanol with increasing alcohol amount, at 30°C.

x_{Eth} (vol%)	0	5.8	10	15	20
D_z (Å)	62.84	65.18/64.5	61.24	62.4	48.93

Table 6.1: Bilayer repeat spacing D_z for DMPC membranes immersed in water/Ethanol solutions at 30°C for varying alcohol concentrations.

Two tendencies are observed, the more alcohol is added (Fig. 6.2): for low concentrations up to 5.8vol%, the membrane swells in D_z compared to the pure DMPC/water reference, for higher concentrations it exhibits a decrease in the lamellar repeat spacing. For 10vol% and 15vol% this decrease in D_z can be attributed to partial and for 20vol% to full interdigitation of the lipid acyl chains (cf. Table 6.1, [58]).

To further evaluate the data, the Fourier synthesis method, where solely the integrated peak intensities contribute to the electron density profile $\rho(z)$ is occasionally employed. The alternative to this method is a full Q_z -range fit of the data curves [121, 124], which yields density profiles in absolute units. The underlying model function must take into account effects of absorption, thermal fluctuations, static defects and instrumental resolution, not all of which are known here. The two methods are compared in Li et al. [125]. If the phase problem can be solved unambiguously, the simplified approach of Fourier synthesis can be used to extract the more crude structural properties, such as changes in distance between the phospholipid head

groups (two maxima in the density profiles correspond to the phosphorus atoms). It is then possible to determine the changes in the thickness of the water layer d_w in between the lipid layers, as well as of the hydrocarbon double layer according to: $a = D_z - d_w - d_k$ (Fig. 2.8).

However, since for most Ethanol concentrations only two Bragg peaks are visible, the phase problem cannot be solved unambiguously and therefore electron density profiles $\rho(z)$ cannot serve to identify distinct phases within or near the coexistence regime of the phase diagram (cf. Fig. 2.14).

For 20vol% Ethanol comparison of the bilayer repeat spacing D_z with literature values obtained for DPPC (cf. 2.3.3) suggests that the fully interdigitated phase, where the membrane bilayer structure is replaced by one with alternately partially overlapping lipid acyl chains separated by Ethanol molecules, is observed. For a naturally occurring membrane this kind of structural arrangement could have two interesting implications: On the one hand the membrane interface with the water layer increases due to an in-plane increase in headgroup distance as well as a decrease in the thickness of the hydrophobic carbon layer, which is bound to increase the membrane's permeability. On the other hand, collective fluctuations of the lipid acyl chains could be more restricted compared to the bilayer arrangement.

6.1.3 Unbinding of DMPC-bilayers

The unbinding of oriented DMPC-bilayers from the substrate was studied by reflectivity-scans for two distinct Ethanol concentrations. The small lamellar repeat spacing D_z obtained from curves of DMPC with 5.8vol% Ethanol (cf. Fig. 6.2, Table 6.1) indicates that the membrane was not fully immersed in liquid at the beginning of the measurements.

For 20vol% Ethanol, the bilayer decay occurs on a much shorter time scale than for 5.8vol% (Fig. 6.3). As for the lower concentration, the unbinding seems to be coupled to the insertion of Ethanol into the membrane. Both effects could be explained in a similar manner. In a state of full interdigitation, which only occurs at larger alcohol concentrations, the two types of amphiphilic molecules are arranged with respect to each other, so that both obtain a maximum exposure to the polar water layer. The bilayer structure consisting of two leaflets ceases to exist. This molecule arrangement is, however, extremely unstable for the lipids which are then particularly exposed to unbound Ethanol molecules. As soon as lipid molecules are dissolved from a single layer, the effect increases and an avalanche-effect which triggers further layer-decay is therefore likely to begin.

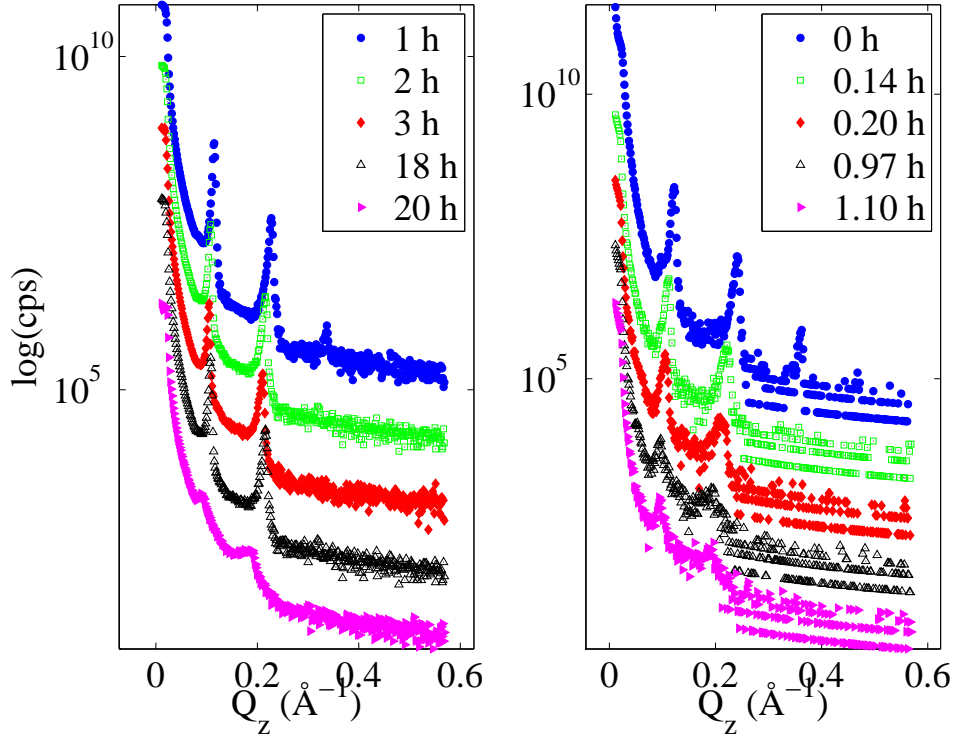


Figure 6.3: Unbinding of lipid layers without osmotic pressure observed in reflectivity-scans for DMPC immersed in liquid water/Ethanol: (*left*) 5.8vol%; (*right*) 20vol%, both at 30°C.

x_{Eth} (vol%)	time (h)	D_z (Å)	x_{Eth} (vol%)	time (h)	D_z (Å)
5.8	1	51.06	20	0	52.32
	2	53.54		0.14	56.27
	3	55.10		0.20	59.89
	18	62.82		0.97	65.20
	20	62.92		1.10	65.44

Table 6.2: Time-dependent bilayer repeat spacing D_z for unbinding of DMPC membranes immersed in 5.8 vol% water/Ethanol solutions at 30°C.

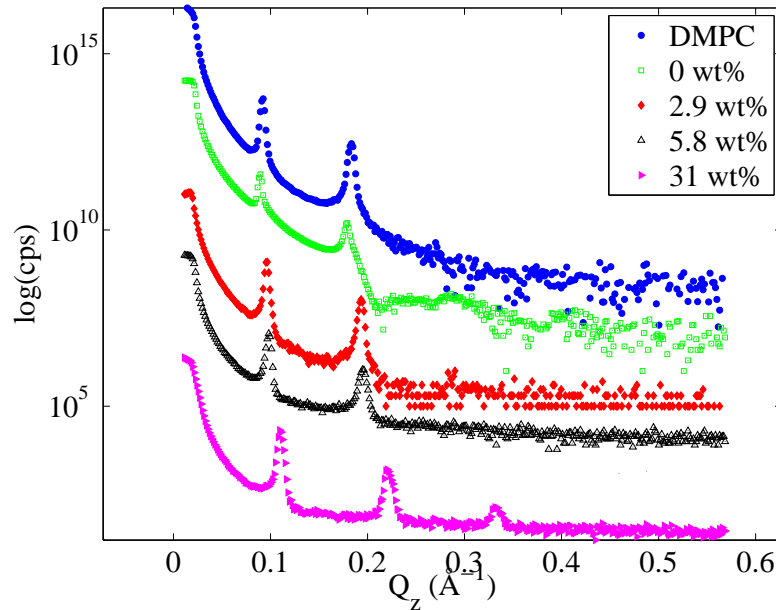


Figure 6.4: Influence of osmotic pressure on DMPC-layers immersed in liquid water/Ethanol (5.8vol%). The osmotic pressure increases with wt% of polymer osmolyte (PEG 20000) dissolved in liquid (cf. Table 6.3).

6.1.4 Influence of Osmotic Pressure

Finally, the influence of osmotic pressure on phospholipid membranes containing varying Ethanol concentrations is studied. Corresponding reflectivity curves for a concentration of 5.8vol% Ethanol are shown in Fig. 6.4. The overall lamellar repeat spacing D_z decreases with increasing pressure.

For the highest osmotic pressure of $\log P=7.23$ dynes/cm² (cf. Table 6.3), the reflectivity-curve strongly resembles the one obtained in the fully interdigitated phase at 20vol% Ethanol without osmotic pressure (Fig. 6.5, (*left*)). The data suggests, that inducing an osmotic pressure into a phospholipid membrane containing Ethanol not only influences the thickness of the water layer d_w , as for the pure phospholipid DMPC [19], but also evokes significant changes in the acyl chain ordering and thus in the respective attractive van der Waals forces (cf. 2.2.4).

The function of a given anesthetic, such as Ethanol, is based on inducing a lateral pressure on the membrane at defined concentrations (cf. 2.3.3). The data presented indicates that inducing an osmotic pressure along the bilayer normal enhances this effect and forces a significant reorganization of lipid molecules into the fully interdigitated phase at a comparably low Ethanol concentration. In fact, the opposite effect is observed in an air-plane, where anesthetics are known to have less effect.

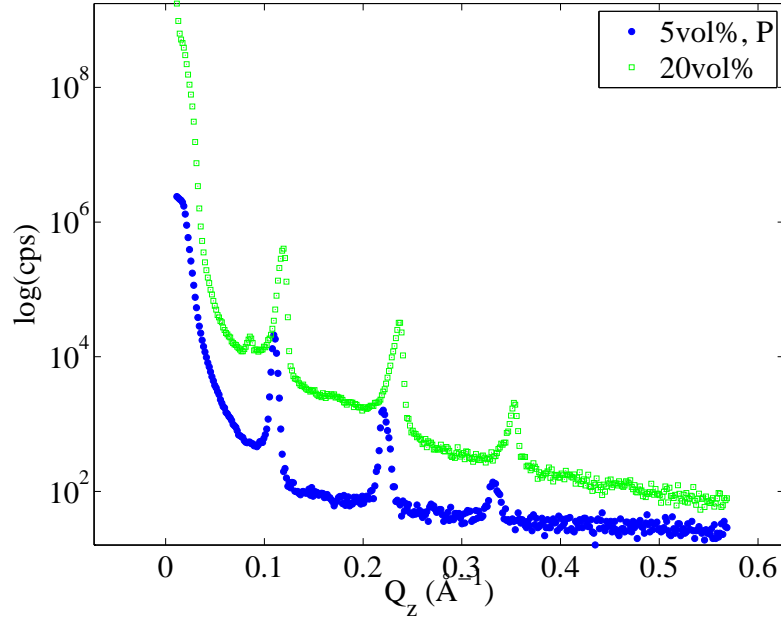


Figure 6.5: Reflectivity-scans in interdigitated phase: for DMPC membrane with 5vol% Ethanol under an osmotic pressure of $\log P=7.23$ dynes/cm², DMPC membrane with 20vol% Ethanol without osmotic pressure.

x_{Eth} (vol%)	x_p (wt%)	$\log P$ (dynes/cm ²)	D_z (Å)
0	0	1.57	62.84
5.8	0	1.57	65.18
	2.9	4.98	59.97
	5.8	5.55	55.94
	31	7.23	51.80
10	0	1.57	61.24
	2.9	4.98	60.25
	5.8	5.55	57.35

Table 6.3: Bilayer repeat spacing D_z of DMPC membranes immersed in water/Ethanol solutions at varying osmotic pressures.

6.2 Neutron Scattering

To study the effect of the short-chain alcohol Ethanol on the collective in-plane density fluctuations observed for the phospholipid acyl chains of single lipid membranes (cf. chapter 4), inelastic energy-scans were taken at distinct points around the DMPC-d54 dispersion minimum on IN12 (ILL, Grenoble). Structural changes within the semi-stable sample were monitored by measuring the in-plane static structure factor $S(Q_r)$ and taking repeated reflectivities $S(Q_z)$ between the inelastic scans throughout the experiment.

Changes in the bilayer repeat spacing D_z are related to the previously presented x-ray reflectivity study on the Ethanol-induced unbinding of phospholipid layers and the influence of osmotic pressure on the composite model system.

6.2.1 Sample Preparation and Experiment

As for previously presented neutron experiments a DMPC-d54 'sandwich sample' (cf. 4.2.1) was prepared and carefully inserted into a vacuum sealable aluminum container specially built to fit into a standard orange cryostat. To reduce incoherent inelastic scattering contributions, the sample was immersed into a mixture of 5vol% deuterated Ethanol-d6 (Merck) in D_2O . To prevent the phospholipid layers from washing off the substrate under the influence of the added alcohol, an osmotic pressure was added. This was achieved by giving the mixture into a solution of 2wt% PEG 20000 (and D_2O). The liquid containing water, Ethanol and the polymer osmolyte was then carefully inserted into the aluminum container with a pipette (cf. photo, Fig. 6.6). The temperature to a constant temperature of 30°C was realized by a standard orange cryostat.

Inelastic scans were taken at constant k_f 's of 1.25 \AA^{-1} and 1.75 \AA^{-1} , respectively. Two different scattering geometries were again employed: along the layer normal Q_z (neutron reflectivity scans) and in the plane of the membrane Q_r (chain peak, inelastic scans).

The neutron (diffraction) results shown in the following differ from the ones obtained from a composite phospholipid/Cholesterol membrane (cf. 5.2), presented in the previous chapter, in two ways: First, both major components of the membrane, DMPC-d54 and D_2O /Ethanol-d6 are deuterated (no selective highlighting). Second, the incoherent scattering contribution is larger because the sample is immersed in a liquid instead of in D_2O -vapor. The majority of incoherent scatterers is located in the polymer osmolyte used to stabilize the sample (cf. 6.1.4). Note that the reduction of incoherent scattering is essential for the observation of the collective



Figure 6.6: Photo of sample-assembly: the sandwich-sample visible in the background is inserted into the aluminum container visible up front. Then the liquid mixture containing 2 wt% PEG 20000 solved in D_2O as well as deuterated Ethanol d-6 is carefully pipetted inside. The container lid is sealed at the top with indium wire and eight screws.

in-plane density fluctuations of the phospholipid acyl chains. In contrast to the previously discussed x-ray experiments, the wafers containing the lipid multilayers were not placed horizontally, but vertically in order to meet the neutron beam. In addition to the decay caused by gravity, the sample tray moves during inelastic scans, in order to adjust the sample position with respect to the changing incoming and outgoing neutron beams (cf. 3.3.1). Therefore bilayer stabilization and reduction of incoherent scattering are two conflicting priorities.

6.2.2 Neutron Diffraction: In-plane and Bilayer Ordering

Several distinct scattering contributions can be identified in measurements of the elastic in-plane structure factor $S(Q_r)$, of which the acyl chain correlation peak located between 1.2 \AA^{-1} and 1.5 \AA^{-1} is the weakest. Towards smaller Q_r , a dominant incoherent scattering contribution appears (priv. comm.: M. C. Rheinstädter), towards higher Q_r a part of the slope of the water peak located at 2.0 \AA^{-1} appears, but is cut off at 1.8 \AA^{-1} by the sample container. Note, that the data shown was collected within the first two days of the experiment, where the bilayer decay was minimal.

Between each set of in-plane measurements regular reflectivity scans were taken in the perpendicular geometry. On the one hand, this was done with the aim of characterizing the sample in terms of a change in the lamellar D_z -spacing caused by

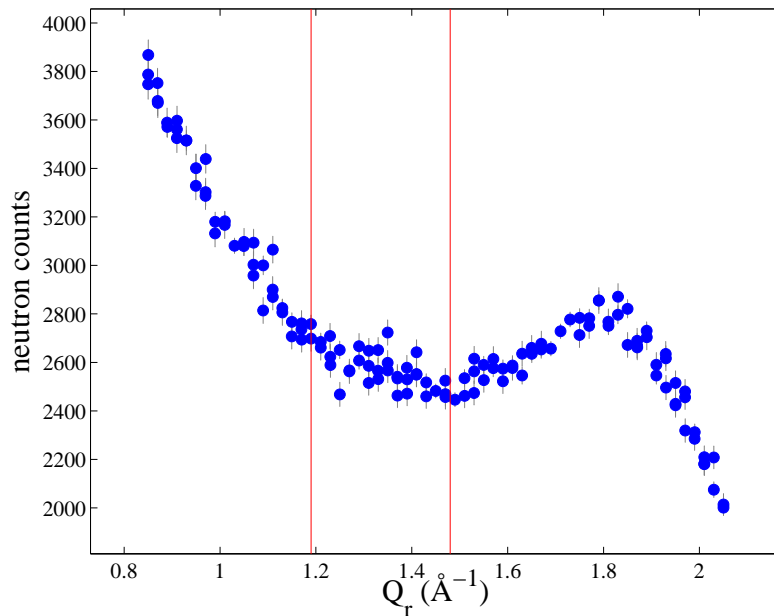


Figure 6.7: Elastic in-plane structure factor $S(Q_r)$: below 1.2 \AA^{-1} , a dominant incoherent scattering contribution is observed, between 1.2 and 1.5 \AA^{-1} a weak intensity increase due to the acyl chain correlation and above 1.5 \AA^{-1} a the water peak centered at 2.0 \AA^{-1} that is cut off at large angles by the sample container.

Ethanol moving into the membrane. On the other hand, the sample decay occurring throughout the experiment was monitored and recorded (Fig. 6.9).

Fig. 6.8 shows typical scans taken throughout the experiment. The data was corrected for an angular offset due to the asymmetry of the sample container along the direction of the layer normal (sample is turned around an axis in container lid, cf. photo, Fig. 6.6). A decrease in the peak intensity with time as well as a shift of the respective peak positions towards larger Q_z are clearly visible. The change in the repeat spacing D_z throughout the course of the experiment is determined from fits of the curves with multiple Gaussians, taking into account a Q_z^{-4} intensity decrease at low Q_z . From these fits, the area under the second peak was normalized with respect to the area obtained at the beginning of the experiment (cf. Appendix B.3.2). An exponential decay for the area under the peak according to $A = A_0 \cdot e^{-t/\tau}$ was observed with a decay time of $\tau = 24.6 \text{ h}$. Note, that the experiment lasted for nine days.

The previously presented x-ray reflectivity study shows that the Ethanol-induced DMPC-bilayer decay exhibits a time-dependent increase in D_z (Fig. 6.3), which is not observed with neutrons for a phospholipid/Ethanol membrane under osmotic pressure and on a significantly larger time scale. In fact the time-dependent decrease

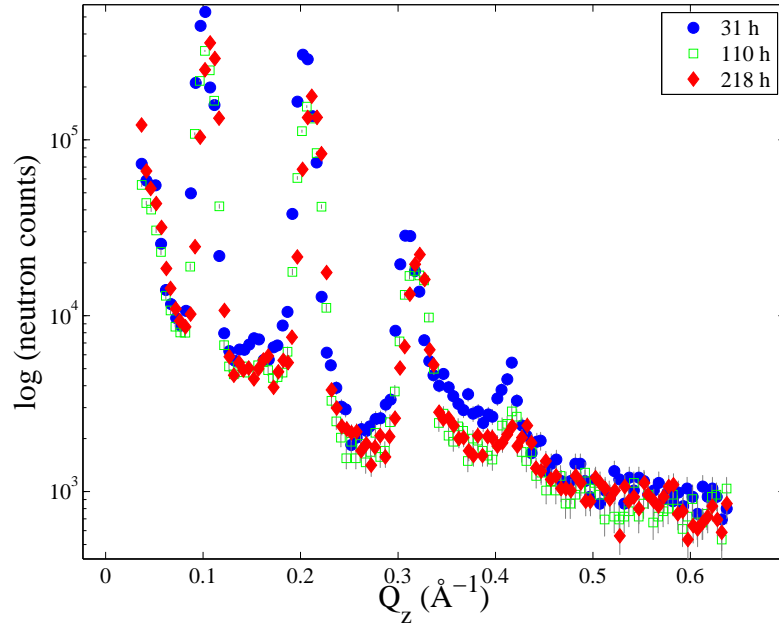


Figure 6.8: Reflectivity-scans taken to monitor time-dependent layer-decay (cf. Fig. 6.9). The data was corrected for an angular offset due to asymmetry of aluminum sample container along layer normal axis (cf. photo, Fig. 6.6).

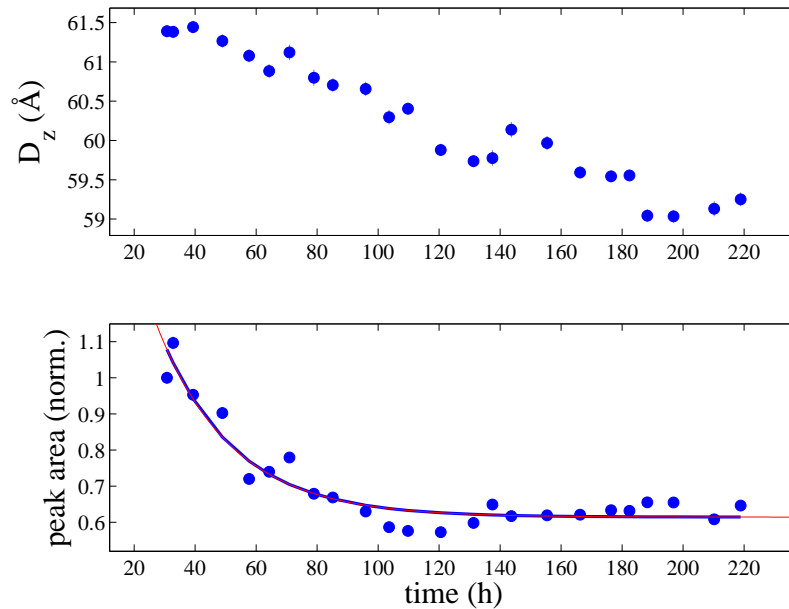


Figure 6.9: (*top*) Time-dependent change in layer repeat spacing D_z throughout experiment obtained from fits of reflectivity-scans. (*bottom*) Time-dependent decay of area under 2. order Bragg-peak obtained from normalized integrated intensity. The solid line corresponds to the fit of an exponential decay.

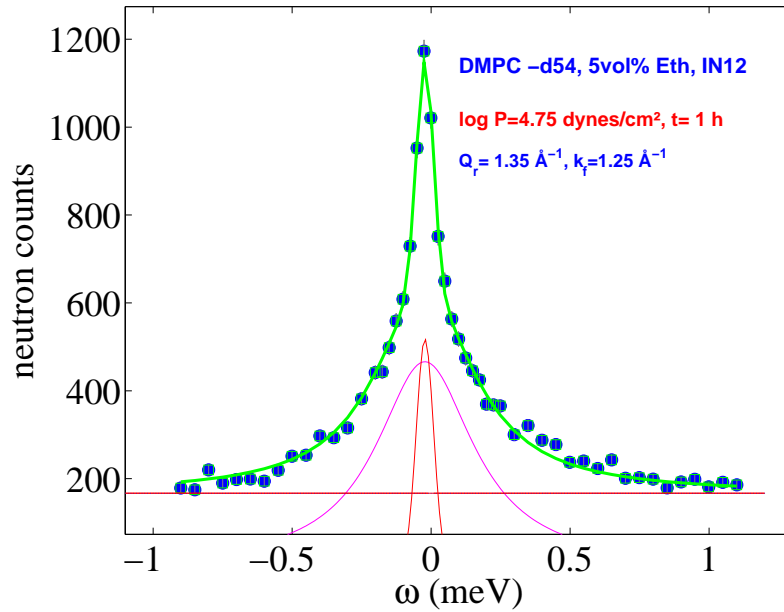


Figure 6.10: Inelastic energy-scan taken at $Q_r = 1.35 \text{ \AA}^{-1}$ at the beginning of the experiment ($t=1 \text{ h}$) for 5vol% Ethanol under an osmotic pressure of $\log P = 4.75 \text{ dynes/cm}^2$. The data was fitted by a sum of a Gaussian for instrumental resolution (red), a Lorentzian for the quasielastic contribution (magenta) and a constant background (red line). No coherent inelastic excitation was found. The overall fit is indicated by the green line.

in the lamellar repeat spacing (Fig. 6.9, (*top*)) could indicate that continuously more Ethanol moves inside the membrane and thereby induces a (partial) interdigitation, possibly due to a higher effective Ethanol concentration in the oriented membranes after layer decay.

6.2.3 Influence of Ethanol on Collective In-plane Chain Dynamics

Overall, the structural analysis already indicates that both incoherent scattering as well as sample decay pose serious limitations to the observability of the collective in-plane density fluctuations of the phospholipid acyl chains under the influence of Ethanol.

Fig. 6.10 shows an example of an inelastic energy scan taken at the very beginning of the experiment, after absorption and detailed balance corrections have been applied (cf. 3.3.4). The fit consists of a Gaussian for instrumental resolution which is fixed in width around the elastic line, a Lorentzian for the quasielastic contribution (diffusional processes), as well as a constant background. Inelastic excitations representing coherent dynamical processes as observed in single lipid membranes or the previously discussed composite membrane of DMPC/Cholesterol were not

found. The reasons for this are mainly of a technical nature and related to the diminishing effective coherent scattering volume due to the sample decay and to the dominant overall incoherent scattering. However, the significant decrease observed in the lamellar repeat spacing D_z indicates that the interdigitated $L_{\beta_i'}$ -phase is at least partially induced. Therefore it is not imminent that the collective chain motions themselves are not at least partially suppressed in this specific phase, due to mutual steric hindrance of the lipid acyl chains. In fact, it could be a distinct mechanism for the biochemical function of the anesthetic to block the in-plane propagation of a signal in a membrane.

6.3 Summary and Outlook

At the investigated Ethanol concentrations DMPC samples of multiple bilayers oriented on silicon wafers (≈ 1000 layers per wafer) exhibit a high degree of instability with a certain statistical weight. For all measured Ethanol concentrations characteristic D_z -spacings could be extracted, from which it was possible to deduce the membrane state to either the lipid fluid phase or (partially) interdigitated phases. In addition to its continuous decay, the neutron sample exhibited strong incoherent scattering contributions. Therefore no coherent inelastic excitations could be observed. In order to stabilize the sample further and thus make the observation of these excitations more likely, a larger concentration of the polymer osmolyte PEG 20000 would have to be used in a deuterated version. Possibly, a higher neutron flux than presently available would be necessary to ensure successful measurement of excitations in the liquid environment, so that they can be distinguished from background and quasielastic scattering contributions.

Further x-ray reflectivity studies seem more practical, however: the liquid chamber with the temperature unit, the water bath and the pump to mix water and Ethanol in varying distinct ratios can easily be transferred to a synchrotron source, where it should be possible to obtain Bragg peaks at least up to the fourth order. Full Q_z -range fits as described in [121, 124, 125] would yield electron density profiles $\rho(z)$ in absolute units and allow a precise analysis of the structural changes induced by varying alcohol concentrations as well as osmotic pressures. Calculation of the underlying contributions to the respective van der Waals and hydration potentials seem possible and would most likely contribute to a unique quantitative understanding of the function of Ethanol in a phospholipid membrane, both as an anesthetic and as a drug enhancer.

Chapter 7

Summary

In the present study the structure and collective short wavelength dynamics of composite phospholipid model membranes have been investigated.

Before an extension to multi-component membranes, the first part of this thesis addressed the comparison of two lipid membranes, each containing a single component, namely DMPC and DSPC. To this end, each system was characterized by x-ray diffraction (4.1.2). The temperature-dependent structural changes in the nearest neighbor distances of lipid molecules in the membrane plane were probed by wide-angle scattering, while the temperature-dependent bilayer stacking was probed by small-angle scattering. Significantly, differences in the temperature-dependent in-plane chain correlation length have been observed. The chain correlation length was obtained from Lorentzian fits of the acyl chain correlation peak, according to $\xi_r(T) = 1/\text{HWHM}$ [126]. The results differed by an order of magnitude for the two single lipid membranes in all phases (Fig. 4.7, 4.12). Both x-ray and neutron diffraction showed a continuous shift of the peak for the short chain lipid DMPC with temperature, while a coexistence of peaks around the main phase transition was observed for the long chain lipid DSPC. Thus, the first system, DMPC, shows the so-called anomalous effect, similar to a second order phase transition. The second system, DSPC, shows phase coexistence typical for first order transitions and no anomalous swelling effect. These differences can hypothetically be linked to the formation of domains of lipids in each of the respective phases with considerably different sizes in DMPC and DSPC. Such arguments must carefully weigh the effect of three length scales on the observed lineshapes, namely: (i) the chain correlation length, (ii) the domain size (in the case of phase coexistence), (iii) the coherence length of the probe.

Here, we have extended both the elastic results, and for the first time present a comparison including results from inelastic scattering. To this end, the coherent

scattering contribution had to be enhanced over the dominant incoherent scattering contribution. This was achieved using highly oriented multilamellar membrane stacks with a total mass of 400 mg of chain-deuterated lipids. As the excitations observed are broad and strongly damped, large counting times in the order of half of a day for an energy-scan, which sufficiently covers the elastic line, were necessary to distinguish the inelastic contribution from quasielastic and background contributions. Instrumental resolution properties (3.3.3) had to be taken into account in order to analyze the data. Finally, distinct points of a dispersion relation were obtained for DSPC, which suggested a characteristic minimum (*de-Gennes narrowing*) [85]. However, the uncertainty in the data is higher than in DMPC due to the higher aluminium background scattering contribution. Also, the inelastic excitations occur at much lower energy-values, closer to the quasi-elastic scattering contributions from which they have to be distinguished. The significantly larger in-plane correlation length obtained for DSPC, however, seems to correspond to a more pronounced narrowing.

In the second part of the thesis, we have investigated a composite membrane of DMPC/Cholesterol in terms of the characteristic nature of its inelastic excitations. Again, detailed knowledge of the structure and the structural changes with temperature and concentration is a prerequisite. The corresponding information obtained from small- and wide-angle x-ray scattering (5.1) shed light on the in-plane nearest chain packing and the corresponding bilayer stacking of phospholipid and sterol molecules in different regions of the phase diagram (Fig. 5.17). A qualitative agreement with previously published phase diagrams was observed [37, 42].

Do to the amphiphilic nature of the phospholipid and the pronounced hydrophobicity of Cholesterol, both types of molecules arrange in close proximity with respect to each other throughout the phase diagram, in order to avoid the energetically unfavorable exposure of the sterol to interbilayer water. According to [45], the hydrophobicity of the Cholesterol molecule determines the observed concentration-dependent phase behavior, while motional degrees of freedom of the sterol molecule within the membrane determine the temperature-dependent phase behavior [6]. This matches our observations, where, apart from a dominant main phase transition, phase barriers are crossed gradually, domains of lipids in one specific phase are not formed.

In the physiologically relevant liquid-ordered L_o -phase the lamellar ordering is significantly higher than in the other phases with lower Cholesterol concentration, reflecting an increase in the bending rigidity κ_B . On a molecular level, this can be explained by a straightening effect, which the rigid part of the sterol molecule has on the lipid acyl chains.

This phase was chosen for the study of the collective in-plane density fluctuations. For comparison, we also measured in the so-called liquid disordered L_d -phase, which occurs at significantly lower Cholesterol concentrations. The samples consisted of partially deuterated phospholipids, but protonated sterol. Correspondingly, the collective dynamics of the lipid acyl chains under the influence of Cholesterol were observed. In other words, there was no coherent scattering contribution from the sterol molecules themselves. Due to the selective highlighting of molecules, the phase-dependent neutron diffraction measurements of the acyl chain correlation peak on the same samples complemented the previously obtained x-ray diffraction data. Surprisingly, the distance of lipid molecules in the membrane plane, as well as the correlation length ξ_r are quite similar for the two liquid phases. Simultaneously measured neutron reflectivity-scans indicated significant changes in the bilayer ordering (Fig. 5.19), which qualitatively matched previously obtained concentration-dependent SAXS-scans.

The appearance of two strong and sharp excitations of a well-defined long lifetime observed in the inelastic neutron energy-scans does not correspond to the typical liquid behavior observed in single lipid membranes. Within the fit error, position and width of the excitations do not depend on the Cholesterol concentration (Fig. 5.23-5.26). For certain specific Q_r , excitations in the inelastic energy-scans are equally suppressed in both phases (Fig. 5.25), which could suggest an underlying mechanism of mode selection. The strongest (inelastic) scattering contribution in constant-energy and energy scans, likewise, is observed for all energies around the position of the acyl chain correlation peak (Fig. 5.20, 5.24, 5.21, 5.22).

The sharpness and intensity of energy excitations representing the collective density fluctuations is rather surprising for a liquid. A typical liquid dispersion relation with a minimum at the nearest neighbor position as found for single lipid membranes, was not obtained. Due to the complexity of the composite model system, however, neither the theory of de Gennes, nor the effective eigenmode model, which originate in the description of classical mono-atomic liquids, can be applied.

Structural results suggest that the bilayer stacking observed in the two liquid phases is to a large degree decoupled from the in-plane nearest neighbor arrangement of lipid molecules, as well as from the corresponding collective dynamics of lipid acyl chains: Neutron reflectivity-scans on the one hand show significant differences in the bilayer ordering in the two phases. The acyl chain correlation peaks, on the other hand, resemble each other in terms of position and width. The two dispersive and paired excitations also occur at the same energies in both phases, as does the high frequency excitation (Fig. 5.27) that was linked to a non-dispersive optical mode

first predicted for the pure lipid membrane by Tarek et al [80].

The results seem to suggest, that the approach to model the lipid chains as (two-dimensional) liquid crystals in single component membranes, can be extended to a composite DMPC/Cholesterol membrane only with significant restrictions. Since no domain formation was observed, the origin of the two paired excitations must be found in a modulation of the propagating in-plane density fluctuations that originates on a molecular scale. Here, the rigid part of the sterol molecule is believed to play a key role: If it adds a slight disturbance to the collective motion of a fraction of the lipid chains, this could evoke a second distinct modulation of the propagating sonic wave, visible in the pairing of excitations.

In the last part of this thesis, a composite model membrane containing the short chain alcohol Ethanol has been studied to shed light on the molecule's function as a drug enhancer and anesthetic. The structural characterization of the DMPC/Ethanol system by x-ray reflectivity for the first time demonstrated the possibility of investigating oriented phospholipid/alcohol-samples in a liquid environment. Specifically, the so-called 'interdigitated' $L_{\beta_i'}$ -phase, which is unique to this particular kind of membrane, was identified (Fig. 6.5).

In order to investigate the corresponding collective in-plane fluctuations of the lipid chains, it turned out that two major technical challenges had to be met: i) the instability of the oriented lipid layers under the alcohol influence, ii) compared to previously employed samples immersed in vapor, an increased incoherent background due to the liquid environment.

Over the course of the reported inelastic neutron scattering experiment, the sample exhibited a continuous decay in the number of bound and aligned bilayers (Fig. 6.9), similar to what was seen before by x-ray reflectivity experiment. Along with the loss of sample volume, the lamellar repeat spacing D_z decreased gradually over the course of 200 h measurement time. The decrease indicates a slow transformation to the interdigitated $L_{\beta_i'}$ -phase with time. Note, that interdigitation of the lipid acyl chains is likely to hinder their collective motion. Therefore, the observed absence of coherent inelastic excitations in the data, could not only be related to the mentioned technical limitations, but also be an intrinsic feature of the lipid/Ethanol/water system.

Appendix A

X-ray Experiments

A.1 WENDI-macros (SPEC)

A.1.1 SAXS- and WAXS-scans combined

DMPC/Cholesterol (95:05) 200 mg/ml capillaries

Julabo control by spec

#chamber connected

mv tth 1 attoff mv f 1

mv ys 12.25

#-----

mv jt1 15

ascan dummy -1 1 90 60

p julabo_gettemppt100(0)

#SAXS

mv s1hg 0.1 mv

s2hg 0.4 mv

s3hg 0.2

mv tth 0.4

ascan tth 0.4 6.4 500 30

pjulabo_gettemppt100(0)

#WAXS

mv s1hg 0.5

mv s2hg 1

mv s3hg 1

mv tth 14

```

ascan tth 14 25 100 120
p julabo_gettemppt100(0)
  #-----
  mv jt1 30
ascan dummy -1 1 90 60
p julabo_gettemppt100(0)
  #SAXS
mv s1hg 0.1
mv s2 hg 0.4
mv s3hg 0.2
  mv tth 0.4
ascan tth 0.4 6.4 500 30
p julabo_gettemppt100(0)
  #WAXS
mv s1hg 0.5
mv s2hg 1
mv s3hg 1
  mv tth 14
ascan tth 14 25 100 120
p julabo_gettemppt100(0)

```

A.1.2 temperature ramp

```

# DMPC/Cholesterol (95:05) 200 mg/ml capillaries
# Julabo control by spec
#chamber connected
  mv tth 1 attoff mv f 1
  mv ys 12.25 mv th 0 #-----
  # Start bei ca. 61
#mv jt1 60
p julabo_gettemppt100(0)
  #SAXS
mv s1hg 0.1
mv s2hg 0.4
mv s3hg 0.2 mv
tth 0.7
  ascan tth 0.7 1.8 80 10

```



```

ascan tth 0.7 1.8 80 10
p julabo_gettemppt100(0)
mv jt1 61

```

A.2 Data Treatment: Matlab

A.2.1 3d-plots

```

T=[10 15 20 21 22 22.5 23 23.5 24 24.5 25 25.5 26 27 28 30 32 35 40 45 55];
Drampe0=loads('specbatch','Cap1,X=Two Theta,Y=Detector,M=Monitor,S=[82 86
99 103 106 109 112 115 118 127 130 133 136 139 157 145 148 159 161 73 70]');

```

```

%2Theta in q umrechnen
for n=1:length(Drampe0)
tth=getfield(Drampe0(n),'x');
Drampe0(n)=setfield(Drampe0(n),'x',4*pi/1.5418*sin(tth/180*pi/2));
Drampe0(n)=cut(Drampe0(n),[0.05 0.13]); end;
clf;
mapplot(cut(Drampe0,[0.05,0.128]),T,0.00001,[10:0.5:55],[0.05:0.001:0.128],'log');
title('DMPC, 10-55°C','interp','tex','fontsize',[20]);
xlabel('T (°C)','interp','tex','fontsize',[24]);
ylabel('Qz (Å-1)','interp','tex','fontsize',[24]);
shading flat;

colorbar;
grid('off');

set(gca, 'fontsize',[24]);
colormap(jet)

print -depsc Rampe0.eps

```

A.2.2 Evaluation of Temperature Ramps

```

for ncount=1:length(Drampe40)
    %Peakposition
    [fitDrampe40(ncount),fitDrampe40data(ncount)]=
fits(cut(Drampe40(ncount),[0.11 0.06]),'strline',[1.193e-01 4.6531e-02],[1 1]);

    %gibtFitparameter aus
    [fitDrampe40data(ncount).pvals(1) fitDrampe40data(ncount).pvals(2)]
    [fitDrampe40data(ncount).evals(1) fitDrampe40data(ncount).evals(2)]
    line(x,x*fitDrampe40data(ncount).pvals(1)+fitDrampe40data(ncount).pvals(2),'color','red');

    [x0,y0,e0]=extract(Drampe40(ncount)-fitDrampe40(ncount))

    s=[x0,y0,e0]

    %sucht in der 2. Spalte der Matrix das Maximum und gibt den Zeilenindex I aus
    [C,I]=max(s(:,2),[],1)
    s(I) %Peakposition

    y02=abs(s(:,2)-0.5*C)
    s2=[x0,y02,e0]
    [s-s2]

    clf;
    plot(x0,y0)
    clf;
    plot(x0,y02)

    %gehe vom ersten Vektoreintrag bis zum Maximumsindex
    y03=y02(1:I)
    x03=x0(1:I)

    s3=[x03,y03]
    plot(x03,y03)

    %erster Nullpunkt

```

```

[B,H]=min(s3(:,2),[],1)
s3(H)

%gehe bis Maximum und schneide den Rest weg
y04=y02(I:length(y02))
x04=x0(I:length(x0))
s4=[x04,y04]
plot(x04,y04)

%zweiter Nullpunkt
[A,G]=min(s4(:,2),[],1)
s4(G)

[C s(I) s4(G)-s3(H)]

Drampe40amp(ncount)=C
Drampe40pos(ncount)=s(I)
Drampe40FWHM(ncount)=s4(G)-s3(H)

plot(Drampe40(ncount)-fitDrampe40(ncount))
%axis([0.05 0.13 0 0.075])
line([s(I) s(I)],[-0.5 1], 'color','green')
line([s3(H) s4(G)], [0.5*C 0.5*C], 'color','red')
line([s4(G) s4(G)], [-0.5 1], 'color','red')
line([s3(H) s3(H)], [-0.5 1], 'color','red')
pause;
end

```

A.2.3 Cuts through 3d-plots Shown

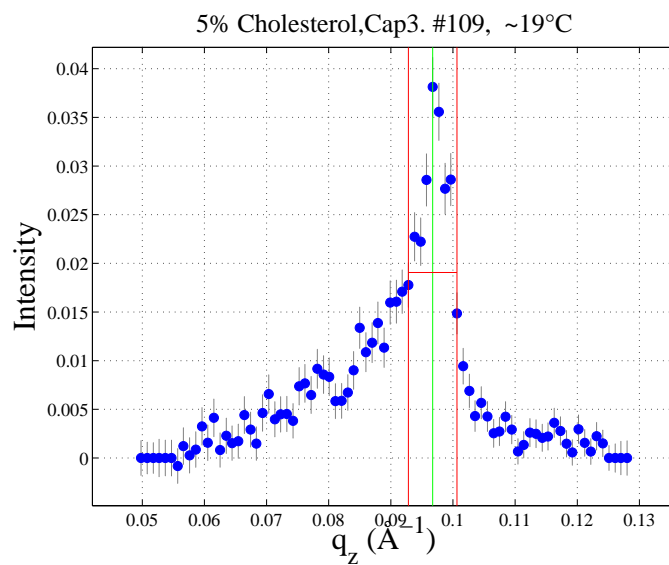


Figure A.1: Exemplary scan as obtained for WENDI temperature ramp.

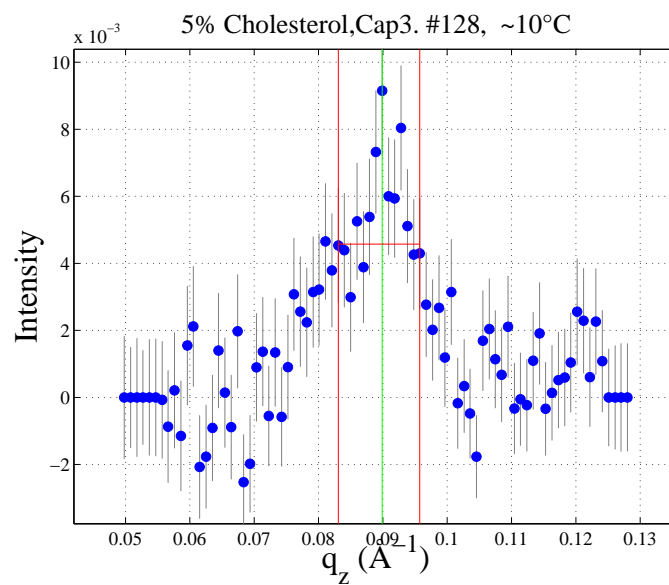


Figure A.2: Exemplary scan as obtained for WENDI temperature ramp.

A.2.4 DMPC/Cholesterol Phase diagram

```
% Phase diagram obtained for DMPC/Chol: SAXS temperature ramps, WAXS
%scans, ID02
    %solid S-phase
    TS0=[10 15];
concS0=[0 0];

    TS5=[10:0.41:16.5];
for i=1:length(TS5)
concS5(i)=5;
i=i+1;
end

    TS=[TS0 TS5];
concS=[concS0 concS5];
    tmp.x=concS;
tmp.y=TS;
tmp.e=0.00001*TS;
    solid=spec1d(tmp);
    clf;
h=plot(solid);
    pause;

    %ripple phase
    Tripple0=[15 20 21 22 22.5 23 23.5 24 24.5 25 25.5];
concripple0=[0 0 0 0 0 0 0 0 0 0];
    Tripple5=[16.5:0.41:21];
for i=1:length(Tripple5)
concripple5(i)=5;
i=i+1;
end

    Tripple=[Tripple0 Tripple5];
concripple=[concripple0 concripple5];
    tmp.x=concripple;
tmp.y=Tripple;
tmp.e=0.00001*Tripple;
```

```
    ripple=spec1d(tmp);
    clf;
h=plot(solid,ripple);
pause;
    %liquid disordered LD-phase
    Tld0=[25.5 26 27 28 30 32 35 40 45 55];
conclld0=[0 0 0 0 0 0 0 0 0];
    Tld5=[21:0.41:60];
for i=1:length(Tld5)
conclld5(i)=5;
i=i+1;
end
    Tld=[Tld0 Tld5];
conclld=[conclld0 conclld5];
    tmp.x=conclld;
tmp.y=Tld;
tmp.e=0.00001*Tld;
    ld=spec1d(tmp);
    clf;
h=plot(solid,ripple,ld);
pause;
    %coexistence solid, liquid-ordered phase
    Tslo12=[10:0.44:23];
for i=1:length(Tslo12)
concslo12(i)=12;
i=i+1;
end
    Tslo20=[10:0.45:22];
for i=1:length(Tslo20)
concslo20(i)=20;
i=i+1;
end
    Tslo=[Tslo12 Tslo20 15 15 21 21];
concslo=[concslo12 concslo20 39.5 40.5 4.5 5.5];
    tmp.x=concslo;
tmp.y=Tslo;
tmp.e=0.00001*Tslo;
```

```

    slo=spec1d(tmp);
    clf;
h=plot(solid,ripple,ld,slo);
pause;
    %coexistence liquid disordered, liquid-ordered phase
    Tldlo12=[23:0.44:48];
for i=1:length(Tldlo12)
conclldlo12(i)=12;
i=i+1;
end
    Tldlo20=[22:0.45:46];
for i=1:length(Tldlo20)
conclldlo20(i)=20;
i=i+1;
end
    Tldlo=[Tldlo12 Tldlo20 54.5 54.5];
conclldlo=[conclldlo12 conclldlo20 39.5 40.5];
    tmp.x=conclldlo;
tmp.y=Tldlo;
tmp.e=0.00001*Tldlo;
    ldlo=spec1d(tmp);
    clf;
h=plot(solid,ripple,ld,slo,ldlo); pause;
    %phase x
    Tx12=[48:0.44:60];
for i=1:length(Tx12)
concx12(i)=12;
i=i+1;
end
    Tx20=[46:0.45:60];
for i=1:length(Tx20)
concx20(i)=20;
i=i+1;
end
    Tx=[Tx12 Tx20 55.5 55.5];
concx=[concx12 concx20 39.5 40.5];
    tmp.x=concx;

```

```
tmp.y=Tx;
tmp.e=0.00001*Tx;
    x=spec1d(tmp);
    clf;
h=plot(solid,ripple,ld,slo,ldlo,x); pause;
    %phase y
    Ty=[65];
concy=[12];
    tmp.x=concy;
tmp.y=Ty;
tmp.e=0.00001*Ty;
    y=spec1d(tmp);
    clf;
h=plot(solid,ripple,ld,slo,ldlo,x,y);
pause;
    %liquid-ordered phase
    Tlo40=[10:0.5:60];
for i=1:length(Tlo40)
conclo40(i)=40;
i=i+1;
end
    tmp.x=conclo40;
tmp.y=Tlo40;
tmp.e=0.00001*Tlo40;
    lo40=spec1d(tmp);
    clf;
h=plot(solid,ripple,ld,slo,ldlo,x,lo40,y);
```

A.3 Osmotic Pressures induced by PEG 20000

An equation that fits this data is the following.

$$\log P = a + b * (\text{wt}\%)\hat{c}$$

where $a = 1.57$, $b = 2.75$ and $c = 0.21$

Note that it should be applied only over the range of pressures measured.

From: http://www.brocku.ca/researchers/peter_rand/osmotic/data/peg20000.

wt%	log P (dynes/cm ²)
1.5	4.59
2.9	4.98
3.6	5.15
4.7	5.34
5.8	5.55
6.3	5.63
7.1	5.76
9.0	5.89
12.1	6.08
13.1	6.18
14.2	6.29
16.0	6.47
18.3	6.70
19.0	6.8
20.8	6.77
21.6	6.83
22.1	6.83
22.8	6.94
23.7	6.93
25.0	6.94
26.2	7.03
28.8	7.11
32.7	7.26
34.8	7.34
35.6	7.32
38.0	7.45

Table A.1: Osmotic pressures induced at 20°C by Polyethylene Glycol of a molecular weight of 20000 Dalton as a function of weight% in water.

Appendix B

Neutron Experiments

B.1 Instrument Parameters (V2-Flex)

Mosaic of analyzer (minutes) ... 30 arcmin

Mosaic of Monochromator (minutes) ... 30 arcmin

Vertical collimation of instrument between
guide to monochromator (minutes) ... open - distance between end of guide and
monochromator is 150 mm

monochromator to sample (minutes) ... given by monochromator height, vertical
diaphragm 1 setting, sample size and L_MS

Sample to analyzer (minutes) ... given by analyzer height, vertical diaphragm 2
setting, sample size and L_SA

Analyzer to detector (minutes) ... given by analyzer height, detector height and
L_AD;

detector height depends on use of detector
diaphragm (Cd mask with 120 mm height)

Horizontal collimation of instrument WITHOUT any soller collimators in place
guide to monochromator (minutes) ... open - distance between end of guide and
monochromator is 150 mm

monochromator to sample (minutes) ... given by effective monochromator width,
horizontal diaphragm 1 setting, sample size and
L_MS

Sample to analyzer (minutes) ... given by effective analyzer width, horizontal
diaphragm 2 setting, sample size and L_SA

Analyzer to detector (minutes) ... given by effective analyzer width, detector
height and L_AD;

detector width depends on use of detector

diaphragm (Cd masks with 10, 20 or 30 mm width)

width of individual analyzer blades on the focusing analyzer ... 15 analyzer blades
each 13 mm

wide

Distances (cm)

guide to monochromator ... 0.15 m

monochromator to sample (cm) ... 1.75 m in standard setup

Sample to analyzer (cm) ... depends on setup, typically 1.10 m

Analyzer to detector (cm) ... ranging from 0.46 m to 1.0 m

most experiments with collimation use 0.62 m

Beam height of guide ... 125 mm

Beam width of guide ... 30 mm

detector width ... 49 mm, without detector diaphragm

detector height ... 150 mm, without detector diaphragm

Width of monochromator ... 125 mm

Height of monochromator ... 125 mm

Thickness of monochromator ... 2 mm

Width of analyzer ... 200 mm

Height of analyzer ... 125 mm

Thickness of analyzer ... 2 mm

Width of monitor ... 70 mm (standard setup: monitor in front of diaphr.)

Height of monitor ... 160 mm

B.2 Macro Example (MAD)

```
!DSPC_V2_12.xbu
!V2 HMI 29/3-7/4/2006
! DSPC -d70
  se fx 2
out ki kf a3 a4
  !—————
!T=65C, fluid phase
  !Diffraction
!Chainpeak
dr kf 1.49
sc qh 1.35 0 0 0 dqh 0.005 0 0 0 np 141 mn 25000
  !Inelastics
!constant q-scans
!q=1.465
!11h
dr kf 1.49
sc qh 1.465 0 0 1.50 dqh 0 0 0 0.10 np 61 mn 800000
sc qh 1.465 0 0 0.05 dqh 0 0 0 0.10 np 31 mn 800000
!q=1.0
!7.5h
dr kf 1.49
sc qh 1 0 0 5.5 dqh 0 0 0 0.10 np 51 mn 800000
!q=1.465 aufzaehlen bei 1.6<en<4.5 meV
sc qh 1.465 0 0 3.0 dqh 0 0 0 0.10 np 31 mn 800000
!!q=2.3
!!7.5h
!dr kf 1.49
!sc qh 2.3 0 0 2.80 dqh 0 0 0 0.10 np 51 mn 800000
! !!constant energy scans
!dr kf 1.49
!sc qh 1.465 0 0 2.5 dqh 0.01 0 0 0 np 81 mn 800000
!sc qh 1.465 0 0 2.0 dqh 0.01 0 0 0 np 81 mn 800000
!sc qh 1.465 0 0 3.0 dqh 0.01 0 0 0 np 81 mn 800000
do DSPC_V2_justage.xbu
```

B.3 Data Treatment: Matlab

B.3.1 Fit of Neutron Reflectivities

```
bg=17;
```

```
amp=0.042;
```

```
exponent=-4;
```

```
[fitDSPCreffl(1),fitDSPCreffldata(1)]=
fits(cut(DSPCreffl(1),[0.08 0.35]),'ngauss_q4',[20000 0.1 0.05 5000 0.2 0.05 5000 0.3
0.05 bg amp exponent],[1 1 1 1 1 1 1 1 0 0 0]);
```

```
[fitDSPCreffldata(1).pvals(1) fitDSPCreffldata(1).pvals(2) fitDSPCreffldata(1).pvals(3)
fitDSPCreffldata(1).pvals(4) fitDSPCreffldata(1).pvals(5) fitDSPCreffldata(1).pvals(6)
fitDSPCreffldata(1).pvals(7) fitDSPCreffldata(1).pvals(8) fitDSPCreffldata(1).pvals(9)
fitDSPCreffldata(1).pvals(10) fitDSPCreffldata(1).pvals(11) fitDSPCreffldata(1).pvals(12)]
[fitDSPCreffldata(1).evals(1) fitDSPCreffldata(1).evals(2) fitDSPCreffldata(1).evals(3)
fitDSPCreffldata(1).evals(4) fitDSPCreffldata(1).evals(5) fitDSPCreffldata(1).evals(6)
fitDSPCreffldata(1).evals(7) fitDSPCreffldata(1).evals(8) fitDSPCreffldata(1).evals(9)
fitDSPCreffldata(1).evals(10) fitDSPCreffldata(1).evals(11) fitDSPCreffldata(1).evals(12)]
```

```
[fitDSPCreffl(2),fitDSPCreffldata(2)]=
fits(cut(DSPCreffl(2),[0.07 0.37]),'ngauss_q4',[5000 0.11 0.05 5000 0.205 0.025 5000
0.225 0.025 5000 0.305 0.025 5000 0.33 0.025 bg amp exponent],[1 1 1 1 0 1 1 0 1 1
1 1 1 1 1 0 0 0]);
```

```
[fitDSPCreffldata(2).pvals(1) fitDSPCreffldata(2).pvals(2) fitDSPCreffldata(2).pvals(3)
fitDSPCreffldata(2).pvals(4) fitDSPCreffldata(2).pvals(5) fitDSPCreffldata(2).pvals(6)
fitDSPCreffldata(2).pvals(7) fitDSPCreffldata(2).pvals(8) fitDSPCreffldata(2).pvals(9)
fitDSPCreffldata(2).pvals(10) fitDSPCreffldata(2).pvals(11) fitDSPCreffldata(2).pvals(12)
fitDSPCreffldata(2).pvals(13) fitDSPCreffldata(2).pvals(14) fitDSPCreffldata(2).pvals(15)
fitDSPCreffldata(2).pvals(16) fitDSPCreffldata(2).pvals(17) fitDSPCreffldata(2).pvals(18)]
[fitDSPCreffldata(2).evals(1) fitDSPCreffldata(2).evals(2) fitDSPCreffldata(2).evals(3)
fitDSPCreffldata(2).evals(4) fitDSPCreffldata(2).evals(5) fitDSPCreffldata(2).evals(6)
fitDSPCreffldata(2).evals(7) fitDSPCreffldata(2).evals(8) fitDSPCreffldata(2).evals(9)
fitDSPCreffldata(2).evals(10) fitDSPCreffldata(2).evals(11) fitDSPCreffldata(2).evals(12)
fitDSPCreffldata(2).evals(13) fitDSPCreffldata(2).evals(14) fitDSPCreffldata(2).evals(15)
fitDSPCreffldata(2).evals(16) fitDSPCreffldata(2).evals(17) fitDSPCreffldata(2).evals(18)]
```

```
[fitDSPCreffl(3),fitDSPCreffldata(3)]=
fits(cut(DSPCreffl(3),[0.085 0.38]),'ngauss_q4',[5000 0.11 0.05 5000 0.22 0.05 5000
0.33 0.05 bg amp exponent],[1 1 1 1 1 1 1 1 1 0 0 0]);
```

```

[fitDSPCreffdata(3).pvals(1) fitDSPCreffdata(3).pvals(2) fitDSPCreffdata(3).pvals(3)
fitDSPCreffdata(3).pvals(4) fitDSPCreffdata(3).pvals(5) fitDSPCreffdata(3).pvals(6)
fitDSPCreffdata(3).pvals(7) fitDSPCreffdata(3).pvals(8) fitDSPCreffdata(3).pvals(9)
fitDSPCreffdata(3).pvals(10) fitDSPCreffdata(3).pvals(11) fitDSPCreffdata(3).pvals(12)]
[fitDSPCreffdata(3).evals(1) fitDSPCreffdata(3).evals(2) fitDSPCreffdata(3).evals(3)
fitDSPCreffdata(3).evals(4) fitDSPCreffdata(3).evals(5) fitDSPCreffdata(3).evals(6)
fitDSPCreffdata(3).evals(7) fitDSPCreffdata(3).evals(8) fitDSPCreffdata(3).evals(9)
fitDSPCreffdata(3).evals(10) fitDSPCreffdata(3).evals(11) fitDSPCreffdata(3).evals(12)]

```

```

clf;
h=plot(fitDSPCreff(1),fitDSPCreff(2),fitDSPCreff(3),'semilogy');

```

```

grid('off');
xlabel('Qz (⁻¹)', 'interp', 'tex', 'fontsize', [20], 'fontname', 'Times');
ylabel('log (neutron counts)', 'interp', 'tex', 'fontsize', [20], 'fontname', 'Times');
legend(h, '50°C', '55°C', '65°C');

```

B.3.2 DMPC/Ethanol Bilayer Decay

```

t = [(30+45/60+06/3600) (32+46/60+33/3600) (39+18/60+29/3600) (48+54/60+28/3600)
(57+41/60+10/3600) (64+15/60+08/3600) (70+56/60+25/3600) (78+55/60+14/3600)
(85+7/60+44/3600) (95+55/60+3/3600) (103+35/60+44/3600) (109+46/60+55/3600)
(120+32/60+10/3600) (131+17/60+54/3600) (137+29/60+50/3600) (143+40/60+58/3600)
(155+24/60+32/3600) (166+13/60+49/3600) (176+22/60+8/3600) (182+24/60+58/3600)
(188+15/60+16/3600) (196+51/60+44/3600) (210+11/60+2/3600) (218+52/60+22/3600)];
DMPCEthreflang=loads('illbatch', 'data/025[211 216 221 224 228 233 238 241 244
247 252 255 258 261 264 267 274 277 280 283 288 291 295 298],X=QH,Y=CNITS,M=M1')*400000;
%Korrektur für Offset vom Drehzentrum
kf=1.25;
j=1;
for j=1:length(DMPCEthreflang)
[qh y ye]=extract(DMPCEthreflang(j));

i=1;
for i=1:length(qh)
a40=acos(1-qh.Â/(2*kfÂ))/pi*180;
a40corr=a40-0.6;

```

```

qhcorr=sqrt((1-cos(a40corr*pi/180))*2*kf2);
end
    tmp.x=qhcorr;
tmp.y=y;
tmp.e=ye;
    DMPCEthreflangcorr(j)=spec1d(tmp);
    clf;
h=plot(DMPCEthreflang(j), DMPCEthreflangcorr(j));
pause(1);
j=j+1;
end
    clf;
h=plot(DMPCEthreflangcorr(1),DMPCEthreflangcorr(12),DMPCEthreflangcorr(24),'semilogy');
legend(h, '31 h','110 h','218 h');
    pause;
    %Fit als Gesamtes
    bg=982;
amp=0.042;
exponent=-4;
    [fitDMPCEthreflangcorr(1),fitDMPCEthreflangcorrdata(1)]
=fits(DMPCEthreflangcorr(1),'ngauss_q4',[5.3349e+005 0.1153 0.006 3.1290e+005
0.2176 0.0064 2.5461e+004 0.3244 0.0099 2.2954e+003 0.4239 0.0114 bg amp expo-
nent],
[1 1 1 1 1 1 1 1 1 1 0 0 1 0]);
    [fitDMPCEthreflangcorrdata(1).pvals(1) fitDMPCEthreflangcorrdata(1).pvals(2)
fitDMPCEthreflangcorrdata(1).pvals(3) fitDMPCEthreflangcorrdata(1).pvals(4) fit-
DMPCEthreflangcorrdata(1).pvals(5) fitDMPCEthreflangcorrdata(1).pvals(6) fit-
DMPCEthreflangcorrdata(1).pvals(7) fitDMPCEthreflangcorrdata(1).pvals(8) fit-
DMPCEthreflangcorrdata(1).pvals(9) fitDMPCEthreflangcorrdata(1).pvals(10) fit-
DMPCEthreflangcorrdata(1).pvals(11)
fitDMPCEthreflangcorrdata(1).pvals(12)]
[fitDMPCEthreflangcorrdata(1).evals(1) fitDMPCEthreflangcorrdata(1).evals(2) fit-
DMPCEthreflangcorrdata(1).evals(3) fitDMPCEthreflangcorrdata(1).evals(4) fitDM-
PCEthreflangcorrdata(1).evals(5) fitDMPCEthreflangcorrdata(1).evals(6) fitDMPCEthre-
flangcorrdata(1).evals(7) fitDMPCEthreflangcorrdata(1).evals(8) fitDMPCEthreflang-
corrdata(1).evals(9) fitDMPCEthreflangcorrdata(1).evals(10) fitDMPCEthreflang-
corrdata(1).evals(11)

```

```

fitDMPCEthreflangcorrdata(1).evals(12)]
    clf;
h=plot(DMPCEthreflangcorr(1),fitDMPCEthreflangcorr(1),'semilogy');
    pause(1);
    ...
    %zeitabhängige Veränderung der Fläche unter jeweils dem 1. und 2. Bragg Peak
%Sichtung der gefitteten Peaks
    [xfitDMPCEthreflangcorr1 yfitDMPCEthreflangcorr1 efitDMPCEthreflangcorr1]
=extract(fitDMPCEthreflangcorr(1));
    i=1;
for i=1:length(xfitDMPCEthreflangcorr1)
yfitDMPCEthreflangcorr1ucorr(i)=yfitDMPCEthreflangcorr1(i)
-(1./(xfitDMPCEthreflangcorr1(i).^4)*fitDMPCEthreflangcorrdata(1).pvals(14)
+fitDMPCEthreflangcorrdata(1).pvals(13)); i=i+1;
end
    tmp.x=xfitDMPCEthreflangcorr1;
tmp.y=yfitDMPCEthreflangcorr1ucorr;
tmp.e=efitDMPCEthreflangcorr1;
    fitDMPCEthreflangcorrucorr(1)=spec1d(tmp);
    clf;
h=plot(DMPCEthreflangcorr(1),fitDMPCEthreflangcorr(1),
cut(fitDMPCEthreflangcorrucorr(1),[0.295 0.38]),'semilogy');
%h=plot(DMPCEthreflangcorr(1),fitDMPCEthreflangcorr(1),
cut(fitDMPCEthreflangcorrucorr(1),[0.17 0.26]),'semilogy');
%h=plot(DMPCEthreflangcorr(1),fitDMPCEthreflangcorr(1),
cut(fitDMPCEthreflangcorrucorr(1),[0.08 0.15]),'semilogy');
    ...
    %Berechnung der Fläche unter 1.,2. und 3. Peak
    Apeak1_1=0.005*sum(yfitDMPCEthreflangcorr1ucorr(8:21))
Apeak1_1e=0.005*sum(efitDMPCEthreflangcorr1(8:21))
Apeak1_2=0.005*sum(yfitDMPCEthreflangcorr1ucorr(25:43))
Apeak1_2e=0.005*sum(efitDMPCEthreflangcorr1(25:43))
Apeak1_3=0.005*sum(yfitDMPCEthreflangcorr1ucorr(50:67))
Apeak1_3e=0.005*sum(efitDMPCEthreflangcorr1(50:67))

    %Zeitabhängigkeit plotten Apeak1=[Apeak1_1 Apeak2_1 Apeak3_1 Apeak4_1
Apeak5_1 Apeak6_1 Apeak7_1 Apeak8_1 Apeak9_1 Apeak10_1 Apeak11_1 Apeak12_1

```

```

Apeak13_1 Apeak14_1 Apeak15_1 Apeak16_1 Apeak17_1 Apeak18_1 Apeak19_1 Apeak20_1
Apeak21_1 Apeak22_1 Apeak23_1 Apeak24_1]; Apeak1e=[Apeak1_1e Apeak2_1e Apeak3_1e
Apeak4_1e Apeak5_1e Apeak6_1e Apeak7_1e Apeak8_1e Apeak9_1e Apeak10_1e
Apeak11_1e Apeak12_1e Apeak13_1e Apeak14_1e Apeak15_1e Apeak16_1e Apeak17_1e
Apeak18_1e Apeak19_1e Apeak20_1e Apeak21_1e Apeak22_1e Apeak23_1e Apeak24_1e];
    tmp.x=t(1:24);
tmp.y=Apeak1;
tmp.e=Apeak1e;
    A1=spec1d(tmp);
    ...
    clf;
h=plot(A1,A2);
legend(h, 'peak 1', 'peak 2');
    ...
    pause(1);
    %Fit: exponential decay (mit Normierung auf Peakfläche zur Zeit null)
    [fitDMPCEthdecay1,fitDMPCEthdecay1data]=fits(A1/Apeak1_1,'expon',[1.2 7.5696
0.5],[1 1 1]);
    [fitDMPCEthdecay1data.pvals(1) fitDMPCEthdecay1data.pvals(2) fitDMPCEthdecay1data.pvals(3)
fitDMPCEthdecay1data.evals(1) fitDMPCEthdecay1data.evals(2)fitDMPCEthdecay1data.evals(3)]
    clf;
h=plot(A1/Apeak1_1,fitDMPCEthdecay1);
    x=1:0.5:250;
line(x,fitDMPCEthdecay1data.pvals(1)*exp(-x/fitDMPCEthdecay1data.pvals(2))
+fitDMPCEthdecay1data.pvals(3),'color','red');
    pause(1);
    ...
    %zeitabhängige Veränderung des Dz-spacings
    i=1;
j=2;
for i=1:length(DMPCEthreflang)
Dz(i)=2*pi/((fitDMPCEthreflangcorrdata(i).pvals(j)+fitDMPCEthreflangcorrdata(i).pvals(j+3)/2
+fitDMPCEthreflangcorrdata(i).pvals(j+6)/3
+fitDMPCEthreflangcorrdata(i).pvals(j+9)/4)/4);
eDz(i)=2*pi*(fitDMPCEthreflangcorrdata(i).evals(j)+fitDMPCEthreflangcorrdata(i).evals(j+3)/2
+fitDMPCEthreflangcorrdata(i).evals(j+6)/3
+fitDMPCEthreflangcorrdata(i).evals(j+9)/4)./(fitDMPCEthreflangcorrdata(i).pvals(j)

```

```
+fitDMPCEthreflangcorrdata(i).pvals(j+3)/2+fitDMPCEthreflangcorrdata(i).pvals(j+6)/3
+fitDMPCEthreflangcorrdata(i).pvals(j+9)/4).^2;
i=i+1;
end
    tmp.x=t;
tmp.y=Dz;
tmp.e=eDz; %aus Fehlerfortpflanzung ermittelt
    Dzspac=spec1d(tmp);
clf;
h=plot(Dzspac);
```


B.4 Treatment of Inelastic Data

B.4.1 Energy-Scans: Detailed Balance Correction

```

enDSPC50(1)
=loads('illbatch','01[1265;1267],X=EN,Y=CNLS,M=M1')*400000;

    %Temperaturkorrektur (Detailed Balance)
kB=1.38E-23;
el=1.6E-19;
T1=50;
for n=1:length(enDSPC50)
normalisierung=(1-exp(-1E-5/(kB*(T1+273)/el*1000)))/1E-5;
werten=getfield(enDSPC50(1),'x');
%energie korrektur im vergleich zu den alten messungen
wertcnts=getfield(enDSPC50(1),'y');
wertcntsalt=getfield(enDSPC50(1),'y');
for m=1:length(werten)
fac(m)=werten(m)./(1-exp(-werten(m)./(kB*(T1+273)/el*1000)))*normalisierung;
wertcnts(m)=wertcnts(m)./fac(m);
end;
[werten wertcnts]
enDSPC50(1)=setfield(enDSPC50(1),'x',werten);
enDSPC50(1)=setfield(enDSPC50(1),'y',wertcnts);
end;

```

B.4.2 Energy-Scans: Absorption Correction

```

omega=getfield(enDSPC50(1),'x');

    kf=1.49;
Q=1.0;

    ki=sqrt(omega/2.072+kf^2);

    testa4_0=acos(1-Q^2/(2*kf^2))/180*pi;
testa4=acos((-Q^2+kf^2+ki.^2)./(2*kf.*ki))/180*pi;

```

```
testa3_0=(180-testa4_0)/2; tmp=(-kf^2+Q^2+ki.^2)./(2*Q.*ki);
testa3=acos(tmp)/180*pi; delta_a3=testa3_0-testa3;
```

```
absorption=(cos(testa3-testa3_0)+cos(testa3-testa4/2));
```

```
energy50_10=getfield(enDSPC50(1),'x');
counts50_10=getfield(enDSPC50(1),'y');
fehlercounts50_10=getfield(enDSPC50(1),'e');
```

```
corrtest50_10=(absorption).*counts50_10;
fehlercorrtest50_10=sqrt(corrtest50_10);
```

```
tmp50_10.x=energy50_10;
tmp50_10.y=corrtest50_10;
tmp50_10.e=fehlercorrtest50_10;
```

```
enDSPC50_10corrabsorb=spec1d(tmp50_10);
clf;
h=plot(enDSPC50(1),enDSPC50_10corrabsorb);
```

```
axis([2.5 8.5 0 17]);
```

B.5 Resolution Calculation with 'Rescal'

Spectrometer

DM: monochromator d-spacing in Å; DA: analyzer d-spacing

ETAM: monochromator mosaic in min.;

ETAA: analyzer mosaic; ETAS: sample mosaic

SM: scattering sense from monochromator (+1: right, -1: left);

SS: scattering sense from sample;

SA: scattering sense from analyzer

KFIX: fixed neutron wave vector in Å⁻¹;

FX: index for fixed wave vector (1=incident, 2=final)

ALF1: horizontal source-mono. collimation in min.;

ALF2: horizontal mono.-sample collimation;

ALF3: horizontal sample-analyzer collimation;

ALF4: horizontal analyzer-detector collimation

Spectrometer					
DM	3.355	DA	3.355		
ETAM	30	ETAA	30	ETAS	42
SM	-1	SS	-1	SA	1
KFIX	1.49	FX	2		
ALF1	50	ALF2	60	ALF3	60
		ALF4	60		
BET1	600	BET2	600	BET3	600
		BET4	600		
Lattice					
AS	6.28	BS	6.28	CS	6.28
AA	90	BB	90	CC	90
AX	1	AY	0	AZ	0
BX	0	BY	0	BZ	1
Scan					
QH	0	QK	0	QL	1.475
		EN	1.35		
DH	0	DK	0	DL	0
		DE	0.1		
GH	0	GK	0	GL	0
		GMOD	0		

Figure B.1: Rescal: Parameters window for resolution calculation according to the Cooper-Nathans as well as the Popovici method.

BET1: vertical source-mono. collimation in min.;

BET2: vertical mono.-sample collimation;

BET3: vertical sample-analyzer collimation;

BET4: vertical analyzer-detector collimation

Lattice

AS, BS, CS: sample lattice parameters

AA: angle between axis B and C in degree;

BB: angle between axis A and C;

CC: angle between axis A and B

AX: first wave vector in scattering plane coordinate H (r l u); AY: first wave vector in scattering plane coordinate K (r l u); AZ: first wave vector in scattering plane coordinate L (r l u)

BX: second wave vector in scattering plane coordinate H (r l u); BY: second wave vector in scattering plane coordinate K (r l u); BZ: second wave vector in scattering plane coordinate L (r l u)

Scan

QH: position of resolution wave vector (center) (r l u);

QK: position of resolution wave vector (center) (r l u);

Rectangular source (cm)	Width	3	Height	12.5
Guide (min/Å)	DIVH	7.05	DIVV	7.05
Flat-plate sample (cm)	Depth	2	Width	5
	Height	5		
Rectangular detector (cm)	Width	4.9	Height	15
Mono (cm):	Depth	0.2	Width	12.5
	Height	12.5		
Analyser (cm):	Depth	0.2	Width	20
	Height	12.5		
Dist (cm):	L0	15	L1	165
	L2	140	L3	100
Focus (1/m):	ROMH	0	ROMV	0.54839
	ROAH	0	ROAV	1.3639

Figure B.2: Rescal: Instrument window for resolution calculation according to the Popovici method.

QL: position of resolution wave vector (center) ($r \ l \ u$)

DH: increment of Q defining general scan step along H (Å^{-1}); DK: increment of Q defining general scan step along K (Å^{-1}); DL: increment of Q defining general scan step along L (Å^{-1}); DE: increment of Q defining general scan step along ω (meV)

GH: gradient of dispersion (planar) direction along H;

GK: gradient of dispersion (planar) direction along K;

GL: gradient of dispersion (planar) direction along L;

GMOD: gradient of dispersion (planar) energy ($\text{meV}/\text{Å}^{-1}$)

The Rescal instrument window is only available if the resolution calculation is performed according to the method of Popovici (compare 3.3.3).

source geometry: circular/rectangular (lengths in cm);

guide: DIVH: horizontal divergence of guide (Nickel: $6 \text{ min}/\text{Å}$);

sample geometry: cylindrical/flat (lengths in cm);

detector geometry: circular/rectangular (lengths in cm);

monochromator size: depth, width, height (lengths in cm);

analyzer size: depth, width, height (lengths in cm);

distances between instrument components (in cm)

L0: source/guide - monochromator,

L1: monochromator - sample,

L2: sample - analyzer,

L3: analyzer - detector;

curvature radius for focussing optics (1/m):

ROMA: horizontal monochromator, ROMV: vertical monochromator,

ROAH: horizontal analyzer, ROAV: vertical analyzer

Fig.'s B.3, B.4 show cuts through the resolution ellipsoid for the same constant-Q

Instrument	SM	SS	SA
IN12 (ILL)	+1	-1	+1
V2-Flex (HMI)	-1	-1	+1

Table B.1: The respective scattering sense configuration directly influences the orientation of resolution ellipsoids shown in Fig.'s B.3 and B.4.

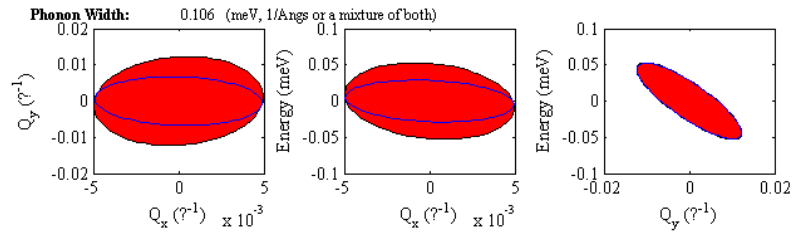


Figure B.3: Cuts through resolution ellipsoid for an energy scan calculated at the dispersion minimum ($Q=1.47 \text{ \AA}^{-1}$) according to Popovici: $\omega=1.2 \text{ meV}$, IN12 (ILL).

scan measured on the cold three-axis spectrometers IN12 (ILL) and V2-Flex (HMI) at identical energy values. In both cases the Popovici method was employed (see also 3.3.3). The orientation of the resolution ellipsoids is influenced by the respective scattering sense geometries that were used:

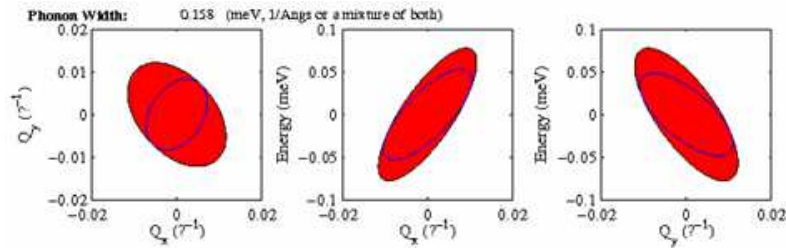


Figure B.4: Cuts through resolution ellipsoid for an energy scan calculated at the dispersion minimum ($Q=1.47 \text{ \AA}^{-1}$) according to Popovici: $\omega=1.2 \text{ meV}$, V2 (HMI).

Bibliography

- [1] S. Paula, A. G. Volkow, A. N. Van Hoek, T. H. Haines, and D. W. Deamer. *Biophys. J.*, 70:339–348, 1996.
- [2] J. F. Nagle and H. L. jr Scott. *Biochim. Biophys. Acta*, 513:236, 1978.
- [3] H. Reinl, T. Brumm, and T. M. Bayerl. *Biophys. J.*, 61:1025, 1992.
- [4] H.A. Scheidt, D. Huster, and K. Gawrisch. *Biophys. J.*, 89:2504, 2005.
- [5] W. Pfeiffer, Th. Henkel, E. Sackmann, W. Knoll, and D. Richter. *Europhys. Lett.*, 8:201–206, 1989.
- [6] C. Gliss, O. Randel, H. Casalta, E. Sackmann, R. Zorn, and T. Bayerl. *Biophys. J.*, 77:331, 1999.
- [7] S. H. Chen, C. Y. Liao, H. W. Huang, T. M. Weiss, M. C. Bellisent-Funel, and F. Sette. *Phys. Rev. Lett.*, 86:740, 2001.
- [8] M. C. Rheinstädter, C. Ollinger, G. Fragneto, F. Demmel, and T. Salditt. *Phys. Rev. Lett.*, 93:108107, 2004.
- [9] W. Pfeffer. *Osmotische Untersuchungen. Studien zur Zellmechanik.* W. Engelmann, Leipzig, 1877.
- [10] E. Gorter and F. Grendel. *J. Exp. Med.*, 41:439–443, 1925.
- [11] S. J. Singer and G. L. Nicolson. *Science*, 173:720, 1972.
- [12] O. G. Mouritsen and M. Bloom. *Biophys. J.*, 46:141–153, 1984.
- [13] J. Israelachvili. *Intermolecular and Surface Forces.* Academic Press, Amsterdam, 2006.
- [14] T. Heimburg. *Biophys. J.*, 78:1154–1165, 2000.
- [15] T. Heimburg. *Thermal Biophysics of Membranes.* Wiley, Weinheim, 2007.

- [16] W. Nolting. *Statistische Physik*. Springer, Berlin, 2004.
- [17] R.B. Gennis. *Biomembranes*. Springer, New York, 1989.
- [18] W. Fenzl. *Z. Phys. B*, 97:333–336, 1995.
- [19] U. Mennicke. *Struktur und Fluktuationen festkörpergestützter Phospholipidmembranen*. Dissertation, Göttingen, 2003.
- [20] K. Gawrisch, D. Ruston, J. Zimmerberg, V. A. Parsegian, R. P. Rand, and N. Fuller. *Biophys. J*, 61:1213–1223, 1992.
- [21] N. Chu, N. Kucerka, Y. Liu, S. Tristam-Nagle, and J. F. Nagle. *Phys. Rev. E*, 71:041904, 2005.
- [22] M. C. Rheinstädter, T. Seydel, F. Demmel, and T. Salditt. *Phys. Rev. E*, 71:061908, 2005.
- [23] R. Zhang, W. Sun, S. Tristam-Nagle, R.L. Headrick, R. Suter, and J.F. Nagle. *Phys. Rev. Lett.*, 74:2832, 1995.
- [24] J. F. Nagle, H. I. Petrache, N. Gouliaev, S. Tristam-Nagle, Y. Liu, R. M. Suter, and K. Gawrisch. *Phys. Rev. E*, 58:7769, 1998.
- [25] P.C. Mason, J.F. Nagle, R.M. Epand, and J. Katsaras. *Phys. Rev. E*, 63:030902(R), 2001.
- [26] G. Pabst, H. Amenitsch, D. P. Kharakoz, P. Laggner, and M. Rappolt. *Phys. Rev. E*, 70:021908, 2004.
- [27] E. Sackmann. *Biological membranes architecture and function*. In *Structure and dynamics of membrane*. Lipowsky R. and E. Sackmann (eds.). Elsevier, Amsterdam, 1995.
- [28] A. Kusumi, M. Tsuda, T. Akino, S. Ohnishi, and Y. Terayama. *Biochemistry*, 22:1165–1170, 1983.
- [29] O. G. Mouritsen and K. Jorgensen. *Chem. Phys. Lipids*, 73:3–25, 1994.
- [30] K. Simons and E. Ikonen. *Nature*, 387:569–572, 1997.
- [31] R. Bittman, S. Clejan, S. Lund-Katz, and M. C. Phillips. *Biochim. Biophys. Acta.*, 772:117–126, 1984.
- [32] W. K. Subczynski, J. S. Hyde, and A. Kusumi. *Proc. Natl. Acad. Sci.*, 86:4474–4478, 1989.

- [33] W. K. Subczynski, A. Wisuiewska, J.-J. Yin, J. S. Hyde, and A. Kusumi. *Biochemistry*, 33:7670–7681, 1994.
- [34] M. Y. El-Sayed, T. A. Guion, and M. D. Fayer. *Biochemistry*, 25:4825–4832, 1986.
- [35] M. Bloom, E. Evans, and O. G. Mouritsen. *Q. Rev. Biophys.*, 24:293–397, 1991.
- [36] M. Bloom and O. G. Mouritsen. *The evolution of membrane. In Structure and dynamics of membrane. Lipowsky R. and E. Sackmann (eds.)*. Elsevier, Amsterdam, 1995.
- [37] M. R. Vist and J. H. Davis. *Biochemistry*, 29:451, 1990.
- [38] I. Vattulainen. *Diff. Fund.*, 2:113.1–113.15, 2005.
- [39] M. B. Sankaram and T. E. Thompson. *Biochemistry*, 29:10670, 1990.
- [40] M. B. Sankaram and T. E. Thompson. *Proc. Natl. Acad. Sci.*, 88:8686, 1991.
- [41] F. Richter, G. Rapp, and L. Finegold. *Phys. Rev. E*, 63:051914, 2001.
- [42] P.F.F. Almeida, W.L.C. Vaz, and T.E. Thompson. *Biochemistry*, 31:6739, 1992.
- [43] G. Ipsen, J. H. and Karlstrom, O. G. Mouritsen, H. Wennerstrom, and M. J. Zuckermann. *Biochim. Biophys. Acta*, 905:162–172, 1987.
- [44] D. J. Recktenwald and H. M. McConnell. *Biochemistry*, 20:4505, 1981.
- [45] J. Huang and G. W. Feigensohn. *Biophys. J.*, 76:2142, 1999.
- [46] A.M. Smondyrev and M.L. Berkowitz. *Biophys. J.*, 77:2075, 1999.
- [47] S. Karmakar and V. A. Raghunathan. *Phys. Rev. Lett.*, 91:098102, 2003.
- [48] S. Karmakar and V. A. Raghunathan. *Phys. Rev. E*, 71:061924, 2005.
- [49] S. Karmakar, V. A. Raghunathan, and S. Mayor. *J. Phys.: Cond. Matt.*, 17:S1177–S1182, 2005.
- [50] K. Mortensen, W. Pfeiffer, E. Sackmann, and W. Knoll. *Biochim. Biophys. Acta*, 945:221–245, 1988.
- [51] E. Endress, H. Heller, H. Casalta, M. F. Brown, and T. M. Bayerl. *Biochemistry*, 41:13078–13086, 2002.

- [52] B. W. Barry. *Eur. J. Pharm. Sciences*, 14:101, 2001.
- [53] H. Benson. *Curr. Drug Delivery*, 2:23, 2005.
- [54] K. Vávrova, J. Zbytovská, and A. Hrabálek. *Curr. Med. Chem.*, 12:2273, 2005.
- [55] T. Heimburg and A. D. Jackson. *Biophys. Rev. Lett.*, 2:57–78, 2007.
- [56] T. Heimburg and A. D. Jackson. *Biophys. J.*, 92:3159–3165, 2007.
- [57] P. Nambi, E. S. Rowe, and T. J. McIntosh. *Biochem.*, 27:9175, 1988.
- [58] U. Vierl, L. Löbbecke, N. Nagel, and G. Cevc. *Biophys. J.*, 67:1067, 1994.
- [59] J. Chanda and S. Bandyopadhyay. *Chem. Phys. Lett.*, 392:249, 2004.
- [60] J. A. Barry and K. Gawrisch. *Biochemistry*, 33:8082–8088, 1994.
- [61] L. L. Holte and K. Gawrisch. *Biochemistry*, 36:4669–4674, 1997.
- [62] S. E. Feller, C. A. Brown, D. T. Nizza, and K. Gawrisch. *Biophys. J.*, 82:1396–1404, 2002.
- [63] B. W. Koenig and K. Gawrisch. *J. Phys. Chem. B*, 109:7540–7547, 2005.
- [64] H. Trauble. *J. Membr. Biol.*, 4:193–208, 1971.
- [65] A. Hodgkin and A. Huxley. *J. Physiol.*, 117:500–544, 1952.
- [66] T. Heimburg and A. D. Jackson. *Proc. Natl. Acad. Sci.*, 102:9790–9795, 2005.
- [67] T. Heimburg. *Biochim. Biophys. Acta*, 1415:147–162, 1998.
- [68] S. Halstenberg, T. Heimburg, T. Hianik, U. Kaatze, and R. Krivanek. *Biophys. J.*, 75:264–271, 1998.
- [69] W. Schrader, H. Ebel, P. Grabitz, E. Hanke, T. Heimburg, M. Hoeckel, M. Kahle, F. Wentz, and U. Kaatze. *J. Phys. Chem. B*, 106:6581–6586, 2002.
- [70] T. A. Harroun, J. Katsaras, and S. R. Wassall. *Biochemistry*, 45:1227–1233, 2006.
- [71] G. Shirane, S. M. Shapiro, and J. M. Tranquada. *Neutron scattering with a triple-axis spectrometer: basic techniques*. Cambridge Univ. Press, Cambridge, 2002.
- [72] G. L. Squires. *Introduction to the theory of thermal neutron scattering*. Cambridge Univ. Press, Cambridge, 1978.

- [73] L. Van Hove. *Phys. Rev.*, 95:251, 1954.
- [74] V. F. Sears. *Thermal neutron scattering lengths and cross sections for condensed matter research*. Atomic Energy Canada Ltd., Chalk River, Ontario, Canada, 1984.
- [75] M. C. Rheinstädter, T. Seydel, W. Häußler, and T. Salditt. *Physica B*, 385-386:722, 2006.
- [76] J. S. Hub, T. Salditt, M. C. Rheinstädter, and B. L. de Groot. *Biophys. J.*, 2007.
- [77] M. C. Rheinstädter, T. Seydel, and T. Salditt. *Phys. Rev. E*, 75:011907, 2007.
- [78] M. C. Rheinstädter, J. Das, E. J. Flenner, B. Brüning, T. Seydel, and I. Kosztin. *Phys. Rev. Lett.*, 101:248106, 2008.
- [79] M. C. Rheinstädter, W. Häußler, and T. Salditt. *Phys. Rev. Lett.*, 97:048103, 2006.
- [80] M. Tarek, D. J. Tobias, S.-H. Chen, and M. L. Klein. *Phys. Rev. Lett.*, 87:2381, 2001.
- [81] T. M. Weiss, P.-J. Chen, H. Sinn, E. E. Alp, S.-H. Chen, and H. W. Huang. *Biophys. J.*, 84:3767, 2003.
- [82] A. A. van Well, P. Verkerk, and L. A. de Graaf. *Phys. Rev. A*, 31:3391, 1985.
- [83] A. A. van Well and L. A. de Graaf. *Phys. Rev. A*, 32:2396, 1985.
- [84] I. M. de Schepper, P. Verkerk, A. A. van Well, and L. A. de Graaf. *Phys. Rev. Lett.*, 50:974, 1983.
- [85] P. G. De Gennes. *Physica*, 25:825–839, 1959.
- [86] C. Y. Liao, S. H. Chen, and F. Sette. *Phys. Rev. E*, 61:1518, 2000.
- [87] J. Teixeira, M. C. Bellissent-Funel, S. H. Chen, and B. Dorner. *Phys. Rev. Lett.*, 54:2681, 1985.
- [88] E. G. D. Cohen and I. M. de Schepper. *Il Nuovo Cimento D*, 12:521, 1990.
- [89] P. G. de Gennes and J. Prost. *The Physics of Liquid Crystals*. Clarendon Press, Oxford, 1993.

- [90] E. I. Kats and V. V. Lebedev. *Fluctuational Effects in the Dynamics of Liquid Crystals*. Springer, New York, 1994.
- [91] W. R. Busing and H. A. Levy. *Acta Cryst.*, 22:457, 1967.
- [92] L. D. Cussen. *J. Appl. Cryst.*, 33:1399, 2000.
- [93] M. J. Cooper and R. Nathans. *Acta Cryst. A*, 23:357, 1967.
- [94] A. Ghose, H. Palevsky, D. J. Hughes, I. Pelah, and C. M. Eisenhauer. *Phys. Rev.*, 113:49, 1959.
- [95] S. Klotz. *Z. Kristallogr.*, 216:420–429, 2001.
- [96] M. Popovici. *Acta Cryst. A*, 31:507, 1975.
- [97] M. C. Rheinstädter, C. Ollinger, G. Fragneto, and T. Salditt. *Physica B*, 350:136–139, 2004.
- [98] G. S. Smith, E. B. Sirota, C. R. Safinya, and N. A. Clark. *Phys. Rev. Lett.*, 60:813, 1988.
- [99] L. Greenspan. *J. of Research, National Bureau of Standards*, 81A:89–96, 1977.
- [100] Z. Khattari, G. Brotons, M. Akkawi, E. Arbely, and T. Salditt. *Biophys. J.*, 90:2038–2050, 2006.
- [101] E. G. D. Cohen, P. Westerhuijs, and I. M. de Schepper. *Phys. Rev. Lett.*, 59:2872, 1987.
- [102] B. Fak and B. Dorner. *Physica B*, 234:1107, 1997.
- [103] H. Ebel, P. Grabitz, and T. Heimburg. *J. Phys. Chem. B*, 105:7353–7360, 2001.
- [104] M. Hildenbrand. *Modulation kollektiver Membrandynamik im mesoskopischen Bereich durch Einbau und Adsorption von Biomolekülen*. Dissertation, Würzburg, 2004.
- [105] M. F. Hildenbrand and T. M. Bayerl. *Biophys. J.*, 88:3360, 2005.
- [106] M. C. Giocondi and C. Le Grimellec. *Biophys. J.*, 86:2218, 2004.
- [107] E. Falck, M. Patra, M. Karttunen, M. T. Hyvönen, and I. Vattulainen. *Biophys. J.*, 87:1076, 2004.

- [108] M. Pasenkiewicz-Gierula, T. Róg, K. Kitamura, and A. Kusumi. *Biophys. J.*, 78:1376, 2000.
- [109] S. W. Chiu, E. Jakobsson, and H. L. Scott. *Biophys. J.*, 80:1104, 2001.
- [110] K. Tu, M. L. Klein, and J. T. Douglas. *Biophys. J.*, 75:2147, 1998.
- [111] S. Marcelja. *J. Chem Phys*, 60:3599, 1974.
- [112] S. Marcelja and J. Wolfe. *Biochim. Biophys Acta*, 557:24–31, 1979.
- [113] P. V. Dolganov, V. M. Zhilin, and V. K. Dolganov. *Phys. Rev. E*, 67:041716, 2003.
- [114] P. L. Chong. *Proc. Natl. Acad. Sci.*, 91:10069–10073, 1994.
- [115] J. A. Virtanen, M. Ruonala, M. Vauhkonen, and P. Somerharju. *Biochemistry*, 34:11568–11581, 1995.
- [116] S. J. Marrink, A. H. de Vries, T. A. Harroun, J. Katsaras, and S. R. Wassall. *J. Am. Chem. Soc.*, 130:10–11, 2008.
- [117] T. A. Harroun, J. Katsaras, and S. R. Wassall. *Biochemistry*, 47:7090–7096, 2008.
- [118] M. Brzustowicz, V. Cherezov, M. Caffrey, W. Stillwell, and S. R. Wassall. *Biophys. J.*, 82:285–298, 2002.
- [119] A. Braslau, P. S. Pershan, G. Swislow, B. M. Ocko, and J. Als-Nielsen. *Phys. Rev. A*, 38:2457, 1988.
- [120] J. Als-Nielsen and D. McMorrow. *Elements of Modern X-ray Physics*. Wiley, New York, 2001.
- [121] T. Salditt, C. Li, A. Spaar, and U. Mennicke. *Europhys. J. E*, 7:105–116, 2002.
- [122] S. Tristram-Nagle, H. Petrache, and J. F. Nagle. *Biophys. J.*, 75:917–925, 1998.
- [123] M. Gandhavadi, D. Allende, A. Vidal, S. A. Simon, and T. J. McIntosh. *Biophys. J.*, 82:1469–1462, 2002.
- [124] E. Novakova, K. Giewemeyer, and T. Salditt. *Phys. Rev. E*, 74:051911, 2006.
- [125] Ch. Li, D. Constantin, and T. Salditt. *J. Phys.: Cond. Matt.*, 16:S2439–S2453, 2004.
- [126] A. Spaar and T. Salditt. *Biophys. J.*, 85:1576–1584, 2003.

Acknowledgements

At this point, I would like to acknowledge Tim Salditt for proposing this challenging topic and for the interest he has shown in my in-house work at the Institut für Röntgenphysik (IRP) in Göttingen over the past three years. Also, I wish to thank him for the unique opportunity to spend the majority of my phd-time in a truly inspiring working environment such as the Institut Laue-Langevin (ILL) in Grenoble, France. Thank you for your vote of confidence.

A special thank you also goes to Helmut Schober, who has agreed to co-referee this thesis, and whose office door at the ILL was always open to me, even during my long stay in Germany in the past year. I also thank Maikel Rheinstädter for his continuous efforts to help me get started at the ILL at the beginning of my thesis, and for returning from the United States twice for mutual experiments.

At the IRP, I particularly enjoyed the times I spent preparing neutron experiments and characterizing my samples. I am grateful to Christoph Ollinger and Thorsten Gronemann for technical assistance during the sample preparation. I thank my former office partners Anja Glisovic and Sven-Philip Krüger, who have both read parts of this manuscript and given valuable comments, and my colleagues, Klaus Giewekemeyer and Sebastian Aeffner, who have done the same.

My heartfelt thanks also go to the members of the ILL Three-Axis (TAS) and Time-of-Flight (TOF) groups who have always made me feel part of a unique team. I am deeply indebted to Karin Schmalzl (TAS-group) and Tilo Seydel (TOF-group), who 'adopted' me in times when I sought scientific and other guidance. Both of them have also read parts of this manuscript. A special 'thank you' also to the members of the 'junior' TAS-group: Lola Ruiz-Martin, Elisa Wheeler, Alexander Grünwald and Paul Freeman. I enjoyed our discussions very much.

'Thank you' also to other former and present members of the ILL student-body: Martin Kempa, Liz, Katy, Clara, Mark, Johnny, Amy, Navid, Tinka, Jochen, Anton, Martin Dawson, Andreas, Audrey and Estelle. Thank you for the 'coffee breaks', the skiing and hiking, going to ice hockey matches, telling me to turn off skype once in while, restaurant visits and going out, 'international' cooking lessons, long game nights and generally for being there in trying and in fun times.

In Göttingen, I would like to thank my three 'oldest' friends who have accompanied me (almost) since the beginning of my undergraduate studies: Alice von der Heydt, Philip Zaulig and Mario Stanke. Countless offers of a couch to sleep on during my shorter stays, as well as help with my frequent moves are deeply appreciated at this point.

Of course, I am grateful to my mother, who has continuously supported me throughout my studies emotionally and financially. My special gratitude also belongs to my brother, Bernhard, whose constant presence in Bielefeld has been a great relief over the past two years.

Without all of you, this work could not have been possible. Thank you.

Lebenslauf

Name	Beate-Annette Brüning
Geburtsdatum	23. Dezember 1978
Geburtsort	Bielefeld
Staatsangehörigkeit	deutsch
Schulbildung	
1985 bis 1987	Bültmannshof-Grundschule in Bielefeld
1987 bis 1989	Riverside Elementary School in Princeton, NJ, USA
1989	Bültmannshof-Grundschule in Bielefeld
1989 bis 1995	Ratsgymnasium in Bielefeld
1995 bis 1996	Chetek High School in Chetek, WI, USA
1996 bis 1998	Ratsgymnasium in Bielefeld (Abitur)
Studium	
Oktober 1998 bis März 2005	Studium der Physik im Diplomstudiengang an der Georg-August-Universität Göttingen (Diplom)
seit September 2005	Promotionsstudium im Fach Physik an der Georg-August-Universität Göttingen Doktorandin am Institut Laue-Langevin in Grenoble, Frankreich
Berufstätigkeit	
August 2000 bis September 2002	studentische Hilfskraft in der Abteilung Molekulare Wechselwirkungen am Max-Planck Institut für Strömungsforschung, Göttingen
WS 02/03	studentische Hilfskraft in der mathematischen Fakultät der Universität Göttingen
SS 03	studentische Hilfskraft am Institut für Mikrobiologie und Genetik der Universität Göttingen
September 2005 bis August 2007	wissenschaftliche Mitarbeiterin am Institut Laue-Langevin in Grenoble, Frankreich
August 2005 bis September 2008	wissenschaftliche Mitarbeiterin am Institut für Röntgenphysik der Universität Göttingen